UNIVERSITY OF CALIFORNIA

SANTA CRUZ

Iontronic Devices with Biological Applications

A dissertation submitted in partial satisfaction

of the requirements for the degree of

DOCTOR OF PHILOSOPHY

in

ELECTRICAL AND COMPUTER ENGINEERING

by

John A. Selberg

September 2021

The Dissertation of John A. Selberg is approved:

Professor Marco Rolandi, chair

Professor David Haussler

Professor Mircea Teodorescu

Peter F. Biehl

Vice Provost and Dean of Graduate Studies

Table of Contents

Table of Figures

John Selberg

IONTRONIC DEVICES WITH BIOLOGICAL APPLICATIONS

Abstract

Bioelectronics is an exciting field that combines electrical and computer engineering, materials science, and biotechnology to develop new tools and therapeutics for the health challenges facing society. Iontronics is a subdiscipline within this field that is concerned with electronics that operate using ions as a charge or information carrier. Iontronics devices have a promising application as interfaces between electronic and biological systems as they can control ion concentration gradients and perform charged molecule delivery in the biological milieu. Protonics is an aspect of iontronics that deals with the movement of protons. Early works on bio-protonic devices displayed the application of these devices towards sensing and control of biological components such as enzymes and membrane-bound ion channels in the form of specialized proton pumps, and pH actuators. The next major step in the maturation of iontronic and protonic devices towards bioelectronics is the design, fabrication, and realization of these devices in *in vitro* and *in vivo* settings.

This work explores the development of bioprotonic devices for *in vitro* and *in vivo* applications. Along the way, protonic biosensors and actuators are discussed. For *in vivo* applications, I discuss a non-enzymatic glucose biosensor that is activated by pH-

shifting protonic electrodes and paves the way for metal-oxide biosensors implants. *In vitro* applications are explored in the context of protonic ion pump actuators. First, I present the development of proton pumps designed to break the buffer capacity of biological media using high-capacity palladium nanoparticle electrodes as a proton sink and source. Then, I iterate on this proton pump design to incorporate microfluidics for the long-term control of the membrane potential of stem cells that are cultured on-chip. Finally, I introduce adaptive machine-learning as a control method for closed-loop experiments with these bioelectronic devices. These results contribute to the field of bioelectronics by introducing new means for interacting biology in the form of biocompatible iontronic biosensors, protonic ion pumps for long-term cell experiments, and closed-loop control methods for long-term experimentation.

Acknowledgements

This work was enabled by the support of many people for whom I am truly grateful.

First, I want to thank my supervisor Marco Rolandi for all he has taught me over the years, for keeping a fire lit under me to reach my goals, and for drilling me on how to communicate my ideas clearly and effectively.

I am grateful for Mircea Teodorescu who is so welcoming, genuine, and has given me so much room to explore ideas in the Braingeneers Group. It has been a pleasure to be a part of the community of students that you maintain with such enthusiasm.

I am thankful for David Haussler and Sofie Salama of the Braingeneers Group for their patience, advice, and enthusiasm as I worked over the years to learn a new field.

I have gained so much by learning from other researchers over the course of my PhD but two stand out. Thank you, Xenofon Strakosas who taught me how to be an engineer and how to have fun doing it, and thank you Joel Sohn taught me how to keep my scientific compass pointing in the right direction.

I am very grateful for Tom Yuzvinsky who not only taught me about the equipment in our cleanroom and brainstormed ideas with me on countless occasions, but he gave me the freedom to try new things when others certainly would not.

Thanks to Pattawong Pansodtee an individual of many talents who has been there just about every step of the way.

Thanks to the past and present members of the Rolandi Group (not named previously) that have made this possible. Harika Dechiraju, Manping Jia, Chunxiao Wu, Raymond Breault, Zahra, Hemmatian, and Xiaolin Zhang. A special thanks to all the Rolandi Group interns that I got to work closely with during this time Maelia Uy-Gomez, Noah Christie, Alexander Flora, Nebyu Yonas, Brian Nguyen, and Carrie Bradley. Also, thanks to the visiting students Devis Montroni and Valeria Criscuolo.

Thanks to the Braingeneers Fluidics Group members Sergio Cordero, Gary Mantalas, and Spencer Seiler, and to all the other members of the Braingeneers group here at UCSC and at UCSF for which there are too many to mention.

Thanks to Mohammad Jafari, Marcella Gomez, and all the people that I have collaborated with on projects.

I want to thank my close friends Leahi Johsens, the Coté family, the Lake family, Todd Walker, Ian Scheiner, Kayla Sample, Alexander Bravo, Alex Rowe, Elektra Robinson, Kevin Johnson, Britney Martinez, Michael Doody, Raymond Berkeley, Christopher Anderson, Kiley Vogel, and Bianca Dootson, all of whom have kept me sane during this endeavor.

Finally, I would like to thank my parents Jan and John who have supported me so much over the years. Without them none of this would be possible.

Publications – In This Dissertation

BIOELECTORNICS AND IONTRONICS

Strakosas, X., **Selberg, J.**, Hemmatian, Z., Rolandi, M. (2017). "Taking Electrons out of Bioelectronics: From Bioprotonic Transistors to Ion Channels." Adv Sci (Weinh) **4**(7): 1600527.

Selberg, J., Gomez, M., Rolandi, M. (2018). "The Potential for Convergence between Synthetic Biology and Bioelectronics." Cell Syst **7**(3): 231-244.

Levin, M., **Selberg, J.,** Rolandi, M. (2019). "Endogenous Bioelectrics in Development, Cancer, and Regeneration: Drugs and Bioelectronic Devices as Electroceuticals for Regenerative Medicine." iScience **22**: 519-533.

Jafari, M., Marquez, G., **Selberg, J.**, Jia, M., Dechiraju, H., Pansodtee, P., Teodorescu, M., Rolandi, M., Gomez, M. (2021). "Feedback Control of Bioelectronic Devices Using Machine Learning." IEEE Control Systems Letters **5**(4): 1133-1138.

IONTRONIC BIOSENSING

Strakosas, X., **Selberg, J.**, Pansodtee, P., Yonas, N., Manapongpun, P., Teodorescu, M., Rolandi, M. (2019). "A non-enzymatic glucose sensor enabled by bioelectronic pH control." Sci Rep **9**(1): 10844.

IONTRONIC ACTUATORS

Strakosas, X., **Selberg, J.**, Zhang, X., Christie, N., Hsu, PH., Almutairi, A., Rolandi, M. (2019). "A Bioelectronic Platform Modulates pH in Biologically Relevant Conditions." Adv Sci (Weinh) **6**(7): 1800935.

Selberg, J., Jafari, M., Mathews, J., Jia, M., Pansodtee, P., Dechiraju, H., Wu, C., Cordero, S., Flora, A., Yonas, N,. Sophia, J., Diberardinis, M., Teodorescu, M., Leevin, M., Gomez, M., Rolandi, M. (2020). "Machine Learning-Driven Bioelectronics for Closed-Loop Control of Cells." Advanced Intelligent Systems **2**(12).

Jia, M., Dechiraju, H., **Selberg, J.**, Pansodtee, P., Mathews, J., Wu, C., Levin, M., Teodorescu, M., Rolandi, M. (2020). "Bioelectronic control of chloride ions and concentration with Ag/AgCl contacts." APL Materials **8**(9).

Selberg, J., Jafari, M., Bradley, C., Gomez, M., Rolandi, M. (2020). "Expanding biological control to bioelectronics with machine learning." APL Materials **8**(12).

Publications – Not Featured in This Dissertation

PROTON CONDUCTION IN BIOMATERIALS

Patel, H. A., **Selberg, J.**, Salah, D., Chen, H., Liao, Y., Krishna, S., Nalluri, M., Farha, O., Snurr, R., Rolandi, M., Stoddart, J. F. (2018). "Proton Conduction in Troger's Base-Linked Poly(crown ether)s." ACS Appl Mater Interfaces **10**(30): 25303-25310.

Selberg, J., Jia, M., Rolandi, M.. (2019). "Proton conductivity of glycosaminoglycans." PLoS One **14**(3): e0202713.

ORGANIC ELECTRONIC BIOSENSOR

Wu, C., **Selberg, J.**, Nguyen, B., Pansodtee, P., Jia, M., Dechiraju, H., Teodorescu, M., Rolandi, M. (2020). "A Microfluidic Ion Sensor Array." Small **16**(6): e1906436.

ION PUMPS

Dechiraju, H., **Selberg, J.**, Jia, M., Bradley, C., Pansodtee, P., Hernandez, C., Hsieh, H.C., Kim, J., Jafari, M. Gomez, M., Teodorescu, M., Rolandi, M. (2021). "Hydrogel Electrophoretic Ion Pump for Long-Term In Vitro Applications." *In Progress*.

Pansodtee, P., **Selberg, J.**, Jia, M., Jafari, M., Dechiraju, H., Thomsen, T., Gomez, M., Rolandi, M, Teodorescu, M. (2021). "The multi-channel potentiostat: Development and Evaluation of a Scalable Mini-Potentiostat Array for Investigating Electrochemical Reaction Mechanisms." arXiv: 2105.09810.

MICROFLUIDICS

Selberg, J., Cordero, S., Sieler, S., Mantalas., G., Pansodtee, P., Ly, V., Rolandi, M., Salama, S., Haussler, D., Teodorescu. (2021). "Microfluidic Culture System for Automated Experiments on 3D Human Tissues." *In Progress*.

Sieler, S., Mantalas, G., Cordero, S., **Selberg, J.**, Teodorescu, M., Salama, S., Haussler, D. (2021). "Optimized 3D Tissue Culture with Automated Regulation of Metabolites." *In Progress*.

Selberg, J., Cordero, S., Pandodtee, P., Sieler, S., Mantalas, G., Rolandi, M., Salama, S., Haussler, D., Teodorescu, M. (2021). “Rotary Pump for Parallelized Planar Microfluidics.” *In Progress.*

INTRODUCTION

1. BIOELECTRONICS

Beginning with Galvani's studies on animal electricity (*1*), bioelectronics has merged electronic devices with biology. One theme of bioelectronics is the use of electronic devices for the sensing and analysis of specific biological processes often relevant to health care (*2-6*). Another theme is the use of electronic signals for treatment and curing of medical conditions. Examples include the pacemaker, neuronal implants, and more recently, vagal nerve stimulation for the treatment of inflammation and organ malfunction (*7*). For these applications, typically electronics are adapted to interfacing with living systems with the additions of probes and sensor elements. Novel materials and strategies are necessary to tailor device properties to the length scales and characteristics of the biological environment. One important aspect of the biological environment is the prevalence of water and ionic conduction, two elements that do not typically merge well with semiconductor devices. Due to these challenges, new materials for bioelectronics are being explored, including carbon nanotubes and silicon nanowires in nanobioelectronic devices (*8, 9*), semiconducting polymers in organic bioelectronic devices (*5*), proton-conducting biomaterials and devices for bioprotonic (*10-12*), and ultra-thin semiconductors integrated in compliant plastic and dissolvable substrates for transient bioelectronic devices (*13*). A separate aspect of bioelectronics is the development of biological materials as electronic components (*14, 15*). Advantages of these biological materials include added functionality and precise

assembly at the nanoscale that reduces the need for complex fabrication strategies (*16*). An exciting class of these devices that incorporate these new materials and approaches to solve the challenge of interfacing electronics with biology is iontronics devices.

This section reproduced from (*17*).

1.2 BIOTIC-ABIOTIC MISMATCH

For a century, electronics have been designed to improve and expand our control over how information is stored in electrons. Traditional silicon-based electronics are composed of hard materials that operate in dry conditions. On the other hand, living systems often convey information in the form of ions, small ionizable molecules, and chemical modifications, and are composed of soft materials and exist in a wet environment. The mismatch between the electronic and biological information carriers, materials properties, and environment makes interacting between the two systems challenging (**Fig. 1.1**).

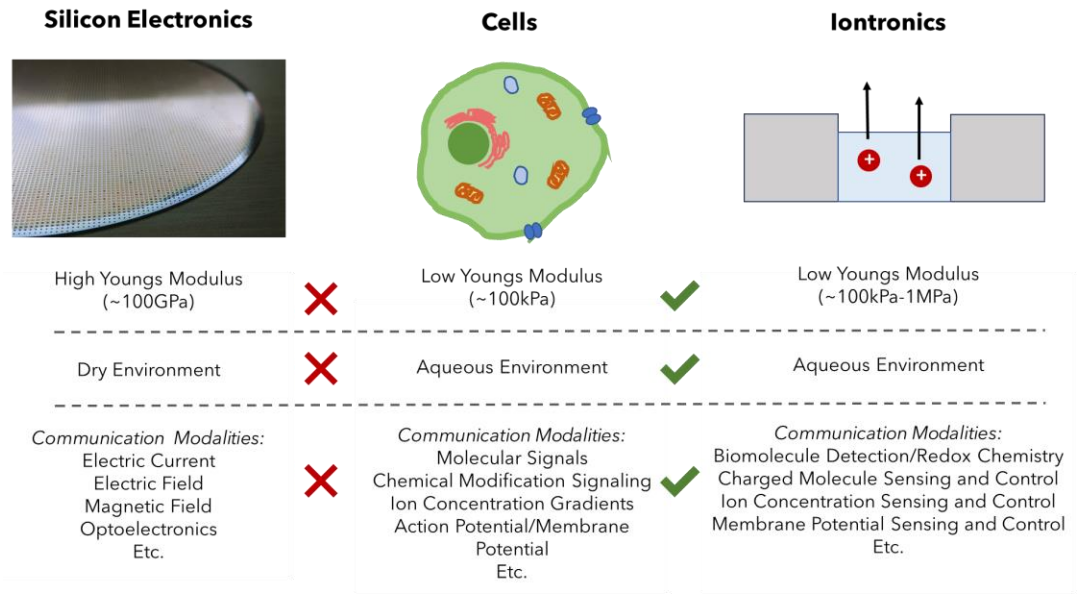

Figure 1.1. Comparison of traditional silicon electronics, cells, and iontronics.

1.3 IONTRONICS

Iontronics is a study of the motion and control of ions within an electronic device(*18*). Devices that are produced by this field rely on the role of ions as a charge carrier to operate. Iontronic devices address many of the challenges of incorporating electronics with biology by translating between electronic and ionic signaling and incorporating soft biocompatible materials. For this reason, ionic actuators and ionic sensors are being explored for their ability to interface between electronic and biological systems.

Iontronic devices take advantage of various electronic and materials properties advantages of working with ions including low operating voltage, low power

consumption, and high capacitance to operate (*19-22*). Researchers have developed many different iontronic devices and components including ionic diodes, ionic transistors, ionic LEDs, ionic memristors, and neuromorphic devices (Table 1.2.1). To make these, a wide variety of materials with ionically conductive properties have been explored for developing iontronics devices such as inorganic materials including metals, oxides, 2D materials and nanotubes as well as organic materials including ionic liquids, polyelectrolyte films and hydrogels, conducting polymers, and biopolymers (*18*). Iontronic technologies are very promising for many applications ranging from supercapacitors to low-power neuromorphic devices.

Device Type	**Examples**
Ionic Resistor	Ion Pump `Organic Electronic Ion Pump (OEIP)
Ionic Diodes	Polyelectrolyte Junctions (*23-25*)
Ionic LEDs	Light Emitting Electrochemical Cell, Protonic Light Emitting Diodes (*26*)
Ionic Transistors	Electronic Double Layer Field Effect Transistor (EDLT) (*27*) Ionic Bipolar Junction Transistor (IBJT)(*28, 29*) Organic Field-Effect Transistor (EGOFET)(*30, 31*) Organic Electrochemical Transistor (OECT) (*32, 33*) Protonic Transistor (*12, 34*)

Ionic Capacitors	Electric Double-Layer Capacitor (EDLC) (*35*) Organic Electronic Ionic Capacitor (*36*)
Neuromorphic Devices	Ionic Memristors (*37*) 3-Terminal Devices (*38, 39*)

Table 1.2.1 Iontronic Device Examples

1.4 BIOSENSORS

Biosensors are a highly studied application of bioelectronics and iontronics that are used to sense many properties of biological systems including electric fields and action potentials, cell growth, ion concentration, and biological markers. Iontronic devices employ various techniques to accomplish these goals (*20*). Electric field sensing is typically performed with high-capacitance electrodes that can detect minute changes in the number of ions forming an electric double layer capacitor at the electrode interface (*40*). Impedance based cell monitoring is carried out by monitoring a change in conductivity of an electrolyte or a change in the capacitance of an electrode that results from the growth (or death) of cells in a layer that block the movement of ions (*41*). Ion and metabolite sensors often rely on electrochemical or enzymatic reactions to detect the species of interest (*42*). In all of these devices the biosensor is transducing an ionic or biological signal into an electrical output that can recorded.

1.5 BIOELECTRONIC ACTUATORS

Bioelectronic actuators are devices that convert an electronic signal into a biological output. These devices are promising for biomedical applications because electronics are able to provide chronic, precise, and rapid stimulation of biological systems. The need for bioelectronic actuators is particularly evident for long term biomedical implants where alternative technologies like microfluidics are not feasible. The most iconic bioelectronic actuator is the artificial pacemaker developed in the 1950s(*43*). Generations of pacemakers have since been developed that rely on the same operating principle, a voltage applied across cells in the atria or ventricles stimulate an action potential which propagates and causes a contraction. Similar control of excitatory cells using neural implant actuators for deep brain stimulation is widely successful at epilepsy, pain management, and neural psychiatric disorders. The ability to control excitatory cells such as cardiomyocytes and neurons reshaped healthcare in the 20th century. In the 21st century, alternative methods of stimulation have gained interest to expand our control over biology beyond excitatory cells. Alternative bioelectronic stimulation methods utilizing electromagenetics, optoelectronics, plasmonics, ultrasonics, and iontronics are being explored to realize novel electronic-biotic interfacing.

Iontronic actuators that can directly control the flow of ions are compelling as life has evolved in a complex ionic environment and organisms have adapted to sense, control, and respond to the presence of ions and ion concentration gradients changes in many ways (*17*). Beyond atomic ions, ionic molecules and polymers are ubiquitous in

nature and necessary for all cellular processes ranging from cell-cell communication, chemical energy generation, biological information storage, and enzymatic reactions. By achieving control over the movement and distribution of ions and ionic molecules, iontronic actuators can communicate with cells in a vocabulary that they are adapted for. Iontronic control of ions and charged molecules will expand the ability to interface with non-excitatory cells and tissues for biomedical and research applications as well for engineering novel functionalities using synthetic biology (*17*).

1.6 CLOSED-LOOP BIOELECTRONICS

Nature achieves biological control using feedback wherein molecular sensors and actuators work in unison to maintain a steady state such as in homeostasis or achieve a desired target state such as in sensorimotor movements (*44*). The goal of closed-loop bioelectronic control refers to the achievement of an intended and predicted response in a biological system using bioelectronic devices. Broadly speaking, feedback is the feature of using information on system response to past inputs to inform immediate action (*45*). This type of control is referred to as closed-loop control. To this end, efforts toward integrating closed-loop control in biological systems have advanced primarily in synthetic biology (*46-49*). Closed-loop control in synthetic biology mimics natural systems such as genetic engineering (*50-52*), automated manipulation of the external environment through microfluidics (*52, 53*), and glucose regulation with an artificial pancreas (*54*). In contrast, relatively few examples of closed-loop control using bioelectronics currently exist (*55, 56*). Machine learning (ML) control strategies are

promising for their potential to account for many uncertainties that exist in working with complex biological systems and bioelectronic devices for applications of synthetic biology and medical devices (**Fig. 1.2**).

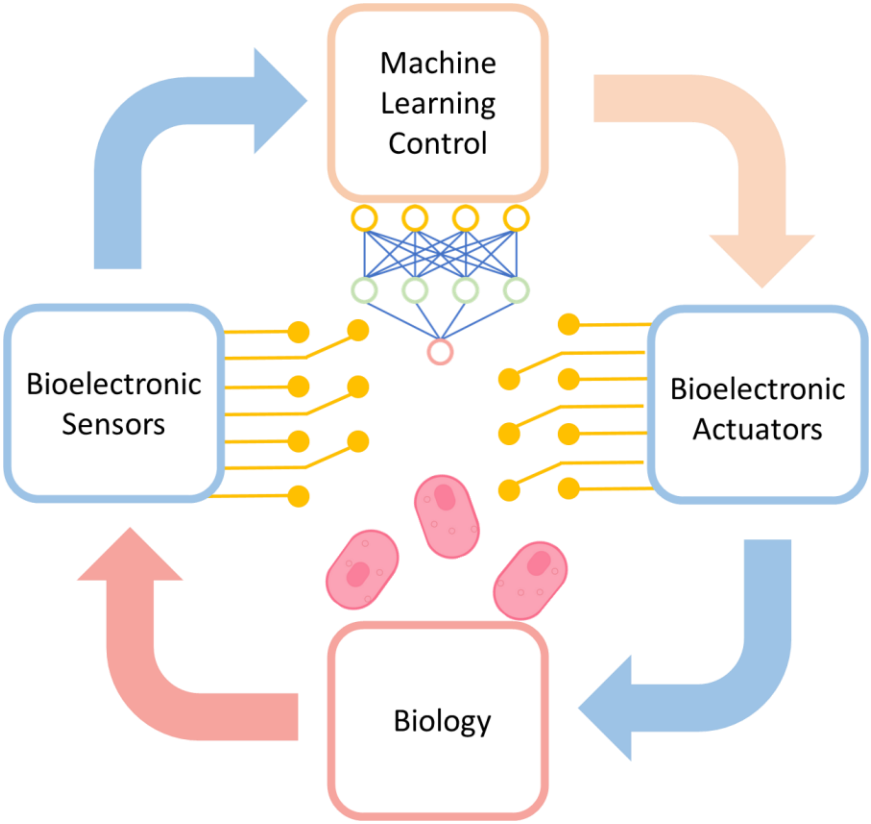

Figure 1.2. A Closed-loop Bioelectronic System with ML-Control of bioelectronic actuators using sensor feedback. *Reproduced with permission from (57).*

This section reproduced from (*57*).

2. ION TRANSPORT

2.1 ELECTROLYTES

Iontronic devices measure or manipulate the movement of ions. Often this transport happens within an aqueous environment in the form of electrolyte solutions, wetted polyelectrolyte solutions and membranes, and hydrogels. An electrolyte is a substance that when solvated disassociates its constituent ions. The extent of this ionization differentiates a strong (complete dissociation) or weak (partial dissociation) electrolyte. Electrolytes are extremely common in chemistry and biology in the form of salts, acids, and bases. Upon ionization the free energy of the solution is reduced. Typically, the dissociated ions interact with polar solvent molecules in their environment which organize around the ion forming solvation shells (**Fig. 2.1**). During dissociation, the total number of positive charges arising from cations and negative charges from anions in an electrolyte remains equal, keeping the charge neutrality. Importantly, these dissociated ions are mobile charge carriers and give an electrolyte the property of being electrically conductive. This characteristic is exploited in electrochemical and iontronic devices.

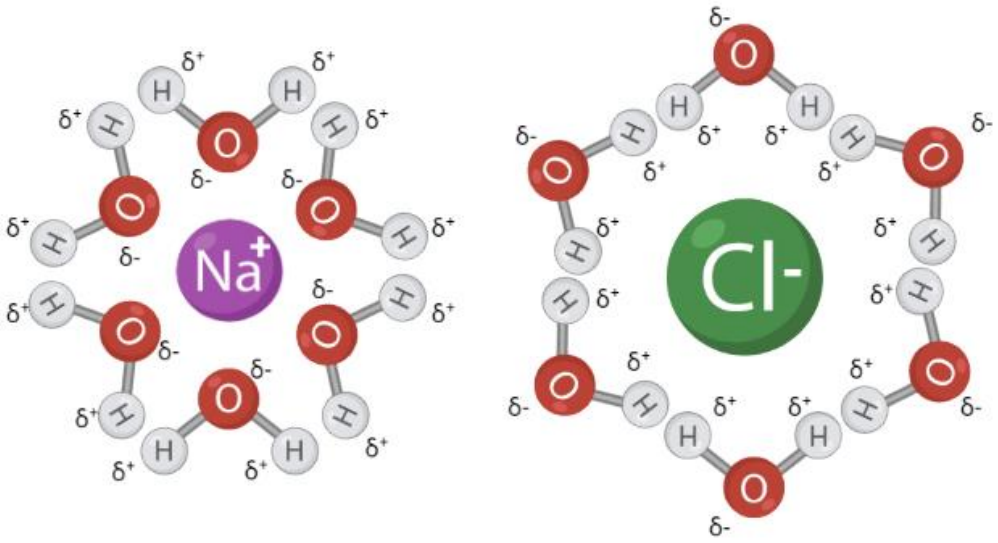

Figure 2.1 First solvation shell for Na+ and Cl- ions in water.

Much like an electronic in semiconductors and conductors, ions in an electrolyte are mobile and can convey electric current. This movement of ionic species is the combined effect of diffusion, drift, and convection. For many electronic applications it is important to understand the relation of diffusion and drift to ion transport as flow is not present.

2.2 DIFFUSION

Diffusion is the movement of particles (atoms, ions, molecules) down their chemical potential (u). The chemical potential is the energy for diffusion which generally decreases with the particle concentration (**Fig. 2.2**).

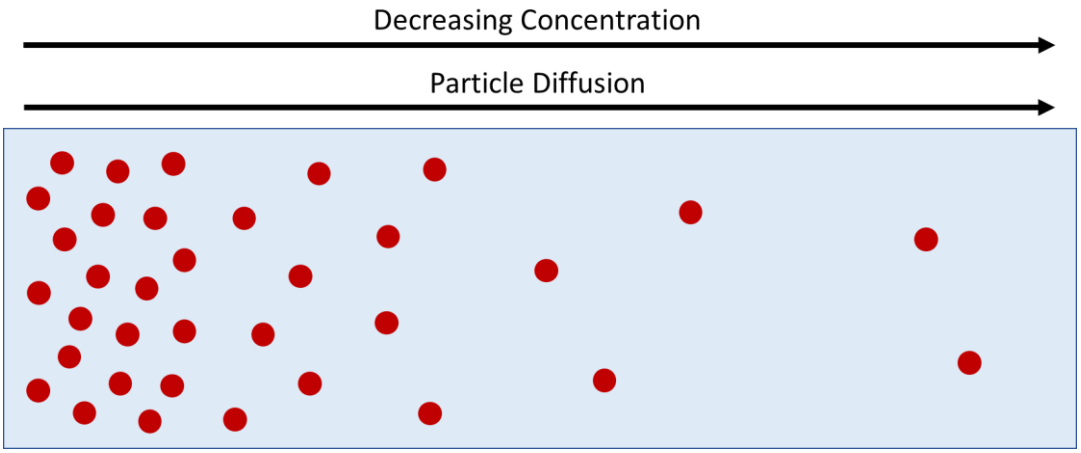

Figure 2.2. The diffusion of particles down their concentration gradient.

In conditions with a uniform ion concentration where the chemical potential remains the same over a given space, there will be no net diffusion of particles. In non-uniform conditions, when a particle moves down in concentration from c_i to c_f the chemical potential of the system decreases. This free energy change is associated with the force that drives diffusion:

$$\Delta u = u_F - u_i = RTln\left(\frac{c_f}{c_i}\right) \quad \textbf{(2.1)}$$

Fick's First Law describes the steady-state diffusive flux (J) arising from this force as proportional to the concentration gradient:

$$J = -D\frac{dc}{dx} \quad \textbf{(2.2)}$$

The diffusion coefficient (D) is a constant that relates the diffusive flux to the concentration gradient. Diffusion coefficients are determined experimentally and are

specific to the particle species and electrolyte environment. Typically, the diffusion coefficient scales inversely with a particle's radius as well as solution viscosity. For a spherical particle in a low Reynolds number solution, the diffusion coefficient is approximated by the Stokes-Einstein equation:

$$D = \frac{\mathrm{k}_b T}{6\pi\eta r} \tag{2.3}$$

Here, k_b is the Boltzmann constant, r is the particle's radius, and η the solution viscosity.

Fick's Second Law is an alternate form of the diffusion equation and describes how the concentration changes over time due to diffusion:

$$\frac{dc}{dt} = D\frac{d^2c}{dx^2} \tag{2.4}$$

Fick's laws are particularly useful for understanding how an electrolyte will behave when particles are delivered or removed through electronic or microfluidic means.

2.3 DRIFT

Ionic drift is the conduction of ionic species in an electric field. When an electric field is applied across an electrolyte, cations migrate to the negative terminal and anions migrate to the positive terminal (**Fig. 2.3**).

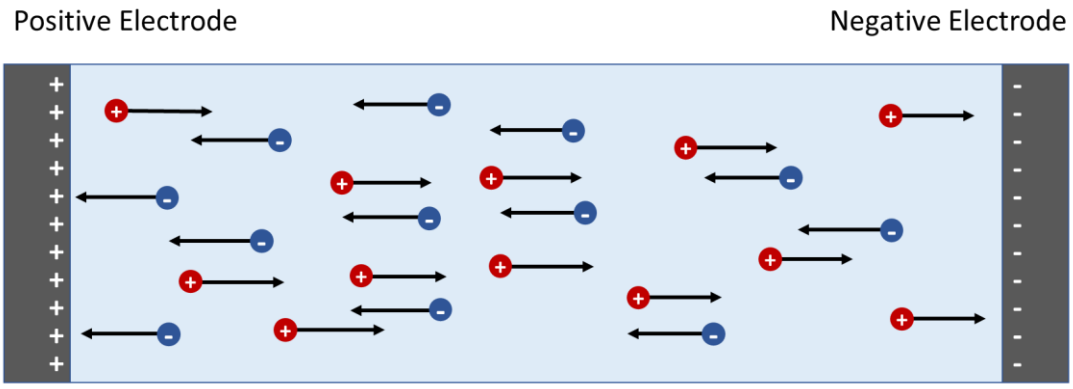

Figure 2.3. Ionic drift in an electrolyte. *In an electric field between two electrodes, cations will migrate towards the negative electrode and anions will migrate towards the positive electrode.*

The total current density is the combined effects of the current densities for the cation and the anion. Like the motion of the electron described by electron mobility, an ion's mobility (μ_i) relates the drift velocity of the migrating ions (v_i) to the magnitude of an applied electric field (E):

$$v_i = \mu_i E \qquad \textbf{(2.5)}$$

Eq. 2.6 connects the current density (j) from the migration of ions in this electric field with the drift velocity and the charge density. Here c is the ion concentration, z is the ion's valence, and F is Faraday's constant which is the charge in Coulombs one mole of electrons. Using Eq. 2.5, this relation can be rewritten in terms of the mobility and applied electric field:

$$j = zFcv_i = zFc_i\mu_i E \tag{2.6}$$

The transport flux associated with this current is the moles of ionic species migrating in the induced electric field:

$$J = \frac{j}{zF} = c_i\mu_i E \tag{2.7}$$

Using the Einstein relation:

$$D = \frac{\mu_i \mathrm{k}_b T}{ze} \tag{2.8}$$

which relates the diffusion coefficient for an ion to its mobility, the ion flux relating to migration in its more standard form is produced:

$$J = \frac{qDc_i}{\mathrm{k}_b T}\nabla\varphi = \frac{Dzc_i}{RT}F\nabla\varphi \tag{2.9}$$

Here R is the gas constant, and T is the temperature in Kelvin.

2.4 NERNST-PLANCK EQUATION

The electrochemical potential is the combined energy from the chemical potential and the electrostatic potential in an electrolyte. This electrochemical potential gradient is the driving force for ion transport which combines the effects of diffusion and drift. The ionic flux from drift and diffusion is explained by the Nernst-Planck equation:

$$J = -D\left(\nabla c_i - \frac{c_i}{RT} zF\nabla\varphi\right) \quad \textbf{(2.10)}$$

2.5 CONVECTIVE TRANSPORT

Convective transport is the movement of solution resulting from the bulk flow (**Fig. 2.4**). This flow can occur due to heat, density, or pressure gradients as well as the diffusion molecules in the liquid. Convection is the dominant mode of transport in microfluidic applications where molecules are delivered with an applied pressure. Mass flux from convective transport is primarily considered in the presence of liquid electrolytes as this process is reliant on bulk hydrodynamic flow. This requirement for liquid flow means that convective delivery of a species is accompanied by a significant volume of solvent molecules.

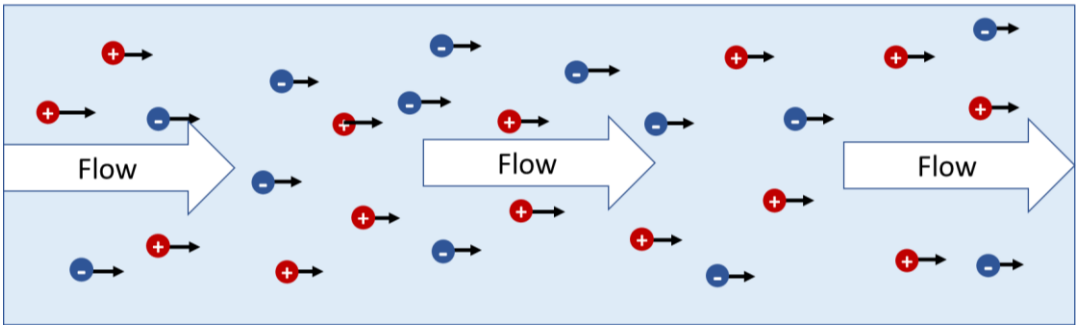

Figure 2.4. Convective Transport

A useful assumption is that the transport flux for a species undergoing convective transport is a product of the concentration of the given ionic species and the velocity (v) of the solution:

$$J = c_i v \tag{2.11}$$

An extended form of the Nernst-Planck equation incorporates flux from convective transport:

$$J = -D\left(\nabla c_i - \frac{c_i}{RT} zF\nabla\varphi\right) + c_i v \tag{2.12}$$

In most cases convective transport is a more potent mode of transport over diffusion and drift and will be the primary contributor to ion transport when present. Convection is also the most effective mode for transporting ions over long distances. For these reasons, there is extensive study of convective transport in the form of microfluidic devices for pharmaceutical, synthetic biology, and healthcare applications. However, downsides of convective transport that include a necessary volume change during delivery or removal of target species, a lack of species specificity, and co-delivery of

other species in the solution (including counterions) bar this transport mode from certain applications where these properties are limiting.

2.1.5 POLYELECTROLYTES

An important subset of electrolytes is composed of polymers which contain a covalently bound ionizable repeating unit, these polymer-based electrolytes are called polyelectrolytes (**Fig. 2.5**). When ionized in the presence of water, the polyelectrolyte can become anionic (polyanion), cationic (polycation), or ampholytic (polyampholyte) depending on the specific chemistry of the ionizable group (*58*). These charged groups on the polyelectrolyte are fixed on the polymer and are immobile relative to the dissociated counterion. The presence of fixed charges along the polymer backbone lends distinct electronic and mechanical properties to these materials.

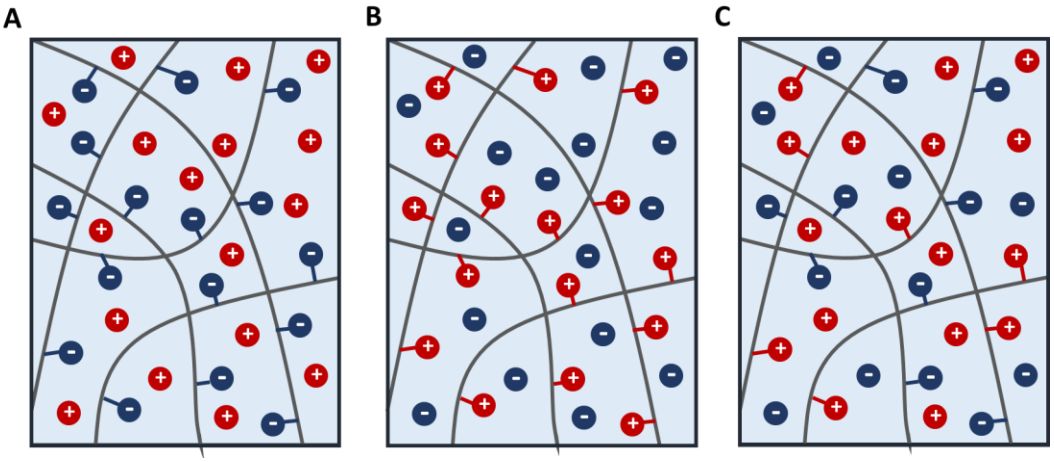

Figure 2.5. Types of polyelectrolyte. *(A) Polyanion. (B) Polycation. (C) Polyampholyte.*

Due to the high concentration of fixed charges, polyelectrolytes are very hydrophilic and are readily dissolved in polar solvents such as water. At high concentrations, polyelectrolytes can increase solution viscosity or induce gelation and form hydrogels. Many biological polyelectrolytes exist as hyperbranched polymers or be incorporated into large macromolecules, such as in glycoproteins which are components of many naturally occurring hydrogels. The hydrophilic nature and high swelling ability of these materials has lent them to a vast number of applications from thickening agents in cosmetics and foods to functional materials in water treatment and sensors (*59, 60*).

Membranes or films composed of polyelectrolytes can be formed through many means including spin coating, dip-coating, spray coating, drop casting, and directly crosslinking the polymer chains in solution (*61-64*). These membranes can absorb a

large amount of water, an application which has made them useful for developing humidity sensors (*65*). As these membranes increase in hydration, the polyelectrolyte ionizes, the counter ions are solvated and can move throughout the material. Ion transport in a polyelectrolyte different from the description for electrolytes. The charge that remains on the ionizable group of the polymer after ionization is fixed in position while the solvated counter ion is mobile. The fixed charges also electrostatically repel other ions of like charge, called coions, that may be present in the membrane. The implication of this is that for a polycation or polyanion membrane, the material selectively supports transport of counterions with a charge opposite of those fixed on the polymer. Polyanion and polycation membranes with these ion-selective permeabilities are generally referred to as ion exchange membranes (IEMs) (*66*). More specifically, the term anion exchange membrane (AEM) belongs to IEMs that are permeable to anions and contain fixed cationic groups, while cation exchange membrane (CEM) indicates a material is permeable to cations and contain fixed anionic groups. Beyond exclusion based on charge, the porosity of the polymer matrix in an IEM can be tuned to further select for ions based on size. For example, a dense IEM film may only be permeable to small monovalent ions while an IEM composed of a hyperbranched polyanion hydrogel may allow transport of larger molecules.

2.1.6 THE GIBBS-DONNAN EFFECT

A common occurrence when electrolytes are separated by a semi-permeable barrier that allows some of the ionic species in the electrolyte to pass, an uneven distribution

of ions occurs on either side of the barrier. Ions that cannot pass through the semi-permeable barrier electrostatically attract the permeable counterions against their concentration gradients (**Fig 2.6A**). During this process, electroneutrality in the solutions is maintained. The unequal distribution of ions from this movement is known as the Gibbs-Donnan Effect (Donnan Effect) (*67*).

The system is at an equilibrium when there is no net movement of ions, at this state the system is said to be in Donnan equilibrium. In this state, the electrochemical potential on one side of the semi-permeable barrier is equal the electrochemical potential on the other side. An electrical potential accompanies this equilibrium state that is related to the concentration of ions on either side of the barrier called the Donnan potential. The Donnan potential can be calculated with the equation (*68*):

$$\Delta\varphi_{donan} = \varphi_1 - \varphi_2 = \frac{RT}{F} ln \frac{c_1}{c_2} \quad \textbf{(2.13)}$$

Where φ_1 and c_1 are the potential and ion concentration on one side of the membrane and φ_2 and c_2 are on the opposing side.

The Donnan effect can occur across semi-permeable membranes that are selective on particle size, solubility, chemistry, and charge. IEMs are often utilized for charge selective permeability to separate cations and anions in an electrolyte. The IEM's counterion can exchange with the counterion species in the electrolyte while the coion

is electrostatically repelled in a process called Donnan Exclusion (**Fig 2.6B**). An application that highlights this process is the use of IEMs to soften water by collecting metal cations. In the case that two electrolytes are separated by an IEM, the membrane's counterions can transport between the two solutions (**Fig 2.6C**).

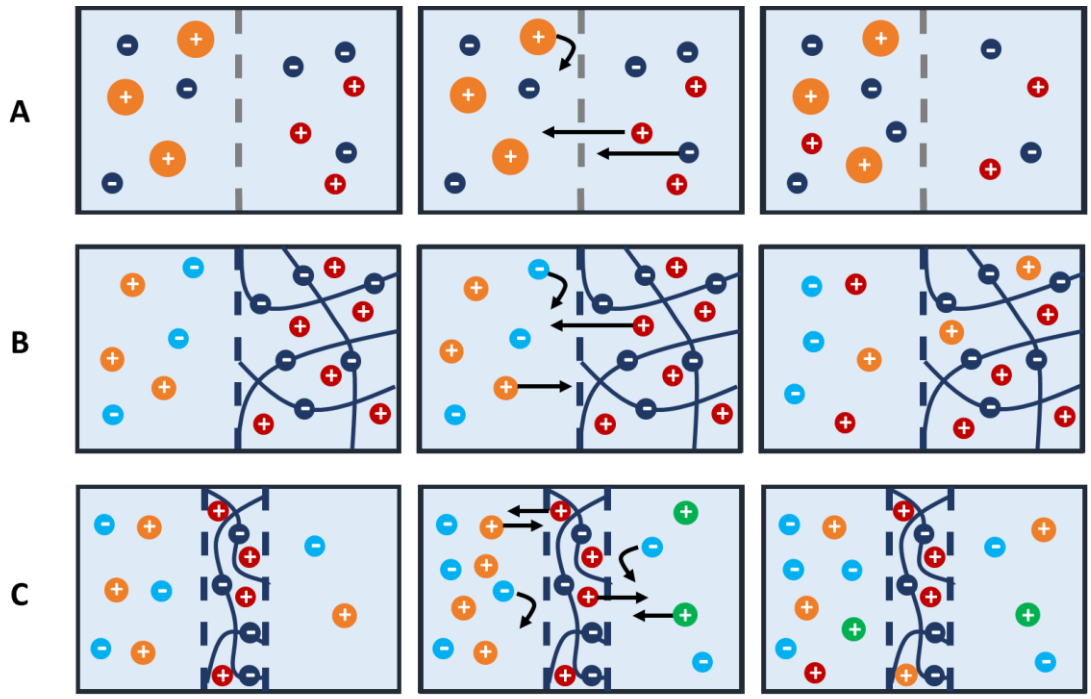

Figure 2.6. Donnan Effect. *(A) Donnan Equilibrium for a semi-permeable membrane that excludes particles above a set diameter. (B) Donnan exclusion in an AEM blocks anion diffusion while allowing cation exchange. (C) Cation transport between two electrolytes across an AEM.*

3. PROTONICS

The proton (H+), a hydrogen ion with a charge of +1e, is the smallest and simplest ion. Protons are ubiquitous and play an essential role in biology and involved in many natural phenomena (*69*), including oxidative phosphorylation (*70*), proton gated ion channels (*71, 72*), and pH regulation (*73, 74*). Iontronic devices that monitor and control H^+ currents can facilitate the interaction with these processes, these devices are known as protonic devices. Examples of protonic devices exist in the form of complementary bioprotonic transistors (*12*), diodes (*34*), protonic resistive memories, fuel cells, and batteries. Protonics are currently being explored as bioelectronic interfaces for sensing and actuating biology.

3.1 PROTONIC CONTACTS

Protonic contacts are made of Palladium (Pd) and Palladium hydride (PdH_x) and can transduce a current of H^+ and OH^- into an electronic current at electrode-electrolyte interface (*12, 75*). In common electrolytes, H^+ exist as hydronium ions (H_3O^+). When a Pd contact is immersed in solution and is biased at a negative voltage versus a reference electrode, H^+ (in the form of H_3O^+) adsorb onto its surface. Upon adsorption, a H^+ is reduced to H with an electron from the Pd. The H subsequently diffuses into the Pd contact and forms PdH_x; with *x* up to 0.6–0.7 (**Fig 3.1A**) (*76, 77*). The PdH_x alloy expands upon absorption of H and the associated mechanical stress may result in degradation of PdH_x /H^+ conducting material contact. The overall equation for this reaction is:

$$Pd + H^+ + e^- \rightarrow PdH_x \quad \textbf{(3.1)}$$

in which a H^+ transfers across the Pd/PdH_x solution interface. The electronic current at the Pd contact arising from the e^- transfer from the Pd to the H^+ is monitored with an external circuit as I_{H+} (*78*). When a PdH_x contact is positively biased, H will be released back to solution from the alloy as H^+ (**Fig. 3.1B**).

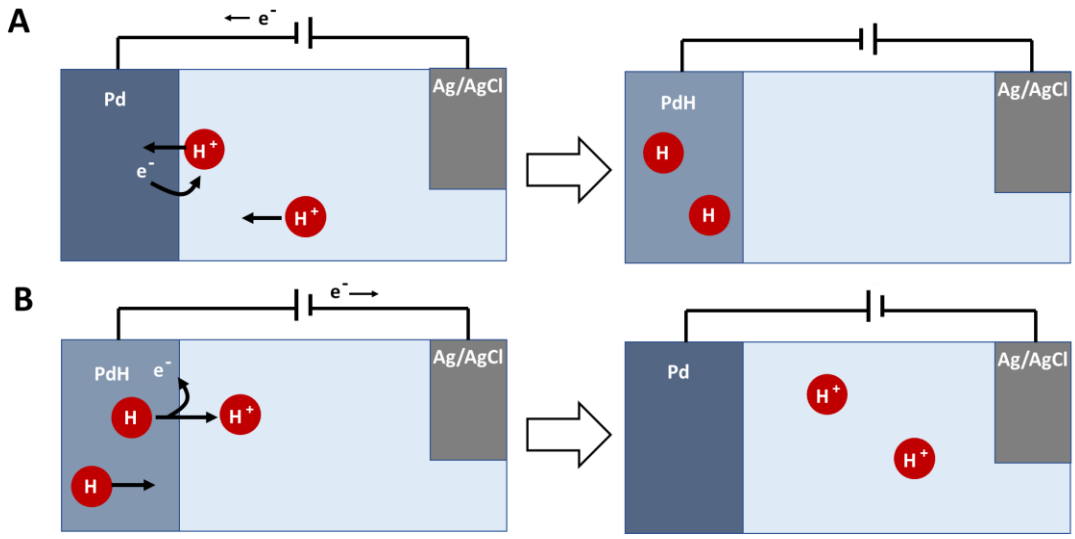

Figure 3.1. Pd/PdHx protonic contacts in aqueous solution. *(A) A negatively biased Pd electrode will absorb protons forming PdHx, in this process the solution is made basic. (B) A positively biased PdHx contact will release protons into solution, shifting the solution towards acidic.*

The threshold voltage applied to the Pd contact for the net transfer of H^+ across the Pd/PdH_x solution interface depends on the pH of the solution due to the influence of $[H^+]$ on the electrochemical potential (**Fig. 3.2**). As expected, in acidic solutions with high $[H^+]$ and electrochemical potential, a small negative voltage applied on the Pd

contact (V = –0.2 V) is adequate to transfer H^+ from the solution to the Pd contact and form PdH_x. In basic solutions with low [H^+] and electrochemical potential, a larger negative voltage (V = –0.9 V) applied on the Pd contact is required to transfer a H^+ from the solution to the Pd contact and form PdH_x (*79*).

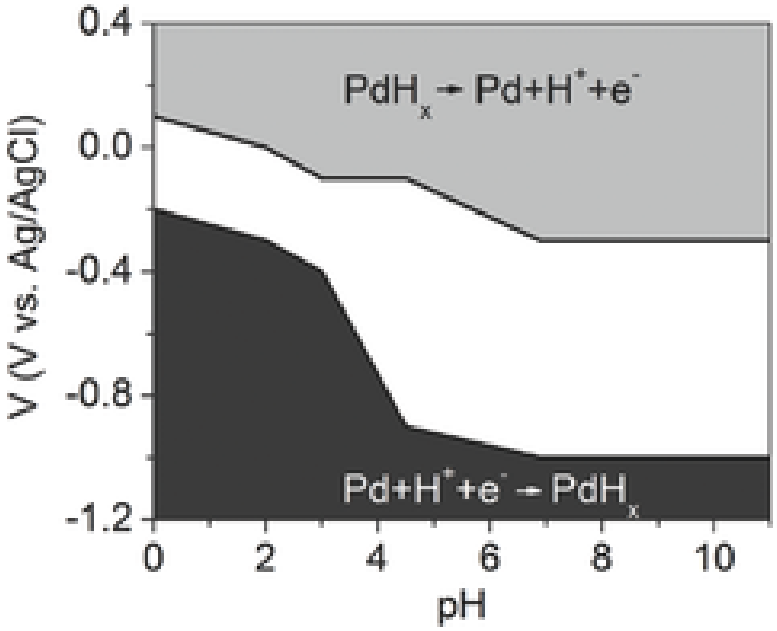

Figure 3.2. Voltage dependence of H^+ transfer across the Pd/PdH_x solution interface as a function of pH. *Reproduced with permission from (78).*

This section is reproduced with permission and modifications from (*80*).

3.2 PROTON TRANSPORT

A proton's mobility in water is about much greater than what is expected from typical hydrodynamic diffusion models. These models predict a hydronium ion (H_3O^+), the predominant form that a proton takes in aqueous solutions, that has a diameter of

~0.3nm to have a mobility on the order of K^+ with a diameter of 0.33nm. Instead, the mobility for a proton is about 4-6 times higher (*81*). The mechanism for this deviation was first explained by Theodor Grotthuss in 1806 in a process now known as the Grotthuss mechanism. The Grotthuss mechanism is a multistep process. In the first step, a hydronium ion aligned is aligned with a network of molecules via hydrogen bonding, then the electron density forming the covalent bond between a hydrogen on the hydronium ion is swapped with the hydrogen bond from adjacent water molecule. Effectively a proton is swapped between the two adjacent molecules. This change in electron density propagates along the water chain. At the terminal end of the water chain, a proton is produced and appears much more rapidly than the more massive hydronium ion would through mass transport. Finally, the water chain reorients the restore the original state of the water chain. A proton transported rapidly with this mechanism is typically described as 'hopping' or 'tunneling' along a water chain. A hydroxide OH^- ion can be transported in a similar manner via covalent/hydrogen bond swapping and the Grotthuss mechanism and has a higher-than-expected mobility in aqueous environments.

For rapid proton conduction over long distances via the Grotthuss mechanism, a highly organized network of water molecules needs to exist. In a bulk electrolyte, the conditions for this organization of water are not present and the Grotthuss mechanism only occurs over short distances when molecules transiently align via Brownian motion. Nonetheless, these short hopping events occur often enough to the increased

mobility H^+ and OH^- in water. As water molecules become more organized through freezing or other constraints on the individual molecules, long distance Grotthuss transfer can occur (*82*).

Many natural and artificial processes take advantage of the Grotthuss mechanism to improve performance. In these processes, water is organized into 'water wires' by constricting the volume that water molecules can occupy and localizing them to specific locations and conformations via hydrogen bonding (*83*). Biological proton channels make use of water wires to increase the efficiency of proton transport across a membrane. An example of this is Gramicidin, an antibiotic protein complex found in soil bacteria that inserts in the membrane of gram-positive bacteria and destroys the ion concentration gradients across the cell membrane – killing the cell. Gramicidin forms a barrel that spans the cell membrane with a pore that is filled with a single row of water molecules that are coordinated by acidic amino acid residues (*84*). Artificial proton channels are used to produce highly efficient proton exchange membranes for applications such as fuel cells, water electrolysis, ion exchange membranes, and batteries. Nafion is a benchmark proton exchange membrane that has a proton conductivity of 50-200 mS/cm (*85*). Nafion is composed of a highly-sulfonated fluorocopolymer simulations suggest that proton transport in hydrophilic regions of the material occurs largely through the Grotthuss mechanism and contribute in part to its high proton conductivity (*86*).

RESEARCH CONTRIBUTIONS

4. pH ACTIVATED IONTRONIC SENSING

This section will discuss work to develop a method for activating and deactivating redox-active metal-oxide surfaces though localized pH control. These metal oxides surfaces are of interest as they can oxidize many relevant biomolecules in solution, in the process an electronic current is collected that is proportional to the biomolecule concentration (*87, 88*). By greatly increasing the amount of hydroxide ions in the solution, the metal oxide surfaces become 'primed' for catalyzing the oxidation of biomolecules. This work discusses a cobalt oxide glucose sensor; however, it is translatable to other metal oxide/biomolecule systems.

Sections 4.1-4.4 are reproduced from (*89*) with permission.

4.1 GLUCOSE SENSING

Over 30.3 million people in the US have diabetes, a condition that now affects 18% of the worldwide population *(90, 91)*. Typically, a person with diabetes has to monitor their blood sugar level (2-20mM range) up to five times a day to regulate their metabolism. This monitoring involves the "prick test" to extract the blood, which could be painful, especially for children. Patients that avoid or forget to monitor themselves could suffer health repercussions. In severe cases, these repercussions can be fatal. Continuous glucose monitoring (CGM) that uses minimally invasive sources such as sweat is less demanding for patients. It improves healthcare by providing a higher data

collection rate with an increased reliability while avoiding the discomfort of the "prick test"(*92*). The glucose concentration in sweat ranges from 0.2mM to 0.6mM (*93*), thus glucose sensing in sweat requires higher sensitivity than in blood. Devices capable of CGM are particularly useful and many sensors exist that can detect glucose from sweat and tears (*94-98*). Google and Novartis have developed the smart Google contact lens, in which the sensing, storage, and transmission of the glucose levels occur on the contact lens (*99*). In a parallel path, glucose monitoring skin patches are able to measure glucose in sweat (*92*). All these examples are enzymatic sensors — the current standard for continuous monitoring of glucose (*100*). These sensors detect the presence of glucose by measuring the rate of glucose oxidation from the enzymes glucose oxidase or glucose dehydrogenase (*101*). For each glucose molecule oxidized, this reaction transfers an electron through a mediator to the sensing electrode. The sensing electrode records this electron transfer either by reading the electrode current or electrode potential. Enzymatic glucose sensors are highly sensitive, but the lifetime of these sensors is limited by decreasing enzymatic activity with time, this lifespan is typically one to two weeks. This relatively short lifetime increases cost and reduces scope (*100, 102*).

Non-enzymatic glucose sensors based on metal oxides at the interface with nanostructured porous metals or carbon materials have longer lifetime because they do not contain a biological component (*103, 104*). Metal oxide sensors detect glucose via the direct oxidation reaction of glucose with an activated metal oxide contact; the

reaction results in an electron transfer to the contact which is recorded by the sensor as a current (*105*). A highly sensitive and stable substrate for glucose detection is cobalt oxide at the interface with nanoporous gold (*106*). However, this sensor only works in high pH (pH ≥ 11) because it requires the presence of hydroxide ions (*107*). This restriction of working only at high pH is not limited to cobalt oxide sensors but applies to many metal oxide and inorganic material-based sensors that oxidize target molecules (*108*). Thus, the development of metal oxide sensors for CGM applications has struggled since bodily fluids such as sweat and tears have a pH range of 4-7 (*109*). Here, we have developed a cobalt oxide-based glucose sensing platform that is able to detect glucose in solutions with the same pH as the bodily fluids such as sweat and tears. The proposed sensor includes the bioelectronic control of pH in the proximity of the cobalt-oxide sensor surface enabling sensing glucose at high pH even in an otherwise neutral fluid.

4.2 RESULTS

The glucose sensor comprises cobalt oxide (Co_3O_4), palladium (Pd), and silver/silver chloride (Ag/AgCl) contacts electrochemically grown on gold (Au) strips defined on a glass substrate. The Co_3O_4 contact is used to sense glucose, the Pd contact is used to change the local pH of the fluid, and the Ag/AgCl contacts act as reference electrodes that balance the half reactions for glucose and pH modulation respectively (**Fig. 4.1A** and **Fig. 4.1B**). These contacts are connected to an external circuit board that provides

control voltages (V_g for the Co_3O_4 and V_{pH} for Pd), measures the contact currents (I_g for Co_3O_4 and I_{pH} for Pd), and provides signal analysis and wireless communication to a personal computer (**Fig. 4.1A**). The geometry of the platform consists of long and narrow interdigitated contacts with a gap of 20μm. The specific geometry was designed with the aim to increase the I_g and I_{pH} currents by increasing the surface area and minimize the time for pH diffusion towards the Co_3O_4 by reducing the spacing between Pd and Co_3O_4 contacts. The novelty of this glucose sensing platform is the ability to create localized and transient alkaline conditions (high pH) for glucose sensing to occur on the cobalt oxide contact even in neutral fluids (**Fig. 4.1C**). This transient high pH is needed because in neutral pH solution, at low voltage (e.g., V_g = 0.2-0.5V), the glucose oxidation reaction does not occur on the Co_3O_4 contact and thus the presence of glucose cannot be detected. To induce local alkaline conditions of a solution starting at pH 7, we set V_{pH}= -1V between the Pd and the Ag/AgCl. Pd has the ability to absorb H^+ from the solution by first reducing H^+ into H at the Pd/solution interface and then absorbing H into its metal lattice to form PdH_x with x being the atomic ratio of H to Pd and its value can reach up to 0.6 (*80*). In this fashion, our group has already demonstrated transfer of H^+ to and from hydrated proton conducting polymers (*10, 12*) as well as membrane proteins (*110, 111*), modulation of solution pH for monitoring enzymatic reactions (*112*), controlling bioluminescence (*113*), and targeted cargo delivery to cells (*114*). By setting the value of V_{pH}, we control the pH of the fluid by multiple units in proximity to the cobalt oxide contact, thus creating a local environment for glucose sensing to occur. when the measurements are done, the pH is restored to its original

value, by switching the V_{pH} off which causes PdH_x to release its stored H back into solution as H^+ (**Fig. 4.1C**).

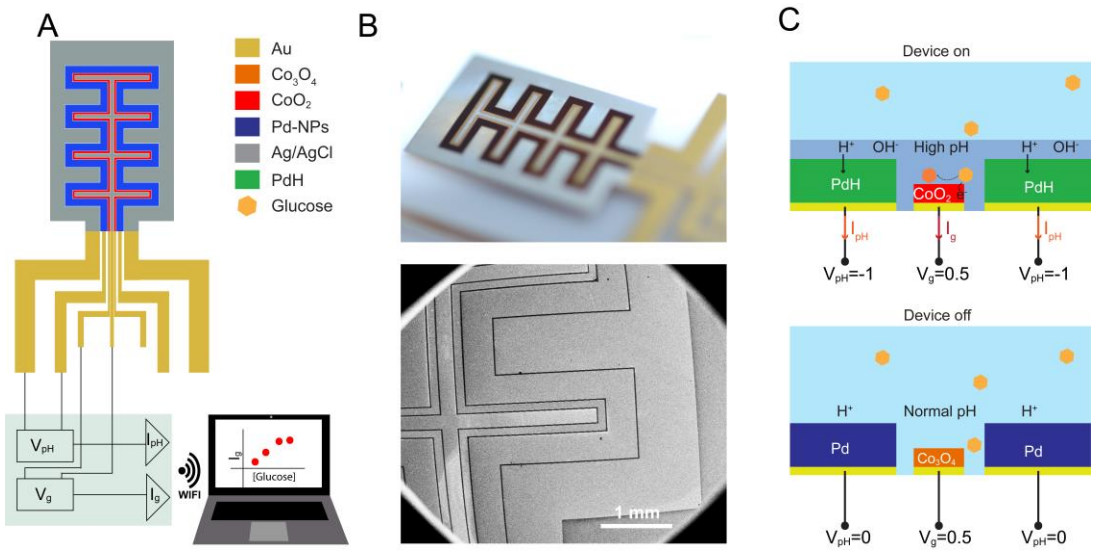

Figure 4.1. Non-enzymatic glucose sensor. A*, Schematic of the non-enzymatic glucose biosensor. A Pd contact (blue) locally creates basic conditions. In basic conditions, a nanoporous Au/Co_3O_4 (red) contact catalyzes glucose to gluconic acid. Two Ag/AgCl electrodes (grey) act as reference electrodes to the Pd and Au/Co_3O_4. A small conditioning board controls the device, acquires current, and transmits wirelessly to an external device.* ***B****, Optical image (top) of the modified contacts glucose biosensor. Au contacts were modified with Pd, Co_3O_4, and Ag/AgCl by using electrodeposition. SEM image (bottom) of the platform showing the interdigitated contacts with a 20 μm gap between each contact.* ***C****, operating principle for glucose sensing. When the device is on (top), V_{pH} = -1 V, the Pd contact absorbs H^+ from the solution and increases its*

pH. At high pH, the Au/Co_3O_4 contact is in its more reactive CoO_2 oxidized state. With V_g = 0.5 V, the CoO_2 contact oxidizes glucose, and the resulting I_g is collected, which increases with increased glucose concentration. When the device is off (bottom), V_{pH} = 0 V, the pH is at physiological values, typically pH 7, no sensing occurs from the Au/Co_3O_4 and I_g = 0 A.

The Au contacts are etched electrochemically by alloying/dealloying in the presence of zinc chloride following the protocol previously reported by Lang *et al. (106),* to increase the surface area **Fig 4.2** and **Fig 4.3**) and improve the sensitivity towards glucose sensing.

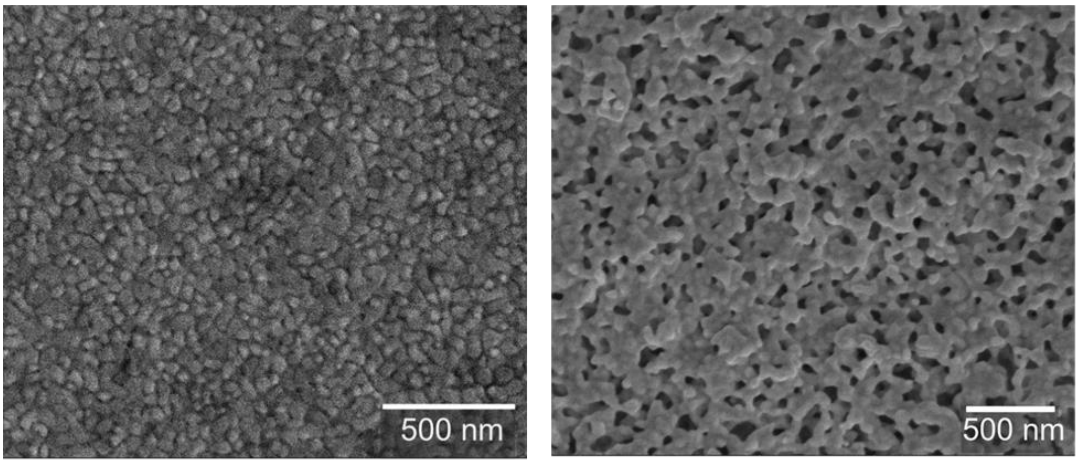

Figure 4.2. Au Etch SEM. *Un-etched Au (left). Nanoporous Au etch with $ZnCl_2$ in Benzyl Alcohol at 120C (right).*

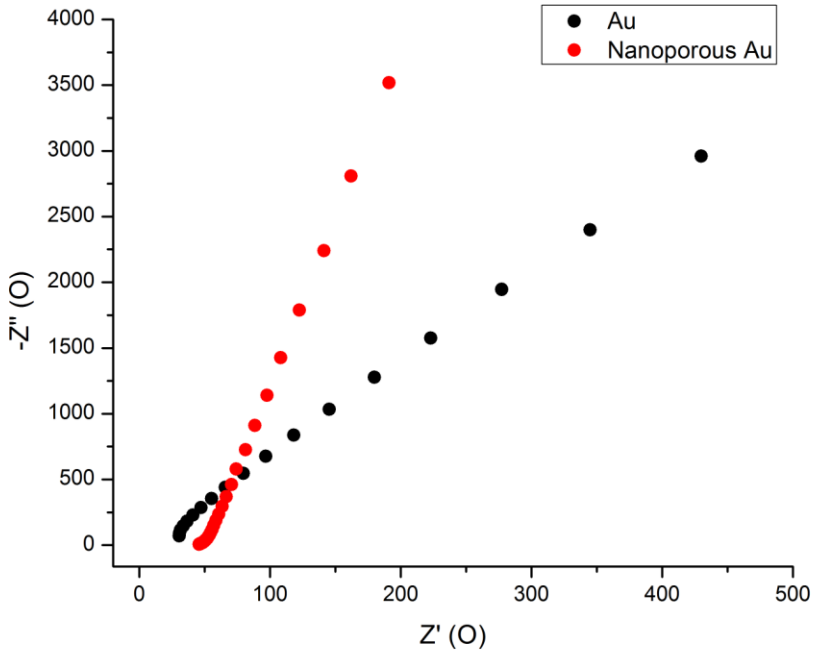

Figure 4.3. Bare Au vs nanoporous Au Nyquist plot generated *from impedance spectroscopy measurements.* *The nanoporous Au has a higher capacitance evident by the larger value of the imaginary impedance.*

Cobalt oxide is then deposited on the gold surface as Co_3O_4 and, in solution, undergoes a series of oxidation reactions with hydroxide (**Fig. 4.4A**). These reactions increase the oxidation state from Co(II/III) to Co(III) and Co(IV), respectively(*107*):

$$Co_3O_4 + OH^- + H_2O \rightarrow 3CoOOH + e^- \quad (4.1)$$

and

$$CoOOH + OH^- \rightarrow CoO_2 + H_2O + e^- \quad (4.2)$$

While both Co_3O_4 and CoOOH species can oxidize glucose, the primary mechanism for oxidation of glucose to gluconolactone in cobalt oxide sensors involves two Co(IV) atoms in the reaction (*107, 115*):

$$2CoO_2 + C_6H_{12}O_6 \rightarrow 2CoOOH + C_6H_{10}O_6 \quad (4.3)$$

In (3), two Co(IV) atoms are reduced to Co(III) as CoOOH. These CoOOH species are in turn oxidized back to CoO_2, for each Co(III) oxidized to Co(IV), two electrons are collected by the cobalt oxide contact and are recorded as current (I_g) (2). At neutral pH, the concentration of hydroxide species necessary to create Co(IV) is low thus greatly limiting the glucose oxidation reaction kinetics. At high pH (**Fig. 4.4A**), the cobalt surface contains many more Co(IV) and the glucose oxidation reaction is faster allowing glucose detection at lower concentrations respect to neutral pH. For this reason, metal oxide sensors and other inorganic sensors that directly oxidize glucose operate at high pH (*108*).

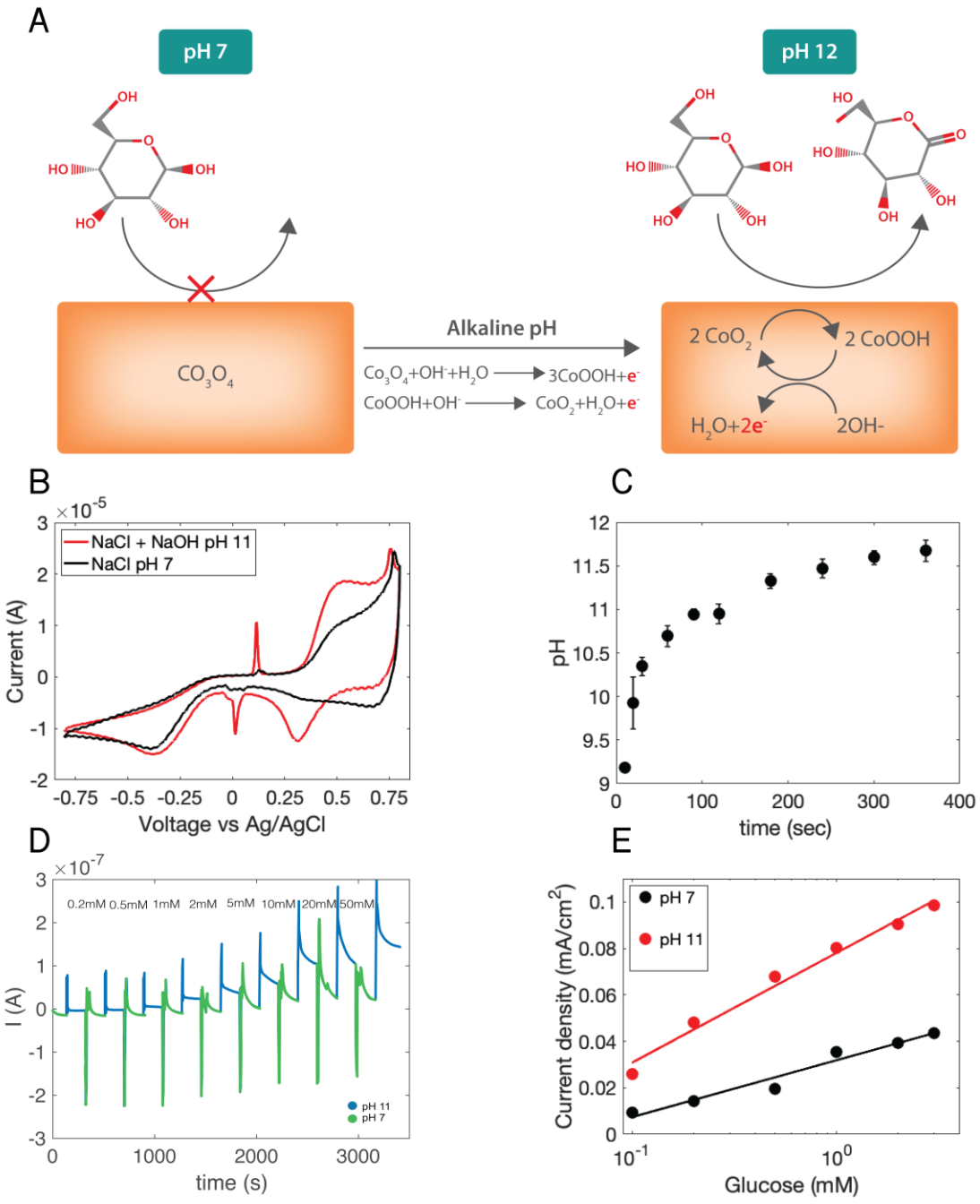

Figure 4.4 . Glucose Sensor Operation. ***A***, *sensing mechanism of Co_3O_4 contacts. At pH 7, the contact is primarily Co_3O_4, which does not oxidize glucose. In alkaline conditions (pH ≥11), the contact is now mainly CoO_2. CoO_2 species react with glucose*

*and are converted to CoOOH. This CoOOH is then oxidized back to CoO_2. For every oxidized glucose molecule, the contact collects two electrons measured as I_g. **B**, cyclic voltammetry of a nanoporous Au/Co_3O_4 contact in 0.1M NaCl at pH 7 and 0.1M NaCl + 0.001M NaOH at pH 11 containing 10mM of glucose. **C**, pH of 0.1M NaCl (initial pH = 7) after pH modulation by a Pd electrode with a V_{pH} = -1V between 10s and 5 minutes. **D**, Device operation. Current response of device at a constant voltage V_g = 0.5V over increasing concentrations of glucose in 0.1M NaCl solution. Pd contacts cycle the pH between pH 7 ($V_{pH} \geq 0V$) and pH 11 (V_{pH} = -1V). During the pH 7 phase, glucose concentration is stepped. **E.** Calibration curve of sensing platform versus glucose concentration with a fit for pH 11 and pH 7 induced by Pd for 100sec.*

To see the behavior of the sensing element in our platform, we performed cyclic voltammetry measurements (CV) using a Co_3O_4 contact in NaCl solutions containing 10mM glucose at pH 7 (**Fig. 4.4B**, black trace) and NaCl with 0.001M NaOH at pH 11 (**Fig. 4.4B**, red trace). From the CV it is clear that the glucose oxidation reaction at pH 7 is barely detectable, while at pH 11 in 0.001M NaOH the peak current associated with oxidation Co(III) to Co(IV) after the contact is reduced by the reaction with glucose occurs around V = 0.5V (**Fig. 4.5**). Similarly, we performed CV of glucose in pH 12 and pH 13. When the pH increases, both oxidation peak current magnitude increases as well as its peak position shifts to lower potential (**Fig. 4.6**).

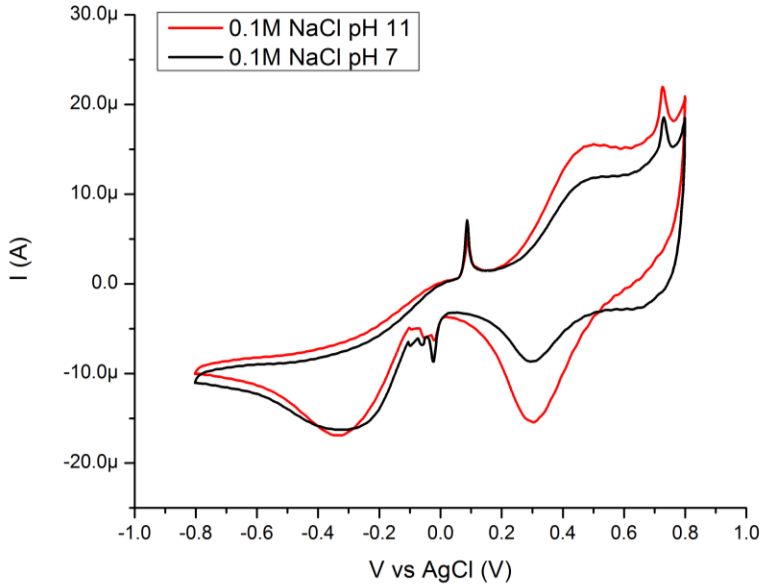

Figure 4.5. Cyclic voltammetry of nanoporous Au/Co3O4 in 0.1M NaCl pH 7 and 0.1M NaCl with 0.001M NaOH (pH 11).

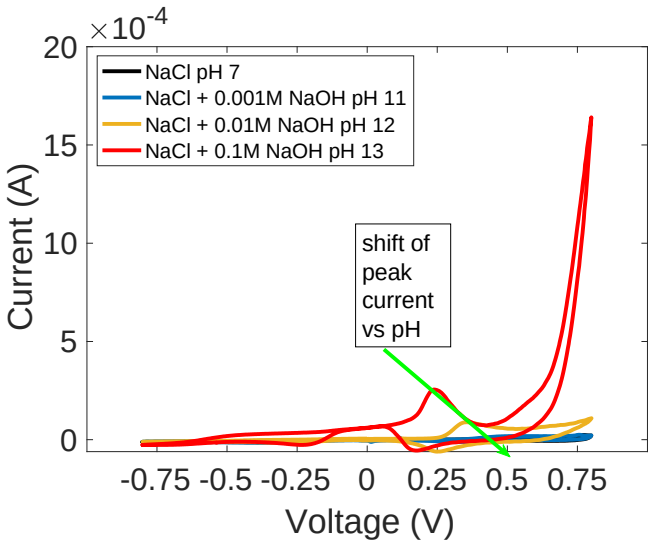

Figure 4.6. Cyclic voltammetry of nanoporous Au/Co_3O_4 in 0.1M NaCl pH 7 and 0.1M NaCl with 0.001M NaOH (pH 11), 0.01M NaOH (pH 12), and 0.1M NaCl with 0.1M NaOH (pH 13) in the presence of 10mM glucose.

To reproduce the alkaline conditions found when the glucose sensor is immersed in NaOH, we perform pH control in proximity to the cobalt oxide contact using the Pd contact with V_{pH} = -1V for different amounts of time (t) in NaCl at pH 7 (**Fig. 4.4C**). For t < 300s the pH increases with time because H^+ can transfer from the solution to the Pd contact. However, at t= 300 s the solution pH saturates because there is a low concentration of H^+ while an OH^- constant concentration is reached at the interface with the Pd. Even with lower V_{pH} = -3V, the solution pH saturates at pH 11-12 (**Fig. 4.7**). This transient pH change is reversible when the V_{pH} is returned to 0 V (**Fig. 4.8**). We are limited in the magnitude of V_{pH} by electrolysis of water. We thus choose a V_{pH} ~ -1V for our glucose sensing. This V_{pH} value corresponds to a solution of pH 11.

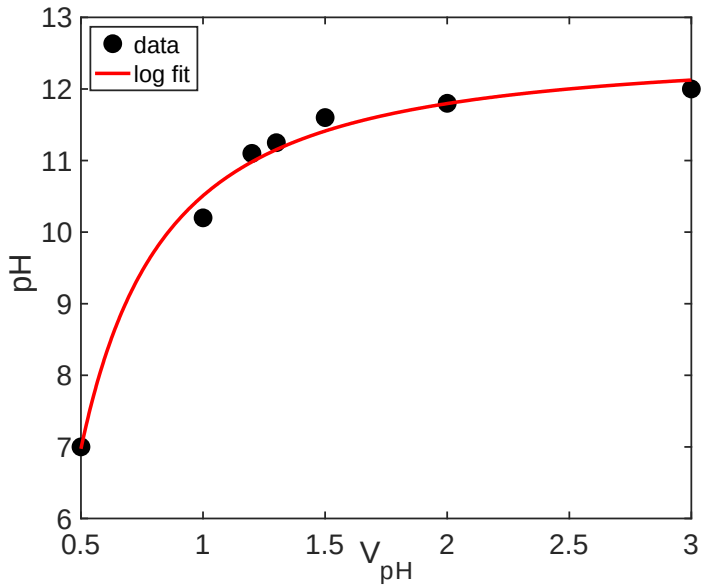

Figure 4.7. pH changes versus applied V_{pH} in 0.1ml volume of 0.1M NaCl solution after 120s.

For glucose detection, we measure the current at the cobalt oxide sensing contact (I_g) with V_g = 0.5V (**Fig. 4.4D**). However, the increased current from glucose oxidation can begin to occur in lower voltage V~0.2V (**Fig. 4.6**). A low V_g~0.2V can be useful to improve the selectivity towards interferent species such as lactic acid and uric acid that exist in sweat. During the measurement we cycle the solution pH from neutral (V_{pH} = 0.3V) to pH 11 (V_{pH} = -1V). At neutral pH, I_g is very small for glucose concentrations below 1mM. However, at pH 11, I_g raises above the noise level and further increases with addition of glucose in concentrations from 0.2mM to 50mM during periods of pH 11 (V_{pH} = - 1V). The resulting I_g is plotted against glucose concentration for 0.1-3mM both at pH 7 and pH 11 (**Fig. 4.4E**). These data clearly show that the glucose oxidation is more efficient at pH 11 and is required for better sensitivity of our biosensor.

Additionally, a Langmuir isotherm fit corresponding to the adsorption of glucose at the surface of the Co_3O_4 agrees with the experimental data at the concentration range between 100μM-3mM. allowing for detection of glucose in sweat concentrations while electronically inducing basic conditions in electrolytes of physiological pH. Co_3O_4 sensors have shown limit of detection in the nanomolar range in high alkaline conditions(*107*), however, in this work we did not perform measurements for finding the detection limit. At pH 11, the reaction rate, is higher because there are more Co (IV) species available to oxidize the glucose. It is worth mentioning that when V_{pH} goes from V_{pH} = -1V to $V_{pH} \geq 0$ the pH in the vicinity of the Co_3O_4 is higher than pH 7 due to slow H^+ diffusion. This may result in the increased signal in the black curve of **Fig. 4.4E** (pH 7).

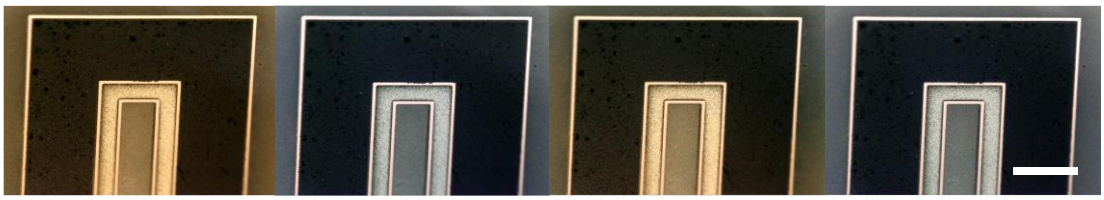

Figure 4.8. pH changes detected optically in NaCl with pH indicator solution. *The palladium contact (black) cycled between -1V and +0.3V vs an AgCl pellet electrode for 1 minute at each voltage. The solution switched between an initial neutral solution (yellow) at t=0s (left), to basic pH (blue) at t=60s after 1 minute of -1V on the Pd (second from left). The cycle was repeated neutral conditions at t=120s after +0.3V on the Pd, and basic conditions at t=180s. Scale = 0.4mm.*

To demonstrate the feasibility of the non-enzymatic cobalt oxide glucose sensor in real world continuous glucose monitoring measurements, we developed a prototype low-cost and low-power miniature board that can apply voltages (V_g, V_{pH}), record and condition the signal as well as transmit it to an external device (WI-FI) for storage and post processing (**Fig. 4.9A**). The board includes a WI-FI enabled microcontroller, a multiplexer, an amplifier, and analogue to digital converter, and two batteries. We connect the board to the cobalt oxide, palladium, and silver/silver chloride contacts to the input and outputs of the board (**Fig. 4.9B**). A high-level schematic is presented in **Fig. 4.9**. The board features two electronic circuits, which are isolated from each other and each of them has an adjustable power circuit. The first circuit supplies V_g (from 10mV to 3.2V) to the Co_3O_4 contact for glucose sensing to occur, and the second circuit supplies V_{pH} (from -1.1V to 0.3V) to the Pd to create the alkaline conditions. We used a WI-FI enabled microcontroller (ESP8266,) and a 16-bit analog-to-digital converter to measure I_g. **Fig. 4.9D** shows the experimental I_g current acquired from the glucose sensing platform and the circuit board by increasing concentrations of glucose in a NaCl solution made to reproduce human sweat. This I_g data is filtered by the conditioning board to remove noise and recorded with a customized software in a personal laptop wirelessly connected to the microcontroller. **Fig. 4.9D** shows the measured current as a function of time in seconds (gray) as well as the filtered signal using a moving average filtering technique with a 1/3 of a second window (black). The data is consistent with what we acquired with the bulkier and non-portable potentiostat

and semiconductor parameter analyzer and follows the analogous calibration curve presented in **Fig. 4.4E**.

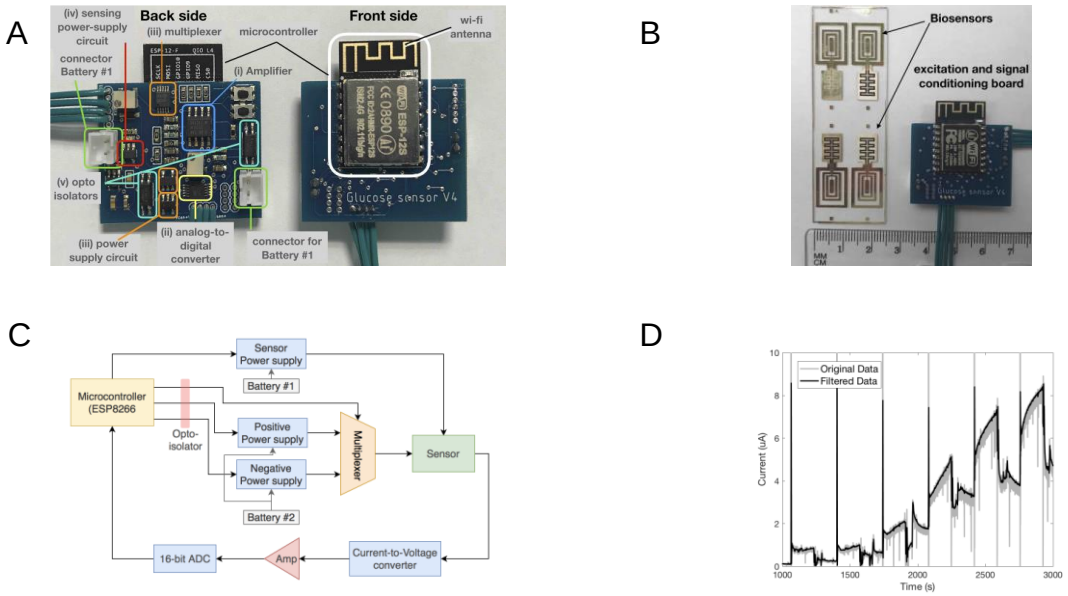

Figure 4.9. Integrated biosensor and sensing/excitation board. ***A****. Photo of the excitation and signal conditioning board used to provide* V_{pH} *and* V_g *and measure the current generated by the chemical reaction to determine the glucose level (*I_g*).* ***B****. the biosensor (left) and the microcontroller signal conditioning/sensing board (right) that applies* V_{pH} *and* V_g*, extracts and amplifies the sensing current, and transmits the results via WI-FI for further analysis. Please note that one microscope slide fits 4 experimental biosensors.* ***C****. The circuit schematic explaining how the components shown in* ***Fig.*** *3a are integrated with the biosensor.* ***D****.* I_g *vs time recording with microcontroller from sensing at 0mM, 0.1mM, 0.2mM, 0.5mM, 1mM, 2mM, 3mM glucose concentration in 0.1M NaCl solution.*

4.3 DISCUSSION

We have developed a non-enzymatic metal oxide glucose sensor that is able to detect physiologically relevant glucose levels in neutral bodily fluids such as sweat and tears. This sensor is superior to other metal oxide glucose sensors because it does not require an alkaline fluid for operation. To sense glucose in neutral fluids, this sensor induces a localized and reversible pH change with a Pd contact that absorbs H^+ from the neutral fluid and increases the pH. This flexibility allows for the seamless integration with current glucose sensing platforms such as contact lenses (*99*), and skin patches (*92*). Respect to the current enzymatic sensors, this metal oxide sensor does not suffer from limited lifetime due to enzyme degradation over time. This strategy of controlling local pH to enable sensing in neutral biological fluid is broadly applicable to other metal oxide and oxidative inorganic sensors for biologically relevant analytes including but not limited to ascorbic acid, dopamine, glycerol, ethylene glycol, and nitrite (*116*).

4.4 EXPERIMENTAL SECTION

Glucose Sensor Fabrication: Glass slides were sonicated for 20 min in 80% v/v acetone and 20 % v/v iso-propanol (IPA), and dried with N2. S1813 (Dow chemicals) photoresist was deposited on top of the glass substrates, following standard protocols (Spin-coated at 3000 RPM, baked 1 min. at 110 ^{o}C), to create the Au patterns. A 5 nm

Titanium adhesion layer and a 120 nm Au layer were evaporated on glass microscope slides. Deposition of photoresist was repeated prior to each electrodeposition following the same process. To increase the sensitivity of the sensor, we increased surface area of Au strip a process adapted from Lang et al. (*106*). Nanoporous Au was produced by electrochemically etching the 100nm thick Au layer with a solution of 1.5M ZnCl2 in Benzyl Alcohol at 120°C. To cycles of a cyclic voltammetry routine from -0.4V to 1.7V vs AgCl was performed with Zn wire reference and counter electrodes and a Metrohn Autolab Potentiostat (PGSTAT128N). This routine corresponds to two rounds of Zn-Au alloying/dealloying. The devices were then washed with 0.1M H2SO4, IPA, and di-water. This treatment was only performed on the contact destined for cobalt oxide. The nanoporous Au has higher capacitance resulting from a larger surface area. Cobalt Oxide was deposited from a solution of 5mM Cobalt(II) Nitrate suspended in 0.1M H_2SO_4. A CV routine (-1.2V to -0.2V) with a glass AgCl reference electrode and a Pt wire counter electrode. This was performed with a Metrohn Autolab Potentiostat (PGSTAT128N). To deposit Pd, we used 10 wt.% Palladium Nitrate ($PdNO_3$), purchased from sigma, and diluted with di-water to give a 1 wt.% PdNO3 solution. PdNPs were electrochemically deposited onto the Pd contacts using a DC voltage of V = -0.3V with a deposition time of 3 seconds with a glass AgCl reference and Pt counter electrode (**Fig. 4.10**). This resulted in a darkening of the contacts where the NPs were successfully deposited. The Pd nanoparticles have an increased surface area which greatly enhances the pH change effect over planar Pd and area stable over many pH cycles (**Fig. 4.11, 4.12**). To create the Ag/AgCl electrode, we electrodeposited Ag on

top of the Au contact in the reference electrodes by using a constant current of 0.5mA for 15s (outer contact) and 0.15mA for 150s (inner contact), from a solution containing 50mM of $AgNO_3$ and 0.2M sulfuric acid in di-water. A glass Ag/AgCl (V ~ 0.2 vs SHE) electrode was used as a reference electrode and Pt wire was used as a counter electrode. CV was used to form AgCl on the Ag, by using a solution containing 0.5M NaCl in di-water. 5 cycles were carried from -0.5 to 0.9V with a scan rate of 50 mV/s (**Fig. 4.10**). An SU8 photoresist layer was patterned to insulate the Au interconnect and define the area of the electrodes.

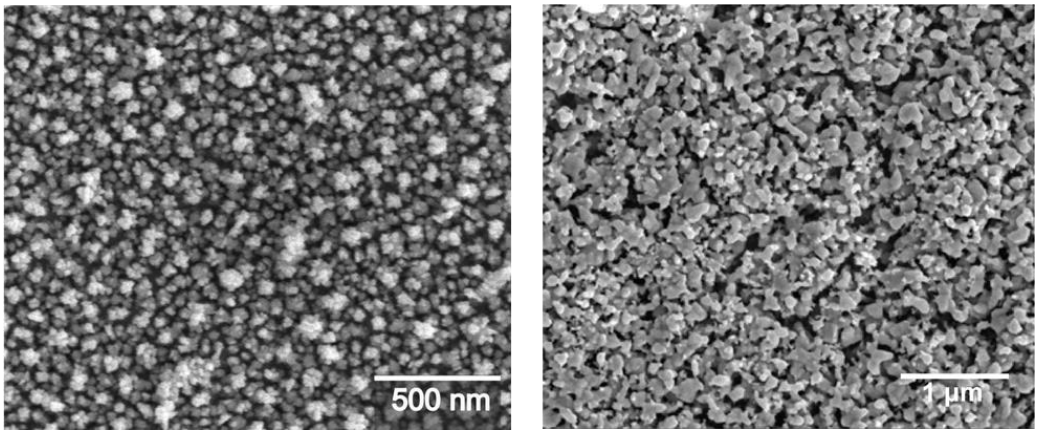

Figure 4.10. SEM images of nanoparticles. Pd Nanoparticles (left). Ag/AgCl nanoparticles (right).

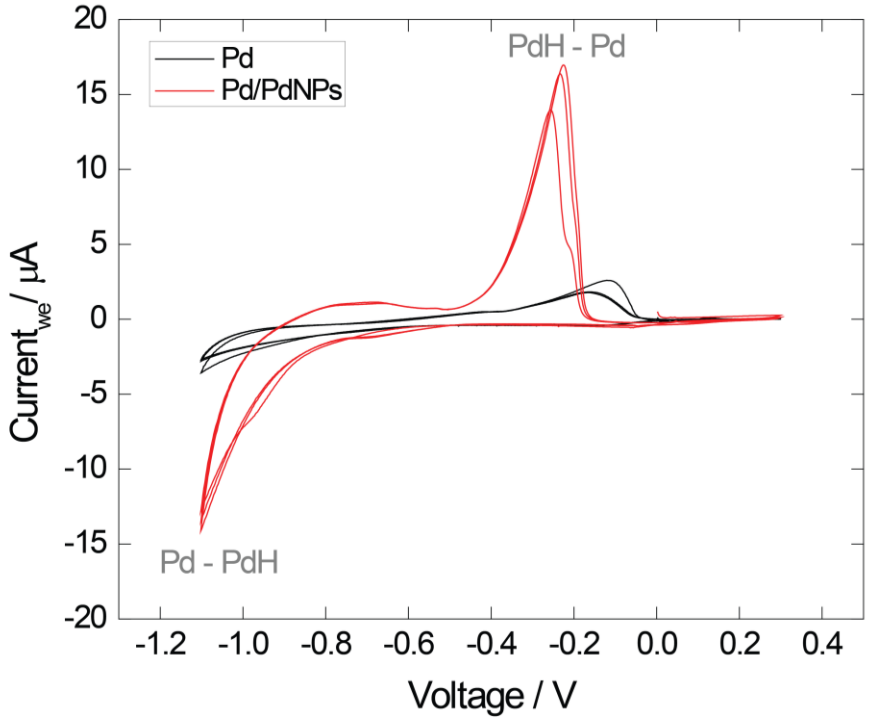

Figure 4.11. Cyclic voltammetry of a Pd contact versus Pd nanoparticles contact (250x250 µm) showing the increased performance of electrodeposited Pd. *The current which corresponds to the H^+ transfer between solution and Pd is higher for electrodeposited Pd.*

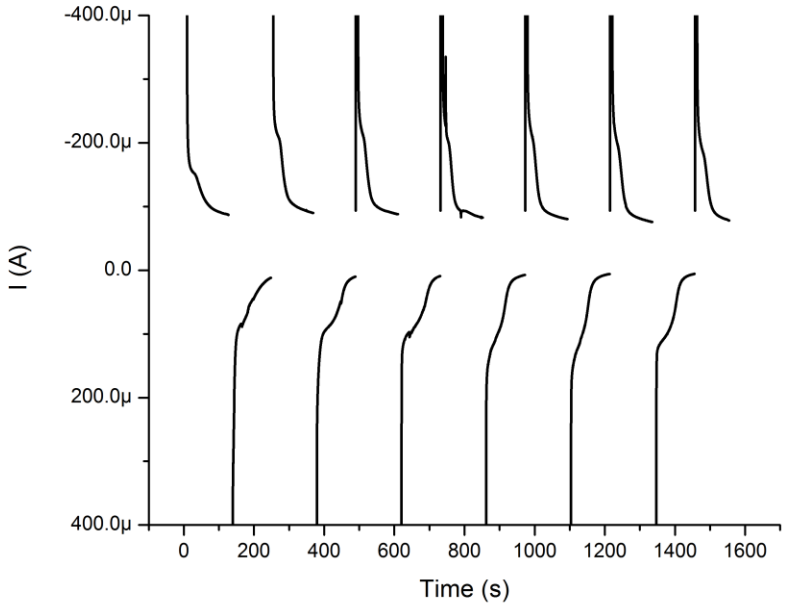

Figure 4.12. Current recording from Pd contact during pH cycling. *The Pd contact was switched between -1V and +0.3V vs AgCl. The current is reproducible for multiple cycles.*

Characterization of Cobalt Oxide Contact: The planar Au, nanopourous-etched Au, and nanoporous Au/Co3O4 coated surfaces were characterized by cyclic voltammetry in 0.1M NaCl solution (pH 7) vs a glass AgCl electrode (**Fig. 4.13**). A CV current typical gold profile (black) is amplified when the surface area of the contact is increased after etching (blue). After deposition of Co_3O_4, the recorded current is lower than that of the nanoporous Au as a result of the oxide film being more resistive, this is true until a broad peak at 0.5V which is characteristic of further oxidation of Co_3O_4.

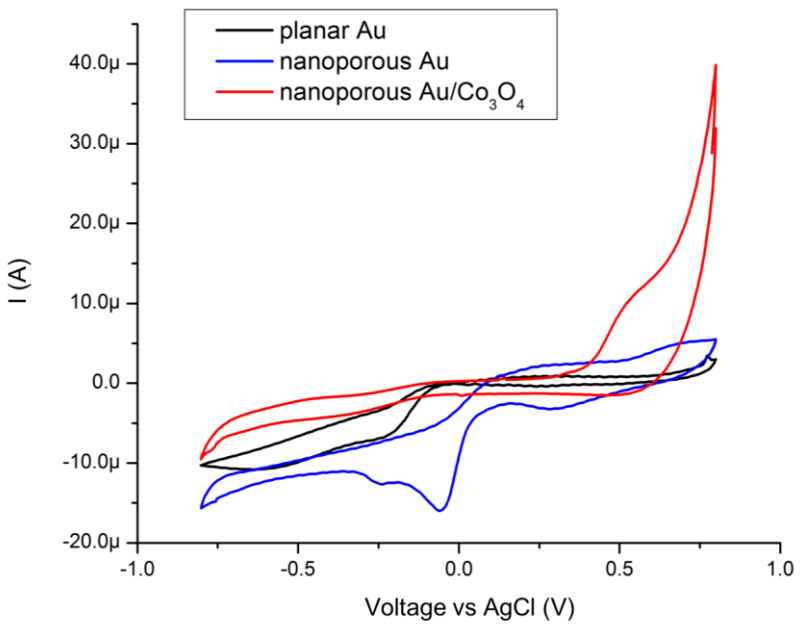

Figure 4.13. CVs on cobalt oxide contact*. Cyclic voltammetry of planar Au, nanoporous Au, and nanoporous Au/Co_3O_4 in 0.1M NaCl in the absence of glucose.*

pH Control and Characterization: pH cycling was controlled with an Autolab potentiostat connected to the Pd contact and an external AgCl pellet (electrode potential value V=0.21 vs standard hydrogen electrode). The quantification of solution pH was recorded with a micro-pH meter (Fisher Scientific). Diffusion of pH in the Co_3O_4 was recorded with a Keyence VHX-5000 series digital microscope. The solution was 0.1M NaCl initially at pH 7 with a universal pH indicator dye (Fisher Chemical) at a volume of 0.1mL.

Electrical Characterization (CV): Device characterization was done utilizing both an Autolab potentiostat and national instruments (NI) PXI with a digital multimeter (DMM) and a source measurement unit (SMU). A custom labview program was controlling the NI system. Potentiostat tests were run to gauge the performance of the devices, cyclic voltammetry, and frequency response analysis (FRA).

Glucose Measurements - NI and Potentiostat: pH cycling was controlled by an Autolab potentiostat connected to the on-chip Pd and AgCl electrodes. The on-chip cobalt oxide-AgCl circuit was controlled with an NI PXI with a digital multimeter and source measuring unit. Measurements began initially in 0.1M NaCl in di-water. During cycling of pH, glucose concentration was increased during periods of pH 7.

Glucose Measurements – Microchip: The board consists of two layers (sides). The WI-FI-enabled microcontroller (Espressif Systems microcontroller ESP8266) is installed on the "front" side while the rest of the electronics on the "back" side. This include: (i) an analog amplifier INA122U Texas Instruments, (ii) a 16-bit analog-to-digital converter (ADS1115 - Texas Instruments), (iii) a multiplexer (Texas Instruments TS5a4624) which together with a fixed +1.4V power supply circuit (ABLIC S-13R1A14) and an adjustable (+0.1 to +3.2V) adjustable power supply circuit (Microchip MCP601OT) we obtained the voltages required for the excitation (+0.3V and -1.1V), (iv) a power supply (Microchip MCP601OT) for the sensing circuit, (v)

two opto-isolator components (Vishay Semiconductor VOS618A) to separate the sensing and excitation sides of the circuit board. Measurements were performed between the on-chip Pd contact and an external AgCl pellet and the on-chip Co3O4 contact and an external AgCl pellet. Measurements began initially in 0.1M NaCl, glucose concentration was increased during periods of pH 7.

5. IONTRONIC ACTUATORS

5.1 ION PUMPS INTRODUCTION

This section will present developments on one form of iontronic actuator known as ion pumps. Ion pumps are devices that perform precise electrophoretic delivery of ions the device and a target solution. Ion pumps typically have at least one IEM that facilitates charge selectivity through electrostatic repulsion. Bipolar IEMs can also be used to reduce the effects of passive diffusion of ions down their concentration gradients through Donnan exclusion. The electrophoretic transport of ions across these membranes under an applied electric field occurs through ionic drift and diffusion as discussed previously.

Ion pumps are a promising technology as iontronic biomedical interfaces because of their ability to perform spatiotemporal delivery of ions and charged molecules without requiring significant volume change in the target solution. Research on ion pumps has been ongoing since the mid-2000s when the Berggren group introduced a Ca^{2+} organic electronic ion pump device capable of modulating the activity of neurons cultured *in vitro* on the device (*117*). In the years since, devices have been developed for injecting cations, anions, small charged molecules and neurotransmitters, and larger molecules. Ion pumps have been developed in different form factors planar devices for *in vitro* applications, implantable probes for *in vivo* applications, and even applications for interfacing electronics with plants (*118, 119*). The Rolandi group specializes in ion pumps for pH modulation and previously used these devices to modulate the activity of enzymes (*113*).

There are several key challenges of iontophoretic delivery with ion pumps. Achieving a high-enough rate of delivery to affect the target biology on a meaningful timescale requires optimized channel ionic conductivity, electrode charge injection capacity, operating voltage, channel length, and form-factor. This problem is enhanced for H+ type pumps that will operate in buffered conditions where the buffer capacity of the target solution needs to be overcome to alter pH. A challenge for *in vitro* applications with cultured cells involves integrating microfluidics for convective flow of cell culture media in the target solution in addition to all the components for the ion pump integration. Finally, the control methods for long term experiments on an ion pump must be considered as device fouling and the dynamics of a biological system's response to stimulation make open-loop control schemes sub-optimal. Addressing these challenges will enable ion pump technology to become a more impactful tool for biomedical scientists and synthetic biologists to treat human disease and create novel bioengineered systems.

Sections 5.2 is reproduced with permission from (*120*).

Section 5.3 is reproduced with permission from (*121*).

Section 5.4 is reproduced with permission from (*57*).

5.2 PROTON PUMP IN BUFFERED CONDITIONS

H^+ currents can be found in proton gated ion channels (*71, 72*) and proton pumps; (*122*) often these currents are coupled to the movement or generation of other chemical species such as in oxidative phosphorylation (*123*). The H^+ concentration (pH) within a cell affects enzymatic activity, (*124, 125*) gene expression (*126*), and is indicative of healthy cell function (*127*). pH regulation in the central nervous system maintains healthy neuronal function (*128*), and pH-affects neuronal excitability. Acidosis plays a role in self-termination of epileptic seizures (*129*). A common trait of cancer cells is a decrease of the extracellular pH due to overproduction of lactic acid, acid sensitive drug delivery vesicles use this mechanism to locally visualize and treat cancer cells and tissue (*130, 131*).

To induce alkalosis and increase pH, a bioelectronic device needs to specifically absorb H^+ ions without changing the concentration of other ions in solution. Pd contacts are able to specifically transfer H^+ to and from solution and proton conducting polymers exploiting the specific and reversible Pd/PdH_x reaction (*112, 113*). In this fashion, our group has demonstrated localized acidosis and alkalosis to control the rate of enzymatic reactions and bioluminescence (*112, 113*). However, these devices lack the dynamic range of the iontronic H^+ pumps that allows to lower the pH in solutions with high buffering capacity such as brain fluid ($\beta = 2.3x\,[HCO_3^-] \sim 60$ mM) (*128*). Here, we combine the large dynamic range of iontronic type H^+ pumps with the specificity of

Pd/PdH_x contacts (*132*, *133*) in a H^+ pump that is able to induce both acidosis and alkalosis in solutions with high pH buffering capacity (**Fig. 5.2.1**).

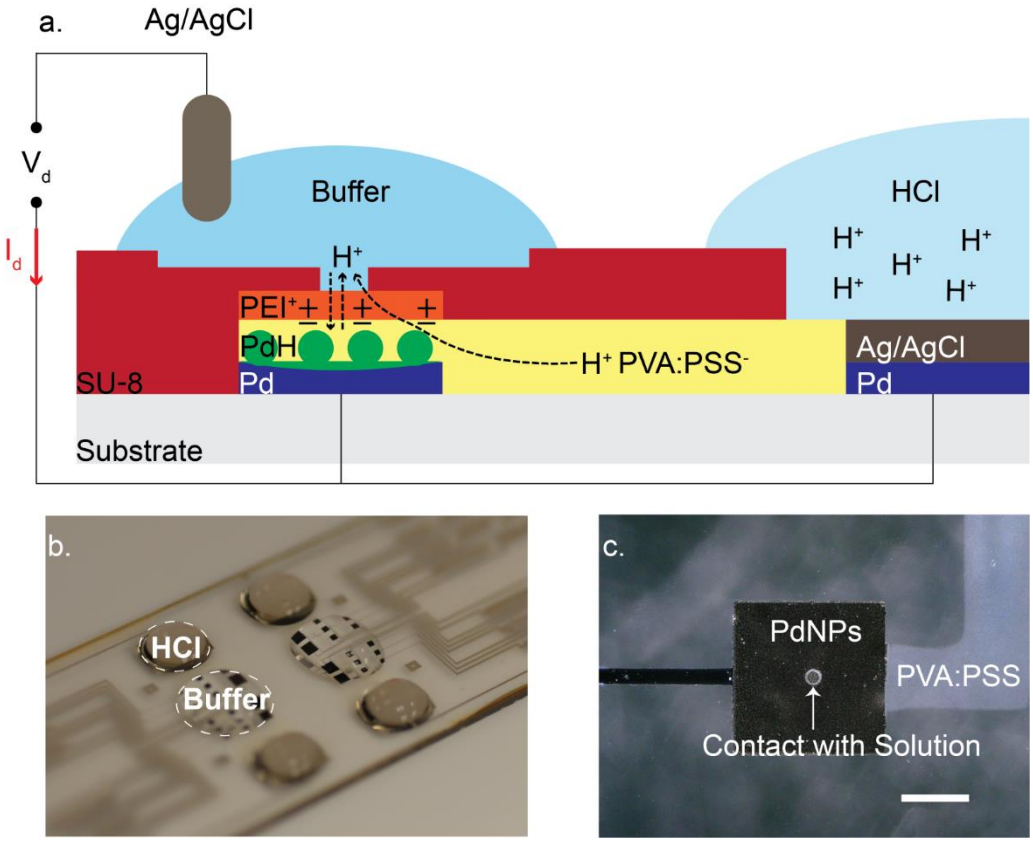

Figure 5.2.1. Bioelectronic H^+ pump design. *a) Schematic and operating principle of bioelectronic H^+ pump,. Two electrolyte chambers are connected with an H^+ conducting membrane. A high [H^+] solution (right) is at the interface with a modified Pd/Ag/AgCl. A buffer solution (left) is at the interface with PdNPs and an Ag/AgCl pellet immersed in solution. Application of V_d = 1V between PdNPs-Pd/Ag/AgCl and Ag/AgCl pellet decreases the buffer potential with respect to reservoir, and H^+ are transferred from the reservoir (right) into the buffer solution and*

thus decrease its pH. Application of V_d = -1V increases the potential of the buffer solution, and H^+ are transferred and stored into the PdNPs, thus the pH of the buffer solution is increasing. b) Perspective photo of the device showing the reservoir loaded with acid (HCl) on top of the Pd/Ag/AgCl electrode and the active area with buffer on top of the PdNPs electrodes. c) optical image showing a close up of a PdNPs contact, the proton bridge, and SU8 pore (40 μm) at the PdNPs/solution interface, scale bar 200 μm.

5.2.1 RESULTS

The H^+ pump, involves independent electrolyte chambers connected by a proton conducting bridge. One electrolyte, consisting of 0.5M HCl is used as a proton source (reservoir) and is in direct contact with a Pd contact modified with Ag/AgCl. The other electrolyte (target) is a buffer solution in which we induce pH modulation. The buffer electrolyte is in direct contact with sixteen square Pd nanoparticle (PdNP) contacts (twelve electrodes with an edge of 400 μm, and four electrodes with an edge of 1mm) and an Ag/AgCl pellet (**Fig. 5.2.1a** and **5.2.1b**). The contacts are used as multiple inlets for H^+ to enter the buffer solution in order to modulate the pH in a homogenous way. A positively charged membrane was patterned on top of the Pd contacts and between the cationic bridge and the buffer solution in order to reduce undesirable H^+ diffusion from the reservoir to the target electrolyte. Finally, an epoxy resist (SU8) was used to separate both the target solution and proton reservoir, insulating the H^+ bridge and the

Pd interconnects from external stimuli. The SU8 allows for an inlet pore of a tunable size between buffer and PdNPs (**Fig. 5.2.1c)**.

The H+ pump uses one input voltage (V_d) between the Ag/AgCl pellet and the PdNPs contacts in order to increase or decrease the pH. The PdNPs contacts are held at the same potential with the modified Pd (electrodeposited Ag/AgCl on top of the Pd) contact in the reservoir (short circuit) (**Fig. 5.2.1a**). When a negative V_d = -1V is applied between the PdNP contacts and the Ag/AgCl pellet, H^+ are transferred from the buffer solution into the Pd contacts, forming Palladium Hydride (PdH_x), with x being the atomic ratio of H to Pd and its maximum value can reach to 0.6-0.7 (*134, 135*). This results in a reduction of the proton concentration in the buffer electrolyte, thus, increase of its pH.(*113*) When the V_d is reversed (V_d = 1V), H^+ are transferred from the reservoir solution, through the cationic selective bridge, to the buffer solution and decrease its pH.

In the target electrolyte, Pd contacts were modified with Pd nanoparticles through electrodeposition, to increase the surface area, capacitance, and the ability to transfer H^+ and modulate (**Fig. 5.2.2a**). A negative voltage (vs. Ag/AgCl) applied to the Pd contact as working electrode and a Pd wire as counter electrode deposits PdNPs in the presence of a $PdNO_3$ solution. We optimized the process by measuring the impedance of the contact at the end of the deposition. For a Pd contact of 400 μm, applying a voltage V = -0.6 V for 0.1 seconds deposits PdNP and increases the surface area by

~20 fold (**Fig. 5.2.2b**). For longer deposition times, PdNP start aggregating thus reducing the surface area. We characterized the modified PdNPs contacts with Cyclic Voltammetry (CV) in a (*4-(2-hydroxyethyl)-1-piperazineethanesulfonic acid*) HEPES buffer solution. We cycled the voltage of the PdNPs contact between positive and negative values, versus an Ag/AgCl reference, for multiple cycles to monitor capacitive ionic currents and currents from interfacial reactions of the working electrode. In the case of Pd and PdNPs in HEPES, the main interfacial reaction between -1.1V and 0 V is the absorption and release of H^+. In the PdNPs the number of H^+ transferred at the PdNPs/electrolyte is 10 times higher than for the pristine Pd contact as measured by the current in the CV. (**Fig. 5.2.2c**). Threshold voltages for H^+ are also lower for PdNP. Absorption of H^+ into PdNPs begins at V = -0.73V compared to planar Pd at V = -0.8V. The release of H^+ starts at V = -0.4V compared to V = -0.3V for planar Pd. Additionally, the slope of the current $dI/dV = G$ for the transfer of H^+ into the electrolyte is ~20 times larger than for planar Pd. As a result of the more efficient H^+ transfer characteristics, the PdNPs contacts modulate the pH in buffer conditions at least 10 times more than a planar Pd contact. A 250 μm square PdNPs contact induces a dpH ~ 0.5 in 1μl of a HEPES (β = 23 mM), compared to a negligible change in pH induced by planar Pd (**Fig. 5.2.2d**).

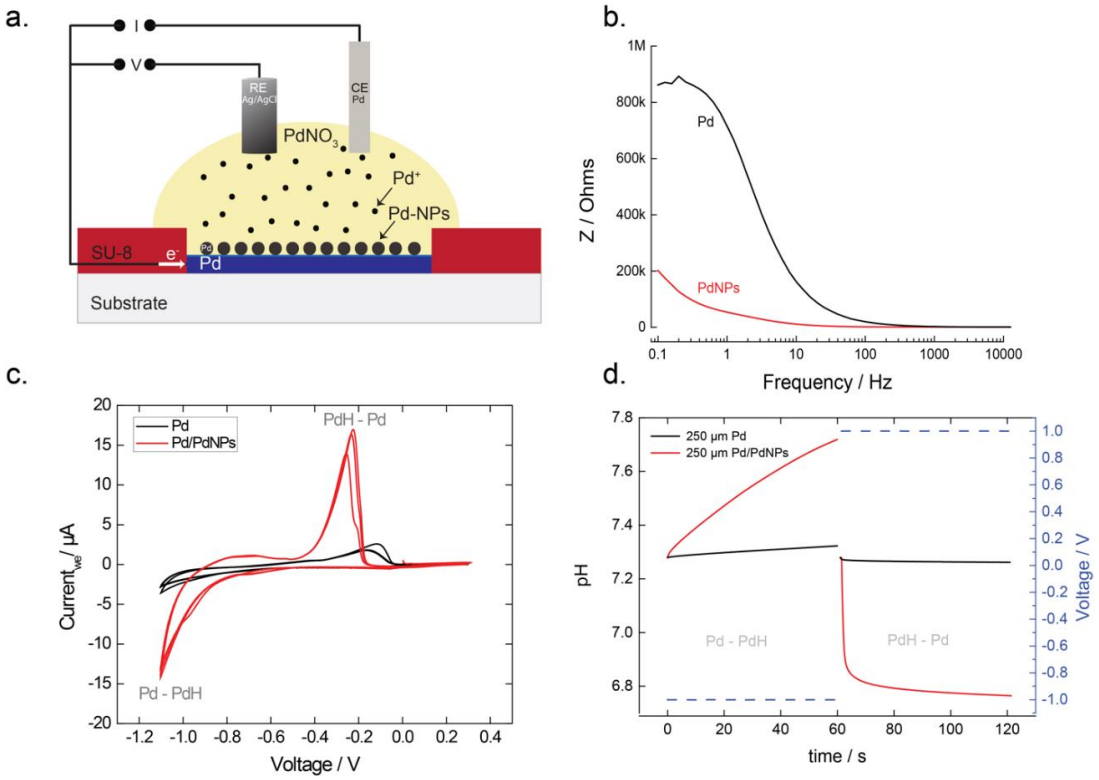

Figure 5.2.2. Electrodeposition of PdNPs on top of Pd. *a) schematic showing the electrodeposition. In the presence of $PdNO_3$, a negative voltage of V = - 0.6 Vs Ag/AgCl reduces the Pd cations on top of Pd and creates PdNPs b) impedance measurements of PdNPs modified contact and a Pd contact. The PdNPs contact exhibits a lower impedance, which means higher capacitance/surface area c) CV of a 400 µm Pd and PdNPs modified contacts in HEPES buffer. The CV shows the voltage regimes of H^+ transfer into the (Pd–PdH) and H^+ transfer to the electrolyte (PdH-Pd). Additionally, the current magnitude for PdNPs electrode is ~10x higher. d) pH modulation of 1 µL HEPES from a 250 µm PdNPs and Pd contact.*

Figure 5.2.3 shows how the device modulates the pH towards acidic and basic conditions. The PdNPs contacts are fixed (short circuit) at the same potential with the Pd/Ag/AgCl contact at the reservoir solution. To operate the device as a H^+ sink (increasing pH), a negative voltage (V_d = -1V) is applied between the PdNPs-Pd/Ag/AgCl and the Ag/AgCl pellet. At this pH and potential difference, H^+ are transferred from the buffer solution into the PdNPs contacts. The current has a transient capacitive behavior, which is typical for Pd contacts during H^+ absorption and it is then stabilized to a constant negative value (**Fig. 5.2.3a**).(*113*) For every H^+ that enters the PdNPs contact, a Cl^- is transferred from the buffer into the Ag/AgCl in order for the solution to maintain charge neutrality. In the H^+ delivery mode (decreasing pH), a positive voltage (V_d = 1V) is applied between the PdNPs-Pd/Ag/AgCl and the Ag/AgCl pellet. During this step, H^+ travel from the reservoir to the buffer solution decreasing its pH.(*128*) The current is mainly resistive with a small initial capacitance, and a magnitude of 30-40 μA. The capacitive portion of the current can be attributed to negatively charged ions, mainly OH^-, that adsorb on the PdNPs a positive potential (**Fig. 5.2.4**).(*136, 137*) A much higher initial capacitive current occurs when the PdNPs contacts are preloaded with H^+ (**Fig. 5.2.5)**.(*134*) Consecutive pulses between V_d = 1V and V_d = -1V for 60 seconds (**Fig. 5.2.3a**) exhibit reproducible current behavior, and consequent pH oscillations. **Figure 5.2.3b** shows the pH changes for a 50 μl of HEPES buffer upon an applied V_d = 1V and V_d = -1V for 120 sec. The pH changes were calculated from the current by using the Henderson-Hasselbalch equation for the specific buffer.(*122*) The calculated pH is in agreement with the experimental

measurements of pH that were performed with a micro pH meter. The pH changes in **figure 5.2.3b** are calculated for the overall volume of the HEPES buffer. Transiently, the pH changes are largest close to the Pd contacts, and subsequently propagate by following diffusion reaction phenomena.

Figure 5.2.3c and **5.2.3d** show localized pH changes that are induced by individual PdNPs contacts. A basic pH is induced on top of a PdNPs contact (blue), when V_d = -1V (**Fig. 5.2.3c**). The pH close to the PdNPs contact is higher compared to bulk of the solution, this pH gradient will slowly diffuse throughout the bulk solution until equilibrium is reached. When the voltage is reversed (V_d = +1V), the pH locally changes from basic (blue) to acidic (red) on top of the Pd contact (**Fig. 5.2.3d)**. This illustrates the contribution of a PdNPs contact that is preloaded with H^+ towards higher and faster local pH modulation, because the release H^+ back in the electrolyte and subsequently adsorb OH^- on their PdNPs surface. By controlling parameters such as the duration of the input voltage and number of PdNPs contacts, the H+ pump can achieve global and local pH changes in biological buffers.

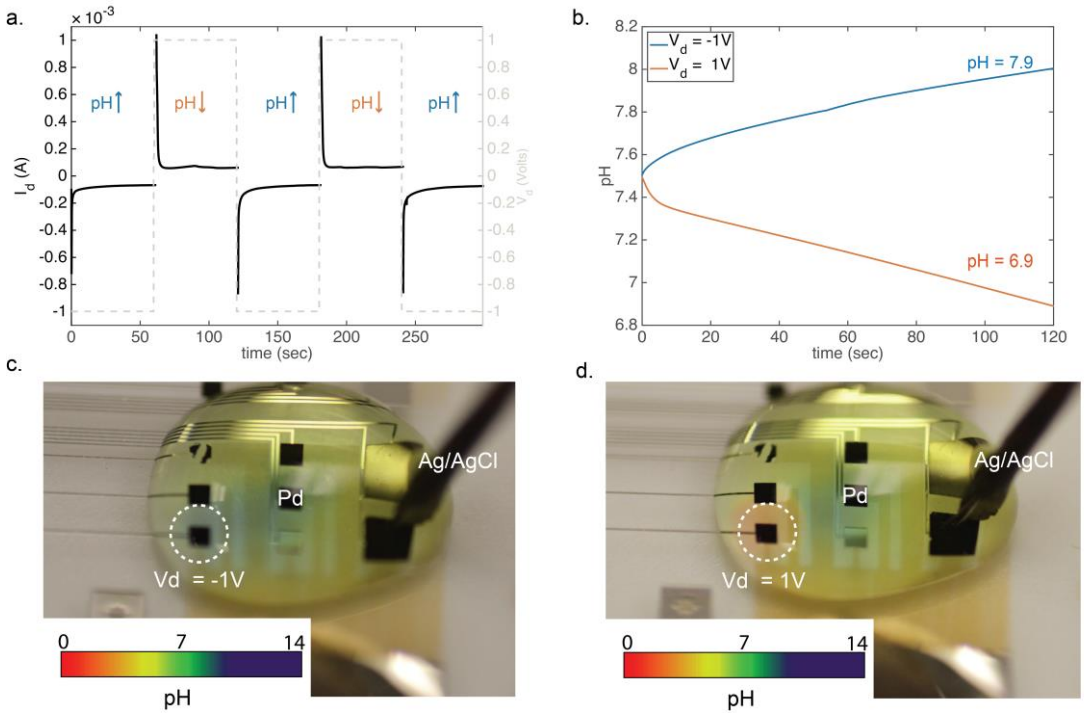

Figure 5.2..3. Protonic pH modulating circuit in action. *a) To increase the buffer pH, a negative voltage V_d = -1 V is applied between PdNPs-Pd/Ag/AgCl contacts and the Ag/AgCl pellet in the buffer electrolyte transfers the H^+ into the PdNPs. The resulting I_d has a typical Pd-PdH behavior with steady state of -40 μA. To decrease the pH, a positive voltage V_d = 1 V between the PdNPs-Pd/Ag/AgCl and the Ag/AgCl electrode in the buffer electrolyte transfers the protons from the reservoir into the buffer electrolyte. b) Calculated pH for V_d = - 1V (blue) for 120 sec and V_d = 1V (acidic) for 120 seconds on HEPES buffer. c) Optical image showing basic pH (blue color) in HEPES buffer with a pH indicator from an individual PdNPs contact. d) Optical image showing acidic pH (red color) in HEPES buffer with a pH indicator from an individual PdNPs contact.*

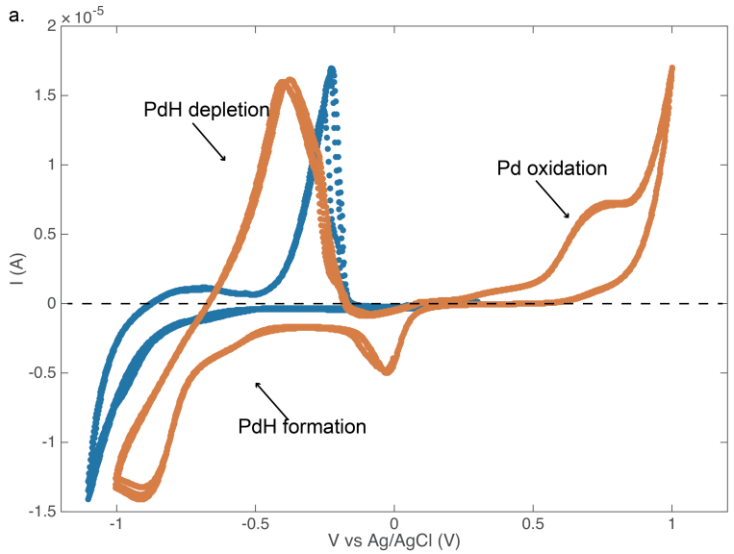

Figure 5.2.4. Behavior of PdNPs contact. *CV of PdNPs contact vs Ag/AgCl shows a oxidative current from starting from 0.7 V until 1V(orange). This current is attributed to the OH^- adsorbing on the surface of the Pd.*

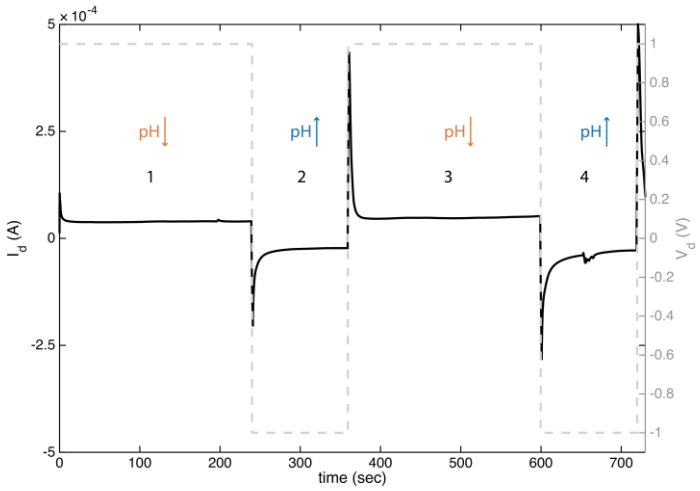

Figure 5.2.5. Proton pump creating initially acidic pH. *When PdNPs have not absorbed H^+ into their structure (pure Pd), the current is mainly resistive with a small initial capacitance (curve 1). The initial capacitance can be attributed to the OH^- adsorption onto the PdNPs surface. After loading the PdNPs with H^+ (curve 2), the current has a higher initial capacitance (curve 3) due to the combination of H^+ release from PdH_x and subsequent OH^- adsorption.*

To demonstrate the ability of our device to control pH in physiologically relevant conditions, we used acid-sensitive microparticles loaded with a pH sensitive dye fluorescein diacetate (FDA) in buffered conditions as a proof-of-concept target. By switching the environment between basic and acidic conditions we observed the degradation of the microparticles, release of FDA, followed by hydrolysis in basic conditions to fluorescein yielding an increase of the dyes fluorescence (**Fig. 5.2.6a**). The microparticles, which are based on dextran tagged with rhodamine, were

synthesized as previously described.(*131*) The microparticles, with average size of 2 μm and concentration of 1mg/ml, were dissolved in HEPES buffer of pH 7.4 and then were exposed to four conditions; control groups in solutions set at physiological pH 7.4, acidic pH 6, and basic pH 8, as well as a device modulated acidic then basic treatment switching the pH from neutral to acidic then to basic.

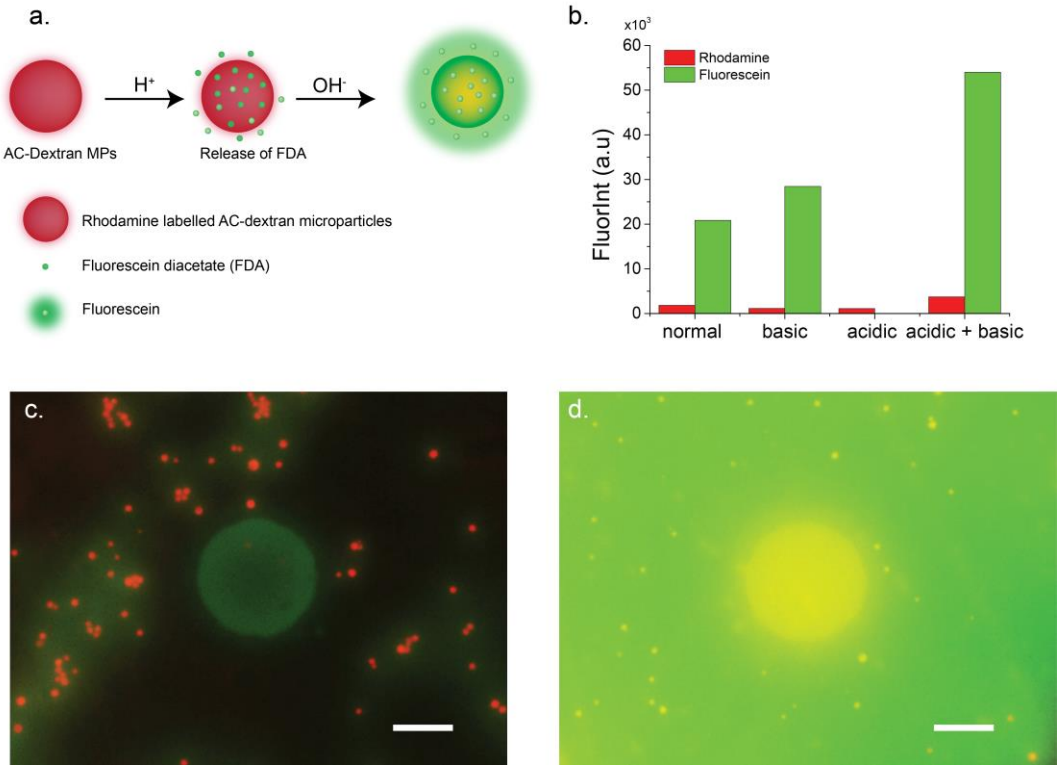

Figure 5.2.6. Degradation of acid sensitive microparticles with H^+ pump*: a) Schematic of dextran-based acid-sensitive microparticles. The microparticles decompose in acidic conditions and release fluorescein diacetate (FDA). Under basic conditions, FDA hydrolyses and is converted to fluorescein, which in turn shows increased fluorescence. b) histogram showing fluorescent intensity of microparticles (red) and released (green) fluorescein, in four different pH conditions: normal (pH 7.4), basic*

(pH 8), acidic (pH 6), acidic+basic (first pH 6, then pH 8). The pH changes were induced by the H^+ pump using 8 PdNPs contacts. 6 of them with size 400x400 μm and 2 of 1x1mm and openings of 100 μm. c, d) Overlay images showing both red fluorescence (red dots) of rhodamine labelled Ac-Dextran micro-particles and green fluorescence intensity (GFP) of fluorescein released from the particles on top of a PdNPs contact at pH 7.4 and at pH 6 and 8, respectively. Scale bar 50 μm.

To degrade the microparticles, acidic conditions were induced by applying V_d = 1V, in the presence of 20 μl of Ac-Dex MPs. After 180sec, The pH of the solution, which was monitored by a pH microelectrode, reached at pH 6. We incubated the solutions for 24 hours in sterile dark conditions, and then we induced basic conditions (pH 8) to hydrolyze FDA. **Figure 5.2.6b** shows the extracted fluorescence intensity of green (FDA-Fluorescein) and red fluorescence (Rhodamine) for the samples that incubated in the four different pH conditions. The green fluorescence intensity of the samples that were exposed to the acidic then basic conditions was the highest, validating both the degradation of the particles in pH 6 and the subsequent FDA hydrolysis. At pH 7.4, green florescence intensity was observed at the surroundings of the microparticles (**Fig. 5.2.6c**). at pH 6, green fluorescence is not detected (**Fig. 5.2.7a**). This is expected for two reasons, FDA is not hydrolyzed and fluorescein does not exhibit fluorescence at acidic pH.(*138, 139*) At pH 8, there is a higher green fluorescence intensity (**Fig. 5.2.7b**), which indicates that the Ac-Dex MPs release FDA, however, the intensity is half compared to the samples of interest (**Fig. 5.2.6d**). The fluorescence intensity in the

samples of interest is the highest, it has a homogenous distribution with highest intensity on top of the electrode surface.

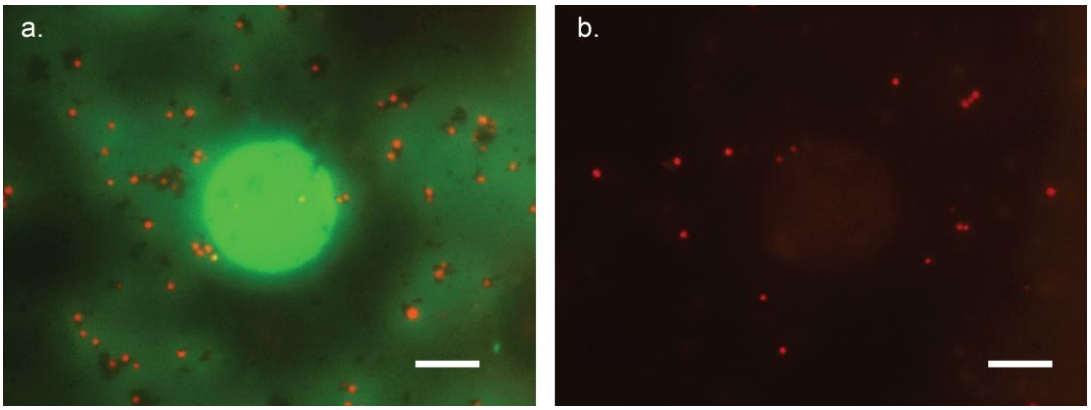

Figure 5.2.7. Acid sensitive microparticles degradation. *a) Overlay red fluorescence (red dots) of rhodamine labelled Ac-Dextran micro-particles and green fluorescence (GFP) of fluorescein released from the particles on top of a pore of a 100 um PdNPs contact in pH 8. pH was increased by the PdNPs contact upon a* V_d *= -1 V vs an Ag/AgCl pellet. b) Overlay red fluorescence (red dots) of rhodamine labelled Ac-Dextran micro-particles and green fluorescence intensity (GFP) of fluorescein released from the particles in pH 6 on top of the opening of a 100 um PdNPs contact. pH was decreased by upon a V = 1 V vs an Ag/AgCl pellet. Scale bars 50 um.*

5.2.2 DISCUSSION

The Pd based H+ pump is capable of both increasing and decreasing pH in buffered conditions. The H+ pump can increase and decrease pH with an electronic input, V_d.

This pump is based on an array of Pd contacts modified with Pd nanoparticles to increase surface area and contact capacitance. These contacts are connected to a H^+ reservoir via a polymer proton conducting bridge. The H^+ reservoir affords a large supply H^+ for extended pH modulation. As a proof of concept, we stimulated the degradation of acid sensitive microparticles, by reducing the solution pH. The microparticles released FDA, a pH sensitive fluorescent dye, and by inducing basic conditions, the fluorescence of the dye was increased. The platform can repetitively control the pH in buffer conditions and can be used for a variety of applications including delivery of cargo to cells(*140*) and control of those biochemical reactions in which pH plays an important role.

5.2.3 EXPERIMENTAL

Device fabrication: Microscale H+ pump was fabricated using photolithography (**Fig. 5.2.8**). Glass slides were sonicated for 20 min in 80% v/v acetone and 20 % v/v iso-propanol (IPA), and dried with N_2. S1813 (Dow chemicals) photoresist was deposited on top of the glass substrates, following standard protocols (spin-coated at 3000 RPM, baked 1 min. at 110 ^oC), to create the Palladium (Pd) patterns. Chromium (Cr) 5 nm and Pd 100 nm were evaporated using an e-beam evaporator, and a lift-off process (sonication in 80% v/v Acetone and 20% v/v IPA for 5 min) defined the metal contacts and interconnects. An additional S1813 process defined the area of the Pd contacts for Palladium nanoparticles (PdNPs) deposition, while the metal interconnects were insulated. After PdNP deposition, the photoresist was

striped with acetone and the samples were activated with oxygen plasma 100 RF for 2 min.

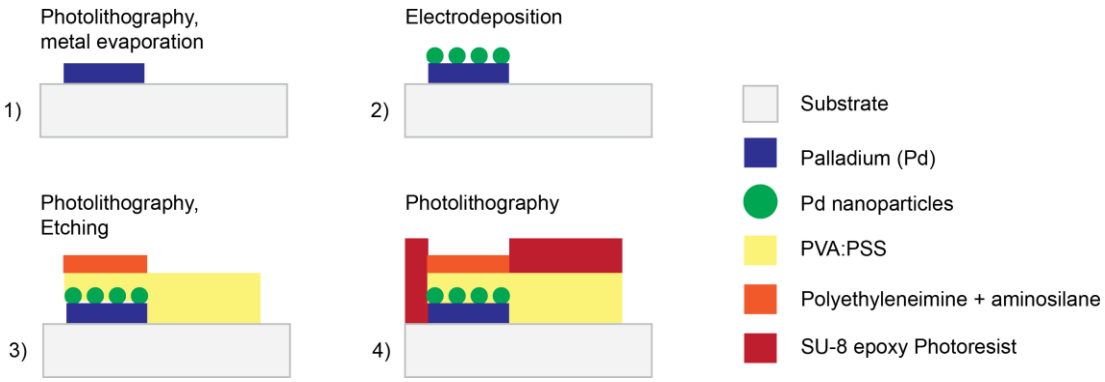

Figure 5.2.8. Fabrication process of the H^+ pump*. Step 1) photolithography and Palladium thin film evaporation. Step 2: photolithography for defining the Pd electrode and electrodeposition of Pd to create Pd nanoparticles. Step 3: photolithography to define the PVA:PSS bridge and the PEI:APTES selective membrane with subsequent O2 etching. Step 4: photolithography of SU8 photoresist to seal the interconnects and define the contact with the electrolyte.*

A blend of 8 wt% Polyvinylalcohol (PVA) with 2 wt% polystyrenesulfonic acid (4:1 weight ratio) was thoroughly mixed (PVA:PSS solution) and sonicated for 45 min. The PVA:PSS solution was filtered with a filter porous size of 0.8 μm and was spin-coated on top of the samples at 3000 rpm for 30 sec and baked in 120 ^{o}C for 45 min, yielding a film thickness of 800nm. A positive photoresist Dow SPR220-4.5 was spin-coated and patterned to define a pattern

for a polyethyleneimine (PEI) membrane which was spin-coated at 1000 rpm, with a ramp up of 200 rpm/s, for 30 seconds and then baked at 70 ^{o}C for 20 minutes. The PEI membrane was coated with an additional layer of S1813 (same process) to cover the area on top of the contacts. This layer was patterned with exposure to UV light for 12s at a power of 8mW/cm^2 and developed with MF26A developer for 90 seconds. The samples were etched with oxygen plasma (O2 15 sccm, Power 200 Watt for 11 min). A developed monolayer of GOPS on top of the glass was formed by chemical vapor deposition under vacuum in 90 ^{o}C for 2 hours. On top of this was spin-coated the final insulating layer of SU8-2005 at 3000 rpm for 30s

Pd Nanoparticles deposition: 10 wt.% Palladium Nitrate ($PdNO_3$), purchased from sigma, was diluted with di-water to give a 1 wt.% $PdNO_3$ solution. PdNPs were electrochemically deposited onto the Pd contacts using a DC voltage of V = -0.6V with a varied deposition time between 0.1 – 10 seconds. This resulted in a darkening of the contacts where the NPs were successfully deposited.

Ag/AgCl Nanoparticles deposition: Ag was electrodeposited on top of the Pd contact in the reservoir, by using a solution containing 50 mM of $AgNO_3$ and 0.2 M sulfuric acid in di-water, by using a constant current of 1mA for 160 seconds. Ag/AgCl electrode was used as a RE and Pt wire was used as a CE. Then CV was used to deposit chloride on top of the Ag, by using a solution containing 0.5 M NaCl and 0.2

M HCl in di-water. 5 cycles were curried from -0.45 to 0.9 V with a scan rate from 0.1V /second (data not shown).

PVA:PSS Bridge: The bridge was created by mixing PVA 10 wt.% in di-water with PSS 30 wt.% that resulted in a mass ratio of 4:1 with final PVA concentration 8 wt.% and PSS 2 wt.%. This 10 wt.% PVA (M_w ~89,000-98,000 99% Sigma-Aldrich) powder was dissolved in di-water while heating in a microwave oven for a total of 30 seconds, during which, at 5 second intervals the microwave was paused, and the solution was thoroughly vortexed. Upon continuous mixing, a 30 wt.% solution of Na^+PSS^- solution (Sigma Aldrich) was slowly added into the PVA, afterwards, the blend solution was sonicated for 45 min. Prior to the deposition the viscous solution was filtered with a commercial PET filter of 0.8 μm porous size.

PEI:APTES Membrane: To reduce unwanted H^+ diffusion, we patterned a 300nm thick membrane consisted of polyethyleneimine (PEI) crosslinked with 3-aminopropyltrimethoxysilane (APTES) at a weight ratio of (1:1) with a final concentration of 3 % weight ratio in di-water. In physiological and acidic pH, the positively charged amine groups of PEI and APTES repel positively charged H^+, acting as a barrier to undesirable H^+ diffusion. Crosslinked APTES groups stabilized the film. The positively charged PEI membrane solution was created by mixing Polyethyleneimine (PEI: M_w ~800 Sigma-Aldrich) with (3-Aminopropyl) triethoxysilane (APTES) at a weight ratio of 1:1 with the final

concentration of 3 wt.%. This mixture was spin-coated onto devices at 800rpm, with a ramp of 200rpm/s, for 30s and then baked at 60 ^{o}C for 20 minutes.

Characterization: Device characterization was done utilizing both an Autolab potentiostat and national instruments (NI) PXI with a digital multimeter (DMM) and a source measurement unit (SMU). A custom labview program was controlling the NI system. Potentiostat, tests were run to gauge the performance of the devices, cyclic voltammetry, and frequency response analysis (FRA).

Fluorescence measurements: All the fluorescence intensity measurements were performed by a Keyence BZX microscope and analyzed with an ImageJ software**.**

Synthesis of pH sensitive AcDex Microparticles (MPs): pH-sensitive acetalated dextran (Ac-Dex) was synthesized by following and modifying a previously described method.(*131*)

pH-triggered MPs deformation: 1 mg/mL Ac-Dex MPs were dissolved in HEPES 10mM buffer (pH = 7.3). The particles were sonicated for 45min. For each measurement 20µl of solution was drop casted on top of the device. a negative V = -1V vs Ag/AgCl pellet was applied for 2 min, during which, the pH increased from the initial pH = 7.3 to pH = 8. The pH of the solution was monitored by a micro-pH electrode (Fisher Scientific).

5.3 CLOSED-LOOP PROTON PUMP FOR ACTUATION IN CELLS

Life is built upon closed-loop feedback and regulation systems that maintain a delicate balance of environmental and metabolic conditions that support cellular function (*141, 142*). Bioelectronic devices interface electronic devices with biology with potential for sensing and actuation (*17, 143-147*). A challenge for bioelectronic devices is translating between ionic and biochemical signals that dominate biology into electronic currents in the devices and vice versa. Iontronics addresses this challenge by modulating ions directly at the device level rather than electron and holes as in traditional semiconductors (*148*). Electrophoretic ion pumps mediate the delivery of ions and charged molecules with an induced electric field (*117, 149*) to treat epilepsy (*148*), chronic pain (*150, 151*), inflammation (*152*), and to actuate movement in plants (*153*). Additionally, bioprotonic devices can sense and actuate the flow of H^+ in field effect transistors (H^+-FETs) (*112, 154-156*), enzymatic logic gates (*112*), and ion channels (*157, 158*).

A cell's resting potential, V_{mem}, is an electrical control signal that occurs between the interior of the cell and the extracellular environment regulated by ion channels (*159-162*). In non-excitable cells (*163*), V_{mem} affects cell physiology and functions such as proliferation, differentiation, migration, and apoptosis, as well as cell-cell communication, and large-scale morphogenesis (*164, 165*). Recently, optically

actuated capacitors have achieved transient V_{mem} control in oocyte cells (*147*). The ability to control V_{mem} for long-term is an essential enabling step to the modulation of cell function, metabolism, and morphogenesis, especially in bioengineering, regenerative medicine, and synthetic morphology applications (*166, 167*).

Controlling cells with bioelectronics is difficult due to the complexity of cellular response to changing environmental conditions. Cellular processes are hard to model due to noise and uncertainty (*168, 169*). This complexity limits most examples of biocontrol to simplified systems such as synthetic gene networks engineered with feedback to achieve noise rejection and adaptation (*170-179*). As the complexity of biological systems scale up, the challenge of feedback design increases. Without a model, a standard approach to bioelectronic control would require information a priori of how the biological variable will respond to an electronic stimulus (*52, 180*). This information is often not available. In addition, such an approach does not account for potential adaptation in system response or unknown changes in the environment or device response. For example, the commonly used controller in practice, known as the Proportional-Integral-Derivative (PID) controller, might not function properly when the system under control is exposed to the uncertainties, nonlinearities, and unknown disturbances caused by undesired phenomena such as varying environmental conditions (*181-183*).

Machine learning (ML) has successfully controlled biological systems when offline training and large datasets are available a priori (*184-187*). However, deep-learning ML methods such as deep neural networks, deep recurrent neural networks, and generative adversarial networks are slow to update in response to system changes. Real-time ML-based methods, such as adaptive ML algorithms, in combination with tools from control theory learn and respond to different operational conditions (*188-190*) and are able to work with nonlinearities, noise, and system uncertainty that are typical of cells or bioelectronic devices. Here, we leverage a single layer neural network with a "sense and respond" (*191*) composed of radial basis functions (RBF). RBF act as universal approximators (*192*) and are fast converging, thus ideal for real-time control applications (*190, 193*).

Here, we demonstrate an array of bioelectronic proton pumps (*194, 195*) merged with an adaptive machine learning-based controller that can provide control of V_{mem} for an extended amount of time (**Fig. 5.3.1**). In brief, a bioelectronic proton pump array adds or removes H^+ from solution and changes $[H^+]$ in proximity of human induced pluripotent stem cells (hiPSCs) (**Fig. 5.3.2**). In hiPSCs, an increase in extracellular $[H^+]$ results in cell depolarization (lower V_{mem}) and a decrease in extracellular $[H^+]$ results in cell hyperpolarization (higher V_{mem}) (*196, 197*). We measure relative changes in V_{mem} of the cells using ArcLight, a fluorescent reporter for membrane voltage that we expressed on the cell membrane(*198*). To monitor and control the dynamics of V_{mem} in real-time, fluorescent images are taken at regularly spaced time intervals. To

set and maintain a specific V_{mem} value for a given cell, we control the system using a machine learning (ML)-based algorithm that maps changes in V_{mem} to prior H^+ stimuli from the proton pump. Using this information, the ML algorithm decides whether the $[H^+]$ surrounding a specific cell should be increased or decreased to achieve the desired V_{mem} value and sends a control voltage (V_{H+}) to the proton pump in the array thus closing the control loop. The algorithm is not trained on any data a priori and makes no use of a model for either the bioelectronic device or the fluorescently tagged hiPSCs. Based on the target goal and current state, the parameters of the neural network are updated in between the time-lapse fluorescent images such that the "learning" happens in real-time and the target V_{mem} is ultimately achieved.

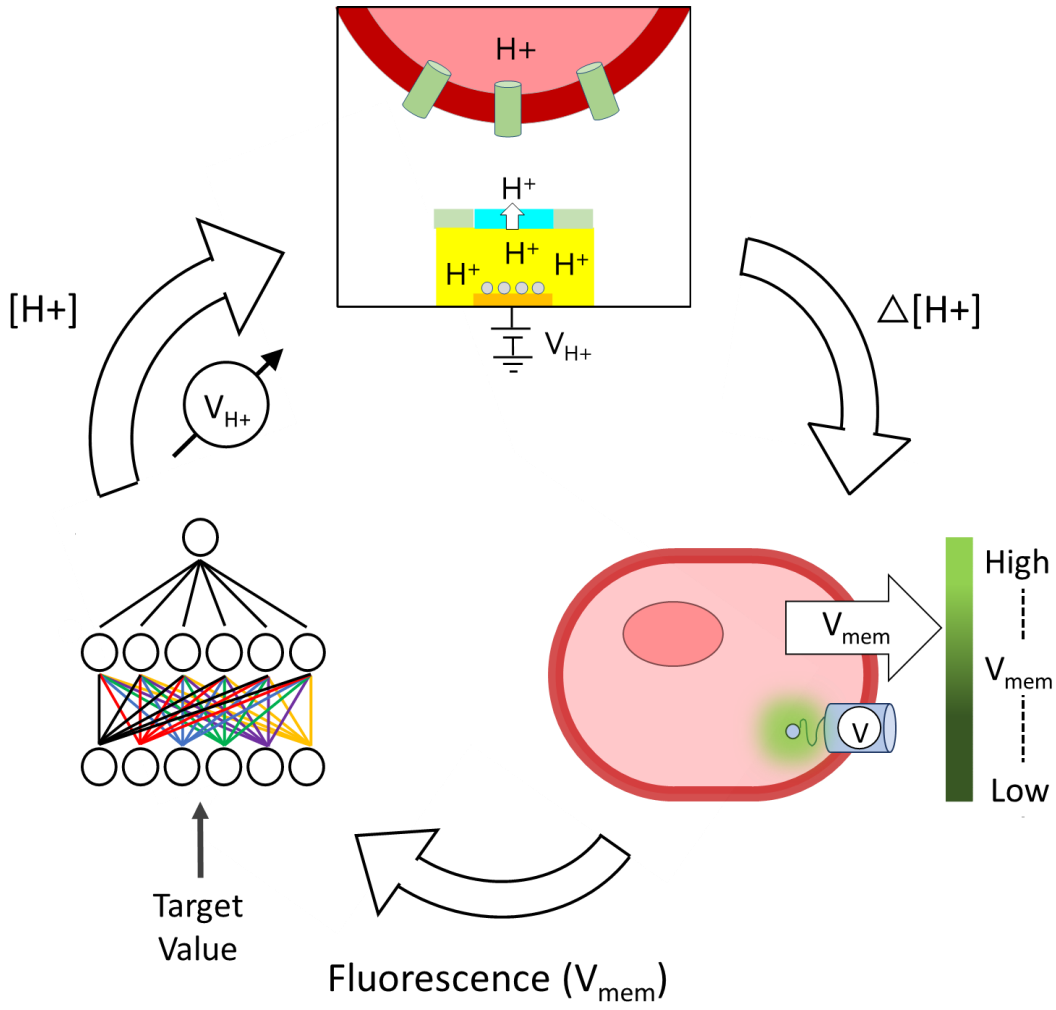

Figure 5.3.1. Closed-loop bioelectronic control of V_{mem}. *An adaptive learning algorithm controls a proton pump array to change the pH of extracellular fluid and alter V_{mem} to a target value, V_{mem} is measured by a fluorescent indicator for feed back to the control algorithm.*

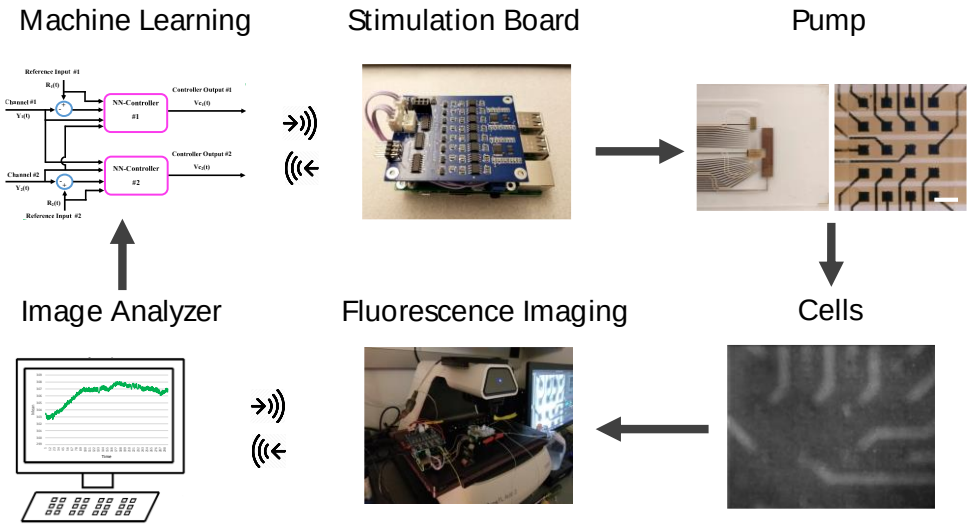

Figure 5.3.2. Subsystems of the closed-loop bioelectronic platform. *An adaptive ML algorithm communicates a control voltage wirelessly to a stimulation board which controls an array of proton pumps and induces pH gradients around hiPSCs. Fluorescence imaging is used to record the* V_{mem} *of these cells which changes in response to variation in pH, images are transferred to an image analyzer that samples regions of the image before being feedback to the ML controller.*

5.3.1 RESULTS

Each individual pump within the array is made of a Palladium/Palladium Hydride (Pd/PdH) contact that is able to transfer H^+ to and from the solution depending on an applied voltage V_{H+} (**Fig. 5.3.3A**) (*112*). Previously described proton pump arrays[*194, 195*] were fabricated on transparent substrates with integrated microfluidic channels to enable on-chip cell culture and monitoring of device performance and cell responses

via fluorescence microscopy. The reservoir and target chambers consist of two microfluidic channels with 40 μm tall side walls and a ceiling of transparent microfluidic tape. At the closest point, the reservoir and target chambers run parallel to each other with a distance of 1mm, with the ion bridge (brown lines) connecting the two solutions **(Fig. 5.3.3B)**. A 2 mm diameter window is excised from the microfluidic tape and aligned to the array of 100 μm x 100 μm proton pump array pixels aligned in a 5x4 grid with a 250 μm pitch in the target chamber prior to sealing the fluidics to allow for interfacing with removable polydimethylsiloxane (PDMS) slides through clamping (**Fig. 5.3.4**). The microfluidic channels allow for distinct electrolyte solution to be flown within the reservoir and target channels. Silver/silver chloride (Ag/AgCl) electrodes located in the reservoir and target channels are paired with the Pd/PdH electrodes located beneath the ion bridge at each pixel in the proton pump array to control ionic flux in and out of the device. A positive value for V_{H+} applied between the array pixel and the Ag/AgCl electrode in the target channel will release H^+ into the target channel thus increasing $[H^+]$ of the solution (**Fig. 5.3.3C**), a negative value for V_{H+} will absorb H^+ from the solution into the contact thus decreasing $[H^+]$ of the solution (**Fig. 5.3.3D**). A voltage V_{RES} between the array pixel and the reservoir can be used to move H^+ from reservoir to Pd contact forming PdH, which increase the efficiency of the proton pump by localizing H^+ to the array pixel although for the work presented here, only V_{H+} is used[194, 195].

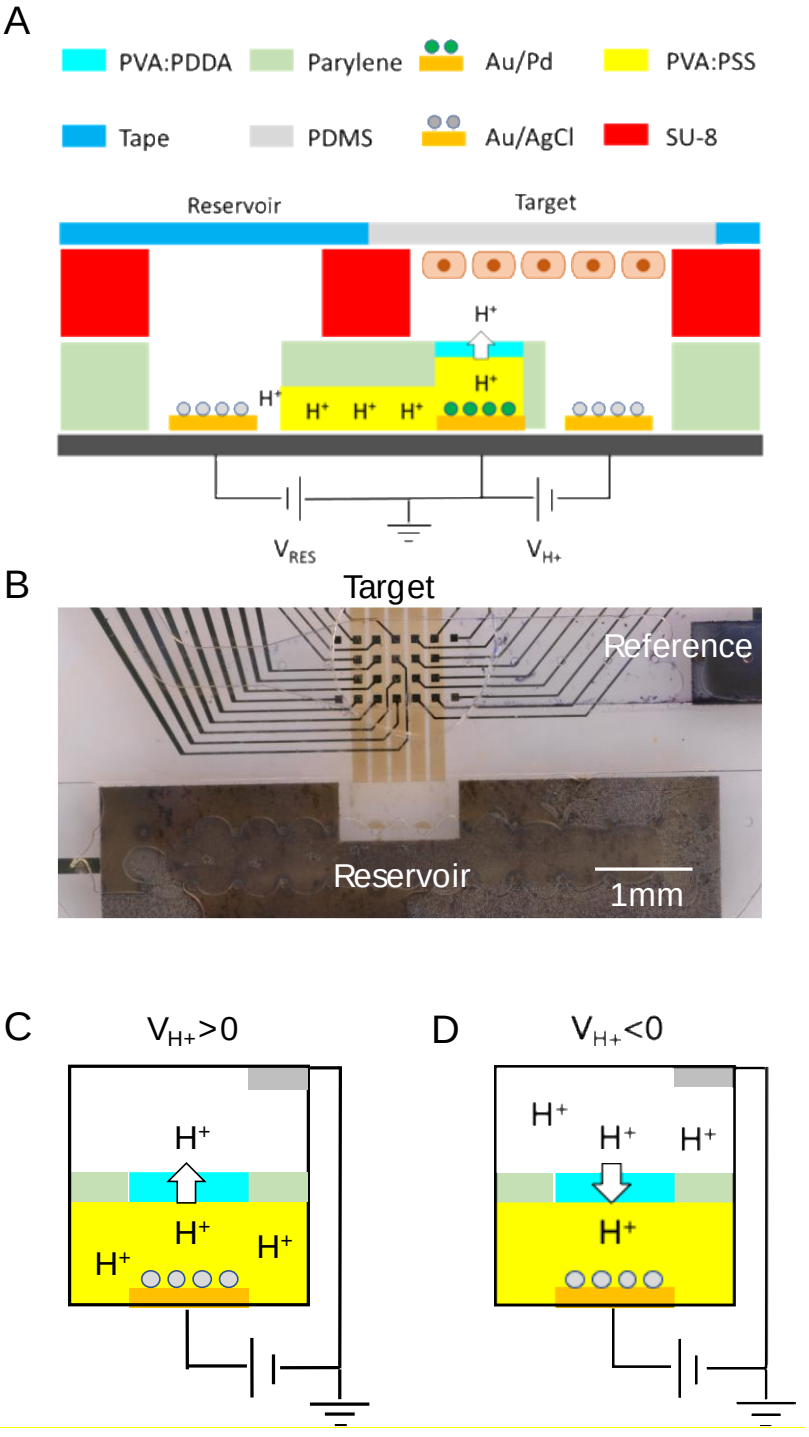

Figure 5.3.3. Proton Pump Design*. (A) Device schematic (B) Optical image of the proton pump array pixels with the PVA:PSS ion bridge. Scale Bar: 1mm. (C) Proton*

delivery to and (D) Proton removal from target solution upon applied bias V_{H+}, Ag/AgCl counter electrode is drawn out of plane for simplicity.

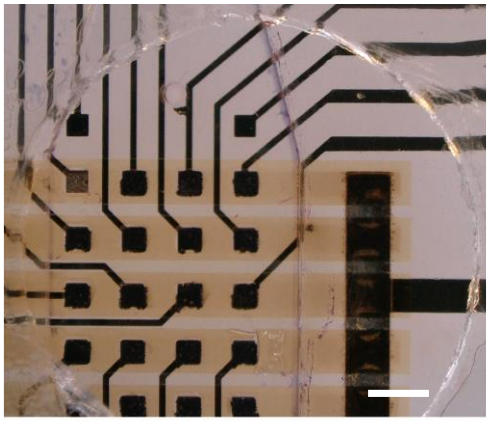

Figure 5.3.4. Optical images of the proton pump array with microfluidic tape sealing the fluidic channel. *A 2mm diameter hole is excised from the tape over the array to allow interfacing with stem cells. Scale bar: 250 μm.*

Given that cells and their associated V_{mem} are highly sensitive even to very small changes in $[H^+]$, we first demonstrate that we can precisely set $[H^+]$ in a desired location at a given time so that a specific $[H^+]$ value is regulated in the extracellular fluid (**Fig. 5.3.5**). To do so, we drive the proton pump with a ML-based control algorithm consisting of a radial-basis function-artificial neural network. In this case, $[H^+]$ response from an area of interest that is mapped using a dye whose fluorescence is inversely proportional to $[H^+]$ (SNARF) (*199*). The algorithm leverages a neural network comprised of an input layer, a hidden layer, and an output layer (**Fig. 5.3.5A**). The input layer receives the error value between the desired and the measured $[H^+]$ values, information on prior [H+] stimuli, as well as, current and previous $[H^+]$ response to the applied V_{H+}. The desired output consists of desired values at time k+1,

k, and k-1, and the measured output consists of measured values at time k-1, k-2, and k-3.The hidden layer converges to a mapping that allows it to discern which value of V_{H^+} should be applied to the individual proton pump surrounding the area of interest to achieve the desired [H^+].

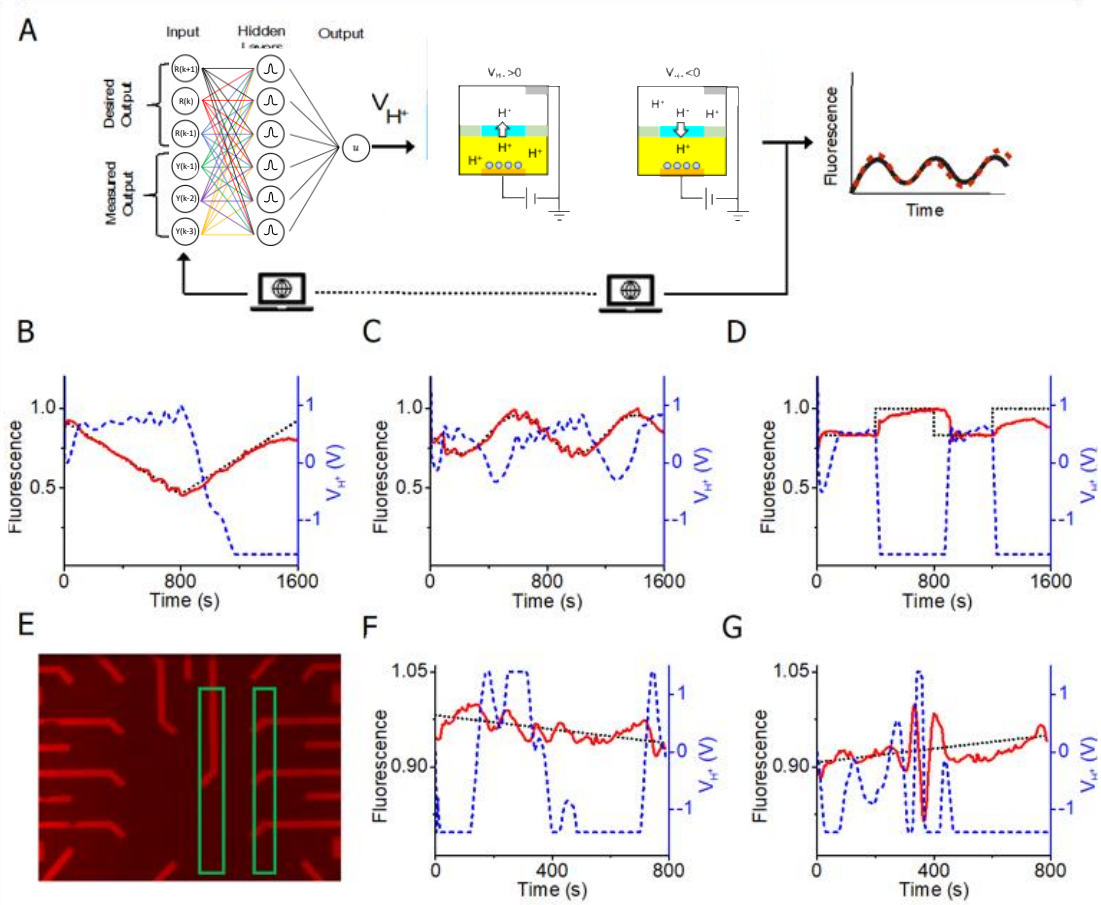

Figure 5.3.5. Control of H^+ pump with machine learning controller generates pH gradients in buffered media. *(A) A schematic of the experimental setup, the H^+ pump array induces pH gradients in solution upon stimulation by a stimulation board. Fluorescence signals from pH sensitive dye SNARF-1 in media are captured and fed into a neural network machine learning algorithm which attempts to control the*

stimulation board voltages to match a prescribed fluorescence pattern. Temporal control of pH monitored through the fluorescence response of SNARF-1 dye over the actuated column of proton pumps (red traces) maps to the target triangle (B), sine (C), and square (D) waveforms (black dotted traces). V_{H+} *(blue dotted traces) for these waveforms responds to the error in the experimental fluorescence value compared to the target value. (E) Fluorescence image of microelectrode array with SNARF-1 dye with labels for multi-column bi-directional control, two separate electrode columns were actuated (yellow) and the fluorescence intensity of SNARF in an area adjacent to the columns (green) was sampled. The fluorescence response (red traces) follows target ramp functions (black dotted traces) both with a negative slope (F) and a positive slope (G),* V_{H+} *is controlled in responds to the error in the experimental fluorescence compared to the target value (blue traces).*

Open-loop tests of the proton pump with SNARF dye in 0.1M Tris buffer show pH gradients forming locally around actuated pixels (**Fig. 5.3.6**).

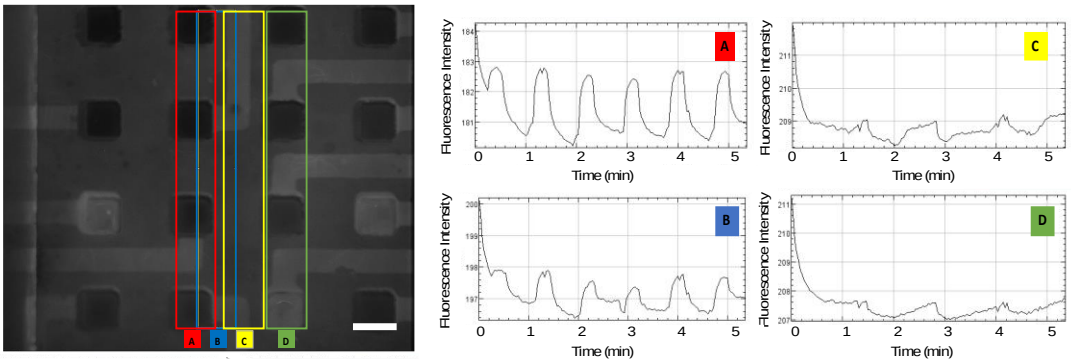

Figure 5.3.6. Fluorescence response of SNARF dye during pH cycling. *Proton pump pixels outlined in red were stimulated to oscillate the pH in a SNARF solution in 0.1M Tris buffer. Scale bar: 100 μm.*

For closed-loop testing with ML-based controller, we start with relatively simple target changes in $[H^+]$ to simulate what may be needed when working with cells over 1600 second trials. In all experiments, we first set a target $[H^+]$ as measured by the fluorescence intensity of SNARF (black dashed line) and we compare it with the actual solution $[H^+]$ as measured by the fluorescence intensity of SNARF (red line) (**Fig. 5.3.5B)**. A difference between target $[H^+]$ and actual $[H^+]$ results in an error value, which in turn triggers V_{H+} actuation of the specific pixel (blue line). We show the ability of the proton pump to perform temporal control over the pH in the form of ramp functions with both positive and negative slopes, these ramp functions combined form a triangle wave (**Fig. 5.3.5B)**. To test repeated stimulation over time, we demonstrate the ability of the proton pump to perform temporal control over the pH in the form of a sine wave over two periods (**Fig. 5.3.5C**). Additionally, the sine function displays the

ability of the ML-based controller to track a function with a gradually changing slope – a challenging feature to achieve with open-loop control. Finally, we use a square wave to step-to and maintain certain pH (**Fig. 5.3.5D**). In addition to temporal control, we achieve spatial control by independently setting $[H^+]$ for two separate areas using two sets of proton pumps **(Fig. 5.3.5E-G)**. To this end, we set for $[H^+]$ to increase as function of time in the area on the left of **Figure 5.3.5E** (green boxes) while we set for $[H^+]$ to decrease as a function of time in the selected area on the left of **Figure 5.3.5E** (green boxes). These $[H^+]$ set points correspond to the downward sloping black trace in **Figure 5.3.5F** and the upward sloping black trace in **Figure 5.3.5G**, respectively. With this strategy, we are able to independently increase and decrease $[H^+]$ in two areas that are separated by only 450 um from each other (**Fig. 5.3.5F, G**). Diffusion of H^+ across the boundaries and cross talk of the electric fields generated by the contacts makes this is a remarkably challenging task. This challenge is confirmed by the relatively large swings of V_{H+} for the proton pumps on both sides that are being actuated trying to control $[H^+]$ (**Fig. 5.3.5G**). These large swings cause the actual $[H^+]$ (red trace) to oscillate visibly around the target value (black trace) until it reaches its set point towards the end of the measurement. With little a-priori knowledge, the ML-based controller adapts quickly to unknown and achieves the target value.

Having demonstrated that our proton pump array precisely set $[H^+]$ as a function of time in specific locations, we used this ability to demonstrate proof-of-concept control of V_{mem} in hiPSCs (**Fig. 5.3.7**). The V_{mem} of proliferative cells such as hiPSCs,

embryonic cells, and cancer cells has a large effect on their proliferative state(*200*). Voltage responsive hiPSCs were generated by using a PiggyBac transposase system to integrate a genetically encoded voltage indicator called ArcLight Q239 with codon optimization for mammalian expression and sequences for membrane trafficking(*201*). To integrate the reporter hiPSCs with the proton pump array, we first grow the hiPSCs on a PDMS slab that is then placed on the top of the proton pump array with the cells facing the proton pump contacts. We select a specific area for $[H^+]$ actuation upon visual inspection of cells and their responsiveness to V_{mem} stimulation (yellow box) **Figure 5.3.7A**. We monitor V_{mem} of cells by measuring the fluorescence intensity of the membrane reporter ArcLight within the red box of **Figure 5.3.7A**. In brief, higher fluorescence intensity corresponds to a hyperpolarized V_{mem} which is sensitive to changes in pH between 7.1 and 8.8. To demonstrate short term control, we first attempt to set V_{mem} for the selected hiPSCs along a triangle waveform (black trace) for a period of 1,400 seconds (**Fig. 5.3.7B**). We set imaging of ArcLight and subsequent ML-based control of $[H^+]$ based on measured V_{H+} to occur every ten seconds to avoid photobleaching. As a result, V_{mem} as measured by ArcLight fluorescence (red trace) oscillates around the target function (black).

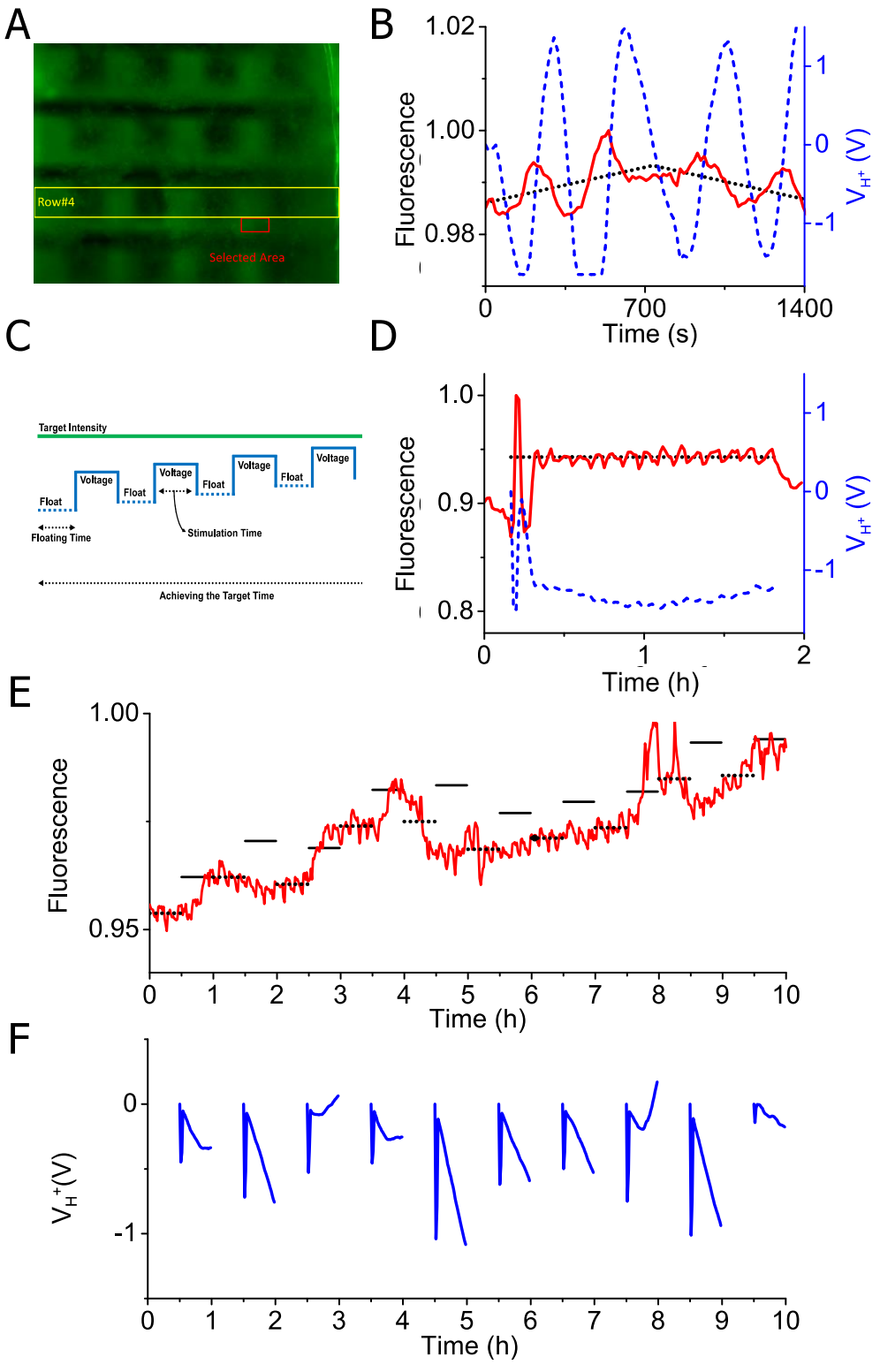
A
Row#4
Selected Area
B
1.02
1.00
0.98
Fluorescence
1
0
-1
V_{H^+} (V)
0
700
1400
Time (s)
C
Target Intensity
Voltage
Float
Floating Time
Stimulation Time
Achieving the Target Time
D
1.0
0.9
0.8
Fluorescence
Time (h)
E
1.00
0.95
Fluorescence
0
1
2
3
4
5
6
7
8
9
10
Time (h)
F
0
-1
V_{H^+}(V)
Time (h)

Figure 5.3.7. Proof of Concept - patterned membrane potential changes induced in hiPSCs. *(A) Fluorescence of the proton pump array with hiPSCs within the microfluidic channel. A row of proton pumps is actuated (yellow box) and the area where cell fluorescence is sampled (red box). (B) The fluorescence intensity of Arclight-hiPSCs (red trace), indicative of V_{mem}, follows the target triangle waveform (black dashed trace), V_{H+} (blue dashed trace) responds to the error in experimental vs. target values. (C) The pulsed-control algorithm used for prolonged control of hiPSCs. While working towards a target fluorescence intensity (green trace), the controller switches between periods of stimulation where V_{H+} is being driven by the ML controller, and periods of no stimulation where the proton pumps are left floating (blue dotted traces). (D) Medium-term control of V_{mem} monitored through the fluorescence intensity of Arclight-hiPSCs (red trace) to form a step increase and holding at a target fluorescence intensity (black trace). V_{H+} is pulsed according to the pulsed-control algorithm with the stimulation and rest duration being 2.5 minutes each. (E) Long-term control for V_{mem} monitored through the fluorescence intensity of Arclight-hiPSCs (red trace) towards increasing the V_{mem} over the course of 10 hours. The mean fluorescence intensity over the floating period of the pulsed-control algorithm was calculated (black dotted lines) and the target fluorescence intensity during stimulation is set to 2 fluorescence units above that value (black solid lines). (F)V_{H+} is controlled during the stimulation periods of the pulsed-control algorithm to raise the V_{mem} and decreases in voltage over the stimulation period indicating a shift towards alkaline conditions around cells which is expected to raise V_{mem}.*

For long term V_{mem} control, we adopt a different sequence for stimulating the hiPSCs in which we alternate periods in which the proton pumps are active with periods during which the proton pumps are left floating (**Fig. 5.3.7C**). We adopted this sequence after observing stimulating the cells for longer than 30 minutes at a time makes the cells less responsive to changes in $[H^+]$. With this sequence, we were able to stepwise increase the V_{mem} of the hiPSCs in the selected locations and maintain this for over one hour (**Fig. 5.3.7D**). We estimate that we were able to increase V_{mem} by about 10 mV respect from the resting V_{mem} by measuring the change in ArcLight fluorescence (*202*). These changes are consistent with what we measured with patch clamping on cells exposed to solutions of different pH (**Fig. 5.3.8**). During this time period, the ML-based control algorithm holds V_{H+} negative, which corresponds to a lower $[H^+]$ concentration than neutral in solution and it is consistent with what we have observed using electrophysiology. To confirm that V_{H+} is having an effect on V_{mem}, we notice that when the cells are not being stimulated, V_{mem} slowly drops towards its initial value likely because $[H^+]$ returns to its neutral level due to the diffusion of ions from the surrounding areas (**Fig. 5.3.7D**). This diffusion is slower than the timescale of our sequence so that we are able to keep V_{mem} to a set value with minimal oscillations. We demonstrate proof-of-concept V_{mem} control for a period of 10 hrs by setting the target ArcLight fluorescence 2 fluorescence units higher than the average measured V_{mem} of the 30 min period prior (**Fig. 5.3.7E, F**). We observe that the V_{mem} of the cells becomes more polarized during the 30 minutes of stimulation and depolarizes during the floating

periods (red trace). Over the course of the trial the extent of polarization during the pumping period is greater than the depolarization in the floating period resulting in a gradual trend towards polarization for the hiPSCs. By calibrating the fluorescence change in the Arclight reporter, we estimate that we were able to achieve an increase V_{mem} of the selected hiPSCs by 10 mV in the 10 hr period.

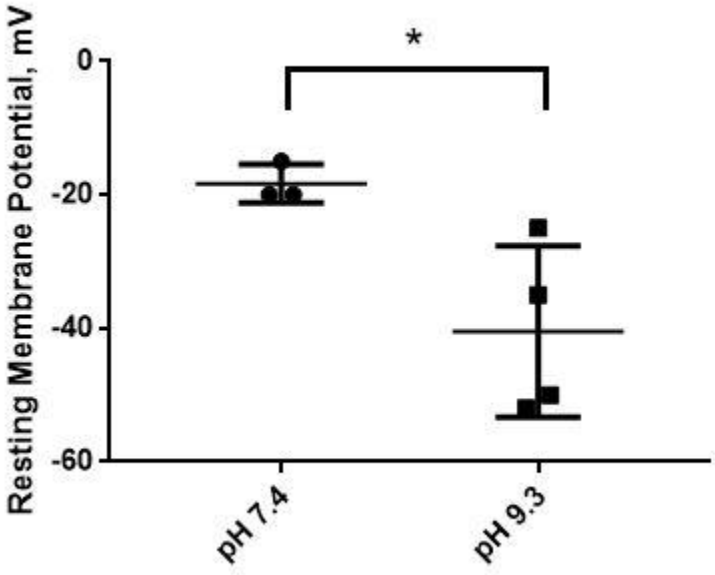

Figure 5.3.8. Electrophysiology measurements of hiPSC resting membrane potential. *Current clamp at 0 pA was used to find the resting membrane potential of hiPSC ArcLight cells in mTeSR no phenol red at the control pH of 7.4 and the high pH of 9.3.*

5.3.2 DISCUSSION

Bioelectronic actuators are an important part of realizing two-way communication with living systems. Inherent challenges in actuating biological tissues such as information carrier mismatch and system dynamics have limited the field to a point where the number of examples of bioactuators is relatively few compared to that of biosensors. Here, we show that it is possible to combine proton pumps as bioactuators with machine learning-based control approaches into biohybrid system that can address these issues to achieve precise closed-loop control of pH, which in turns allows long term proof-of-concept closed-loop control of membrane voltage in cells. To the best of our knowledge, this is the first proof- of-concept control of V_{mem} on non-electrically excitable cells using closed-loop bioelectronic devices. Our ML approach did not experience failure modes dealing with uncertainties associated with over-stimulation of the biology, device variability, and saturation of the system. To this end, we can manipulate V_{mem} for periods as long as 10 hrs opening the opportunity for long-term control of cell function and proliferation. This ability to induce V_{mem} changes on non-excitatory cell types is of interest for applications in regenerative medicine and synthetic biology. In the future, a combination of additional monovalent and divalent ion species, and small ionic molecules, can increase the capabilities of our system. Importantly, closed-loop biohybrid systems, such as this one, are highly anticipated due to their broad applicability across the fields of biology and engineering. Thus, new technology in synthetic biology and bioelectronics with closed-loop control could result in unprecedented spatiotemporal control over nature.(*17, 144*)

5.3.3 EXPERIMENTAL

Device Fabrication: Ion pump arrays were fabricated on borosilicate glass wafer substrates which were cleaned via sonication for 10 minutes in acetone and isopropanol prior to a rinse with water. Au contacts and traces were patterned photolithographically with positive photoresist (S1813, Micro-Chem Corp.) and e-beam evaporation (10nm Ti, 100nm Au) followed by liftoff in acetone. Subsequent patterning with S1813 photoresist defined electrode regions for electrodeposition (see electrodeposition section in materials and methods). After electrodeposition, a 1.4 μm insulating layer of parylene-C was deposited (Specialty Coating Systems Labcoter 2 system) in the presence of A174 adhesion promoter in the deposition chamber. The parylene was etched with an oxygen plasma at 200V with the regions over the electrodes and contact pads exposed, and the interconnecting regions protected by a thick positive photoresist (SPR220-4.5, Micro-Chem Corp.). Prior to deposition of polymer coatings, wafers were treated with the a 5% solution of (3-Glycidyloxypropyl)trimethoxysilane (GOPS) in ethanol via spin coating at 1000 rpm for 30s and then baked at 110C for 5 minutes to promote adhesion of the ion bridge. A mixture of 8%wt polyvinyl alcohol (PVA) and 2% polystyrene sulfonic acid (PSS) in water was then passed through a 0.8 μm MCE syringe filter and spin coated on the wafers at 3000rpm for 30s followed by baking at 120C for 2 hours. The PVA:PSS CEM was etched with an oxygen plasma at 200V with the desired pattern defined with SPR220-4.5 photoresist. A second 1.4 μm coating of parylene was then deposited with the same protocol as above to insulate and

protect the ion bridge from the subsequent steps. To promote adhesion between the parylene and SU8 photoresist, GOPS was again deposited using the above process prior to SU8 patterning. SU8 was spun onto the wafer at a speed of 1250 rpm for 30 s and a ramp of 300 rpm, microfluidic channels of height 40 μm were patterned forming the sidewalls reservoir and target chambers. The parylene insulation layer protecting the ion bridge openings in the reservoir and target channels were defined and etched using the same process as the previous parylene etch. A mixture of 2.5% wt PVA and 5% wt poly(diallyldimethylammonium chloride) (PDDA) in water was passed through a 0.8 μm MCE syringe filter and spin coated on the device at 6000rpm for 30 seconds prior to baking at 120C for 1 hour prior to etch features being patterned in SPR220 photoresist and etching with O_2 reactive ion etching. Devices were then diced from the wafers prior to sealing the microfluidics. Single sided microfluidic transparent diagnostic tape (3M 9964) was used to seal the microchannels on the proton pump array after the devices were diced. Features in the tape layer were punched out with 1 mm and 2 mm diameter biopsy punches for fluidic inlets and openings for cell clamping, respectively. The tapes were then aligned to features on the device and pressed to seal by hand.

Electrodeposition: Pd nanoparticles were deposited onto the MEAs using a 1wt.% Palladium Nitrate solution which was made by diluting a 10wt.% PdNO3 solution with DI-water. The nanoparticles were electrochemically deposited by applying a DC

voltage of –0.3V for 4 seconds using an AgCl reference electrode and Pt counter electrode. An Autolab Potentiostat was used for the electrodeposition.

Stimulation Board: The stimulation unit is a custom designed modular circuit board for stimulating up to 64 electrodes simultaneously. The design consists of single-board computer, adjustable voltage sources, ammeters, and an analog switch. The adjustable voltage source can be controlled in a range of -4 V to +4V with a resolution of 1.95 mV and able to source current up to 30 mA. Stimulate current can be measured in a range of -1,650 nA to +1,650 nA with a resolution of 0.8 nA using built-in ammeters. Ultra-Low-Leakage CMOS Analog switches allow the stimulation unit to connect/disconnect individual electrodes results in the addition output stage, floating. The stimulation unit can operate in two different modes, standalone and network. The standalone mode is where the output stages(voltage) of the stimulation unit are pre-programmed and run sequentially. On the other hand, in network mode, the stimulation unit will be listening to an incoming UDP packet, and output stages can be programmed in real-time via a wireless connection. The network mode allows the machine learning control algorithm, which runs in a different machine to perform closed-loop control using feedback from both fluorescent images and measured current.

$[H^+]$ measurement**:** We used microscope based real-time imaging over the MEAs to monitor $[H^+]$ change. We used 50 uM SNARF dispensed in 0.1M Tris buffer as a

fluorescent [H^+] indicator, which was flowed into the target chamber via a sealed microfluidic channel. Thereafter, the device was monitored by BZ-X710 fluorescence microscope with10x Nikon objective (excitation: 560/40 nm, emission: 630/75 nm), and data were collected every 2s in real-time. Each set of experiments was repeated a minimum of three times, representative recordings are presented. Data were analyzed using ImageJ software.

Machine Learning-based controller algorithm: Machine Learning-based controller performs in real-time and updates its parameters online (**Fig. 5.3.9**). The technique could roughly be considered as supervised learning since we know our target response for the cellular system and actively correct bad behavior by the algorithm. There was no training of the ML-based algorithm prior to the initiation of the experiments. Hyperparameters were tuned on the fly at the beginning of the experiment (if needed) and the radial-basis neural network parameters were randomly initialized (**Fig. 5.3.10**). The "training" happened in real-time by learning each time a new data point was generated through the course of the experiment. To provide an appropriate real-time ML-based controller, the total instantaneous error energy function of the system (i.e., $E(k) = \frac{1}{2}e^2(k)$) is considered as a Lyapunov candidate to be utilized for updating the ML-based controller's parameters for guaranteed convergence. Here e(k) is the system error (i.e., $e(k) = R(k) - Y(k)$), R(k) is the target of the system, and Y(k) is the output of the system. The updates to the adaptive ML-based controller's parameters are

made by computing the appropriate gradients which are all derived utilizing the above mentioned Lyapunov candidate. The ML-based controller updates its centers' c_i, weights' w_i, and bias term w_0 by using equations (S5, S6, and S7) in supplementary materials, respectively. Algorithm S1 (in supplementary material) is summarizing the overall real-time adaptive machine learning-based control methodology employed in this paper as pseudo-code.

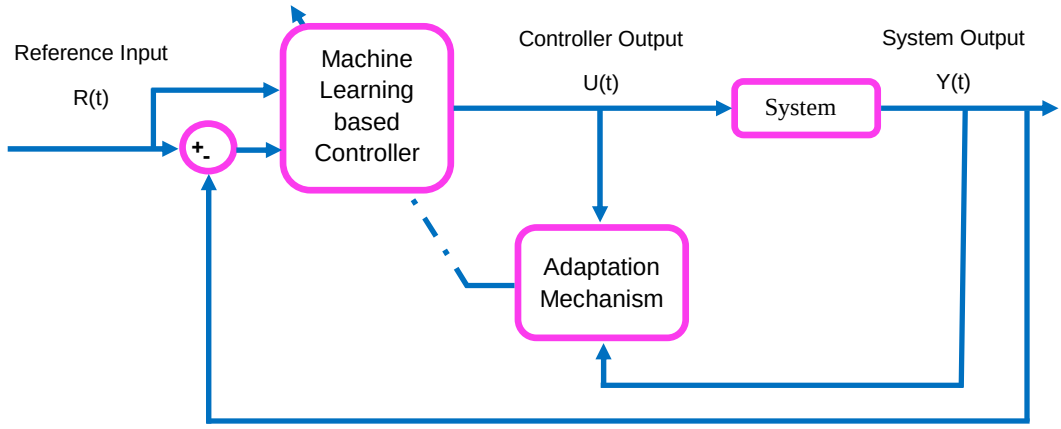

Figure 5.3.9. Architecture of online machine learning based direct controller designed for controlling the system.

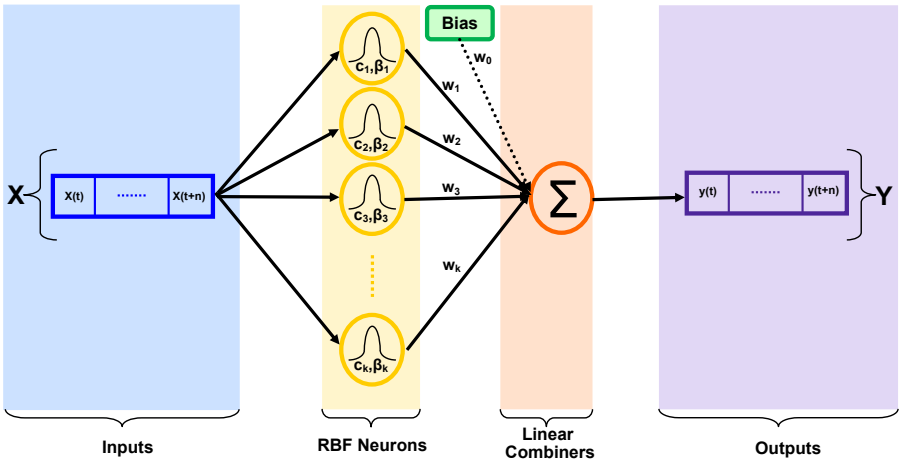

Figure 5.3.10. Architecture of Radial Basis Function Neural Network.

Cells: hiPSCs were a generous donation from David Kaplan's group (ND418566, NINDS Human Genetics and DNA Cell Line Repository(*203*). Stem cells were maintained at 5% CO_2 in StemFlex Medium (A3349401, ThermoFisher) on hESC Qualified Matrigel Matrix (354277, Corning) coated plates with the dilution recommended by the manufacturer. Cells were disassociated with TrypLE Select (12563029, ThermoFisher). Transgenic cells were made by transfecting 500 ng of plasmid via 1 µL of lipofectamine 3000 (L3000008, ThermoFisher) per well of 24 well plate containing 500 µL of Opti-MEM (31985062, ThermoFisher) with 1X RevitaCell (A2644501, ThermoFisher). Reagent was removed after 4 hrs and replaced with StemFlex. Cells were allowed to recover for 3 days before being selected with 50 µg/mL G418 in StemFlex with 10 µg/mL ROCK inhibitor Y-27632 (72304, STEMCELL Technologies). After selection, a stable, clonally pure line was made by serial dilution using StemFlex with 1X RevitaCell. Clones were expanded in StemFlex

and then assayed for alkaline phosphatase activity (SCR004, Millipore). The clone with best membrane localization and expression of ArcLight was chosen for further experimentation and frozen down using NutriFreez D10 (05-713-1E, Biological Industries). Prior to being used in experiments, hiPSC ArcLight cells were plated in mTeSR1 no phenol red (05876, STEMCELL Technologies) and allowed to expand for two passages prior to seeding on PDMS slabs that were coated in hESC Qualified Matrigel Matrix. Slabs were used in bioelectronic chips one to three days after seeding. Cells were perfused with mTeSR1 no phenol red during experiments.

Plasmid Construction: A pENTR1A plasmid with a CAG promoter and multiple cloning site followed by a SV40 poly A was used to clone in the mammalian codon optimized ArcLight Q239 from the plasmid CMV ArcLightCo (Q239)-T2A-nls-mCherry, a gift from Vincent Pieribone (Addgene plasmid # 85806 ; http://n2t.net/addgene:85806 ; RRID:Addgene_85806). Cloning was done by In-Fusion HD Cloning Plus (638909, Takara) with HindIII and SalI restriction enzyme sites added. PCR was done using PrimeSTAR GXL DNA polymerase (R050A, Takara). The resulting pENTR1A CAG ArcLightCo construct was then Gateway LR clonased (11791020, ThermoFisher) into the hyperactive piggyBac transposase-based, helper-independent, and self-inactivating delivery system, pmhyGENIE-3 containing a neomycin resistance gene in the backbone for selection, a gift from Stefan Moisyadi(*204*). The resulting plasmid HypG3NeoBBArcLightCo (Q239) was used for subsequent transfections.

hiPSC ArcLight pH Response Assay: A PDMS microfluidic chip with multiple inputs was used to sequentially add mTeSR1 no phenol red media set at different pH by adding 5N NaOH or 1N HCl to large colonies of hiPSC ArcLight cells. The pH of the media was tested before and after the experiment to make sure that it had stayed constant during the experiment. Each pH solution was flowed over the cells for 5 minutes followed by the control media and images were taken of the cells every minute using an EVOS FL Auto2 imaging system with a standard GFP filter. Each solution was tested twice to make sure that the genetically encoded reporter was still responsive even after high pH media was applied.

Electrophysiology: hiPSC ArcLight cells were grown in mTeSR1 with no phenol red for two passages. Cells were then seeded on hESC Qualified Matrigel Matrix coated cover slips at a very low density. Cells were patched using mTeSR no phenol red media as the external media with or without 8.31 mM NaOH. The internal solution was 130 mM KCl, 10 mM NaCl, 0.5 mM MgCl2, 10 mM HEPES, 1 mM EGTA, 2 mM Mg-ATP, adjusted to pH 7.2 with NaOH. Resting membrane potential recordings were obtained by current clamp at 0 pA for 10 sweeps for 10 seconds each.

5.4 ION PUMP CONTROL DISCUSSION

5.4.1 CLOSED LOOP CONTROL IN BIOELECTRONICS

Bioelectronics approaches for the control of cellular behavior are often focused on health care applications such as pacemakers, neural implants, and electroceuticals (*205-208*). Applications in peripheral neuromodulation has gained the most interest with great potential for closed-loop control to help regain motor control (*209*). The integration of feedback provides an advantage over open-loop control by increasing efficiency and minimizing side effects (**Fig. 5.4.1A**).

Current methods in closed-loop control for biological systems inside and outside of bioelectronics rely on traditional tools from control theory. For example, another application that has gained similar traction as neural modulation is in diabetes management. Control efforts for an artificial pancreas have been numerous (*210*) but generally lie in one of two strategies. The first strategy is a proportional-integral-derivative (PID) controller, which is a common method in industry and thought to mimic nature (**Fig. 5.4.1B**). The second strategy, is a model-predictive controller (MPC), which uses a model to forecast the effects of control on the system (**Fig. 5.4.1C**). MPC controllers are used to predict the effects of insulin delivery on glucose levels and pick the optimal strategy to achieve the desired glucose level (*209, 211*).

While PID is the commonly adopted controller in practical engineering, its performance degrades when the system is exposed to the non-linearities, uncertainty, and unknown disturbances induced by unwanted phenomena such as variational changes in environmental conditions (**Fig. 5.4.1B**). In diabetes management, this can come from dietary changes or increased physical activity. While researchers have developed methods to improve PID performance by increasing robustness to non-linear systems with uncertainties and process noise (*181, 212, 213*), the primary hurdle with the PID controller is that conventional approaches to designing the parameters of the PID rely on a time-invariant linear or linearized model of the system (*181, 212, 213*). This becomes a problem when dynamics become unpredictable or target goals increase in complexity and move away from maintaining homeostasis. On the other hand, an MPC approach can handle nonlinearities and track time varying target outputs, however it can be sensitive to unmodeled dynamics (**Fig. 5.4.1C**). These approaches are not immune to the inherent properties of nature such as stochasticity (*169*) and unmodeled dynamics (*168, 169*).

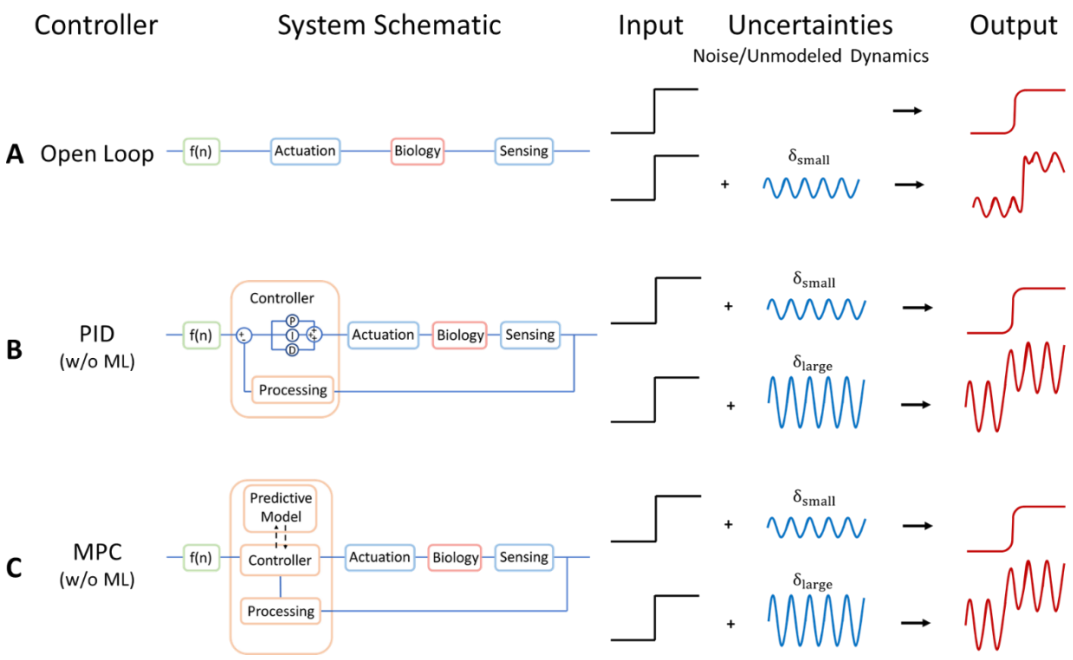

Figure 5.4.1. Bioelectronic control options. *(A) Open-loop, (B) PID, and (C) MPC methods in bioelectronic control and their robustness to uncertainties, noise, unmodeled dynamics.*

The successful applications of control systems theory to biological systems have primarily relied on utilizing a detailed set of mathematical tools to initially model biological systems with precision (*214*). These models require significant a priori knowledge the underlying chemical and genetic mechanisms governing the overall systems (*44*, *215*). Even if this knowledge were to exists, biological systems are adaptive, which means that their response to control and actuation varies with time. As a result, developing closed-loop controllers that can evaluate a signal from a sensor and drive an actuator accordingly are particularly challenging for bioelectronic systems due

to variable conditions that make standard closed-loop control mechanisms unreliable. Here, we argue that methods in ML provide a suitable platform to overcome these challenges but require further development and describe a proof-of-concept example of ML control of pH and cellular response.

5.4.2 MACHINE LEARNING FOR BIOELECTRONIC CONTROL

ML-based techniques are suitable when accurate control is required in the absence of a precise mathematical model (*216*). The best-known ML techniques rely on the availability of large datasets a priori and have not been applied to control bioelectronic devices (*184-187*). We propose that ML-based techniques that are explored as control solutions outside of biology for cases involving complex non-linear systems are also suitable for closing the loop for bioelectronic systems containing biosensors, biology, and bioelectronic actuators. To this end, tools from control systems theory leveraging ML can be used to learn from new observations for effective real-time operation without data a priori (*188, 217-219*). ML-based techniques can be implemented directly (**Fig. 5.4.2A**) or indirectly (**Fig. 5.4.2B**) to solve complex control problems (*220, 221*).

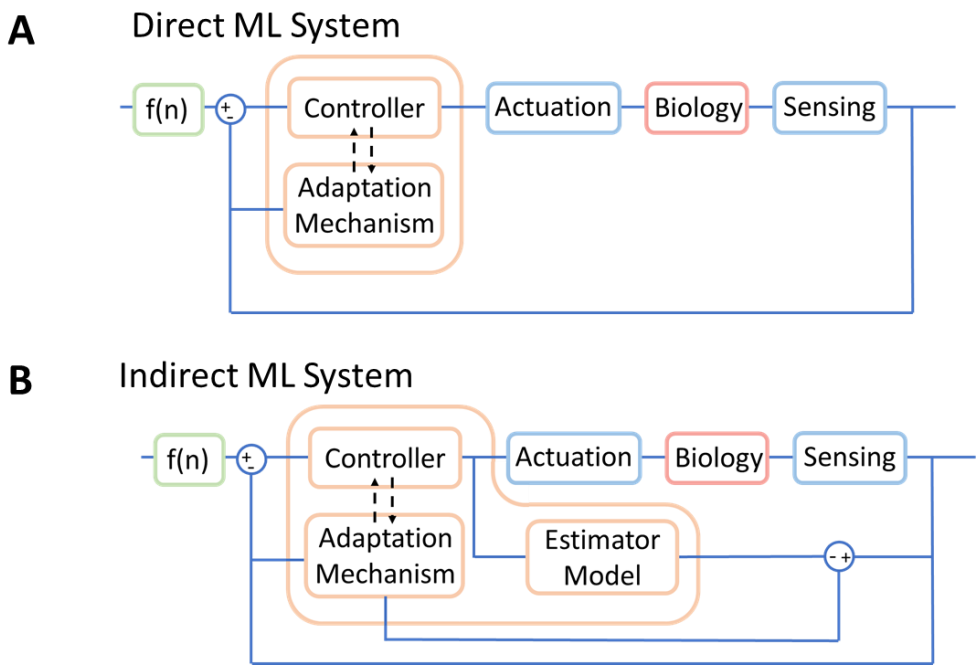

Figure 5.4.2. ML Control schematic. *(A) Direct and (B) Indirect ML system architectures.*

An example of ML control of bioelectronics is the real-time ML control of pH in solution recently demonstrated by the authors (*218*, *222*). This approach can be expanded to the control of cell membrane voltage (V_{mem}) facilitated by pH with an addition of control hierarchy (**Fig. 5.4.3A**). This hierarchy contains three levels: a decision maker, a planner, and a low-level controller. The decision maker sets the short-term goals (pH values) that in turn affect the long-term goals (V_{mem}). The planner organizes the activities between those required by the decision maker and the low - level controller that directly interfaces with the bioelectronic actuators and sensors. An example of an activity required by the decision maker is the mapping V_{mem} in response

to change in pH. An example of an activity required by the low-level controller is adjusting the setpoints for a more effective operation of bioelectronics actuators. The low level- controller interfaces directly with the bioelectronic actuator and sensor to provide data for the higher-level controllers.

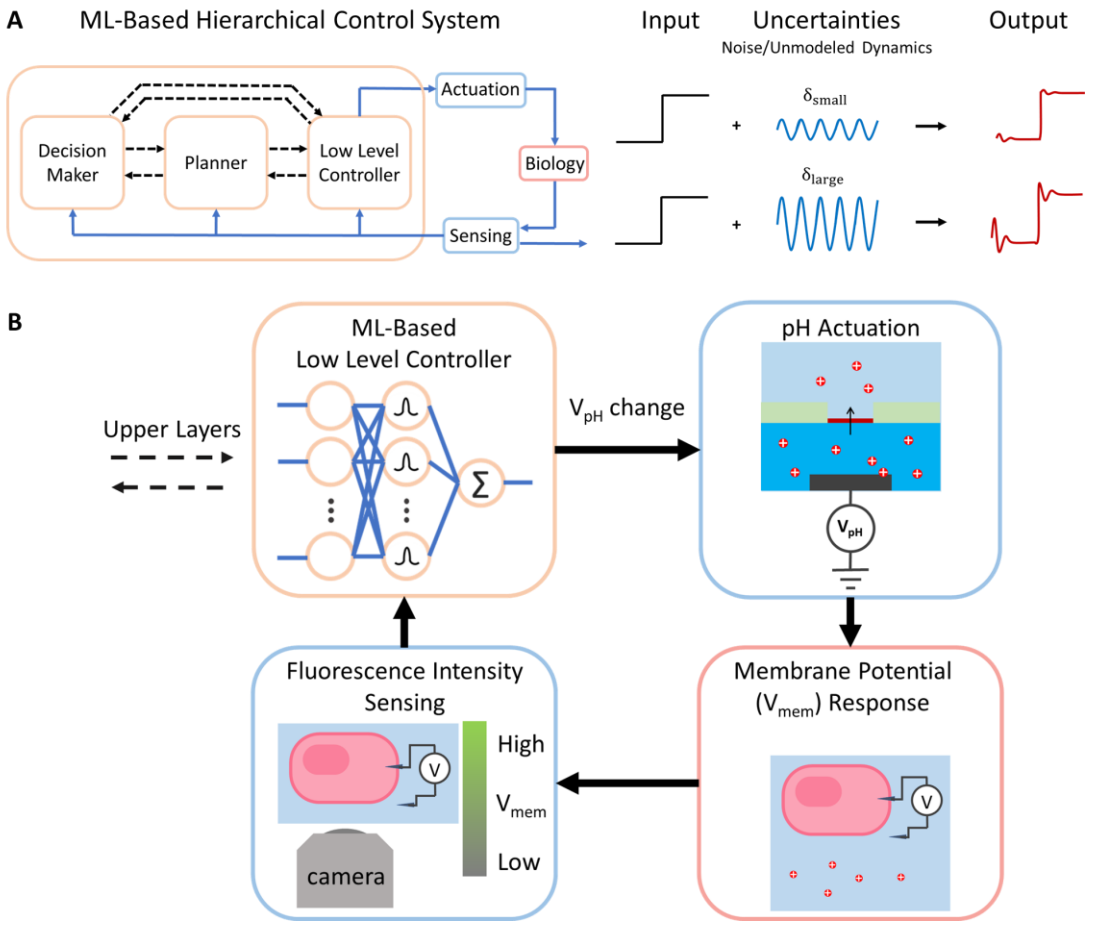

Figure 5.4.3. Hierarchical control for bioelectronics. *(A) The hierarchical control system and its main components (i.e., Decision-Maker, Planner, and Low-level Controller) and its robustness to uncertainties, noise, unmodeled dynamics. (B) ML-based system for Vmem control using pH modifying bioelectronics and fluorescence feedback.*

In this system, pH changing actuators affect the [H^+] surrounding a cell and shift the cell's membrane potential (**Fig. 5.4.3B**). This shift is measured with a voltage sensitive fluorophore. The fluorescence intensity of the fluorophore is fed back into the controller and compared with the set value to see whether further actuation is required or not (**Figure 5.4.3B**). The advantage using ML for this system is that no assumptions are made on the most suitable control algorithm, which would be impossible to determine a priory given the uncertainty associated with cell response to actuation. In this case, uncertainties and non-linearities of the system arise from elements of the system that occur at different timescales including temporal ionic currents that occur in response to the electric field, membrane bound ion channel activity, and expression of stress response factors. Here a neural network learns how to drive the bioelectronic device to achieve the desired response in the cells despite these uncertainties. This network is robust to variability and noise both in the cell response and the bioelectronic devices themselves.

6. OUTLOOK

The developments in this dissertation contribute towards the impact of ion-based bioelectronics for human health, synthetic biology, and biotechnology applications. Protonic activation of catalytic surfaces through pH modulation will enable long-term implants of highly sensitive biosensors. Importantly, this pH activated metal-oxide catalyst architecture is also applicable in industrial applications where heterogeneous catalysts are used. The realization of protonic ion pumps for *in vitro* applications will enable studies to understand how pH and ionic gradients can alter cell function and identity for synthetic biological applications. These *in vitro* devices are a gateway towards closed-loop *in vivo* systems to treat disease and injury in people. Finally, my work on long-term closed-loop control of bioelectronics is the first example of applied machine learning towards solving these problems and will be fundamental for a future where smart bioelectronics devices and electroceuticals can improve human health.

7. REFERENCES

1. E. M. Bick, The classic. The effects of artificial electricity on muscular motion. Aloysio Luigi Galvani. *Clin Orthop Relat Res* **88**, 2-10 (1972).

2. Y. Fang, X. Li, Y. Fang, Organic bioelectronics for neural interfaces. *Journal of Materials Chemistry C* **3**, 6424-6430 (2015).

3. S. Loffler, K. Melican, K. P. R. Nilsson, A. Richter-Dahlfors, Organic bioelectronics in medicine. *J Intern Med* **282**, 24-36 (2017).

4. J. Rivnay, R. M. Owens, G. G. Malliaras, The Rise of Organic Bioelectronics. *Chemistry of Materials* **26**, 679-685 (2013).

5. D. T. Simon, E. O. Gabrielsson, K. Tybrandt, M. Berggren, Organic Bioelectronics: Bridging the Signaling Gap between Biology and Technology. *Chem Rev* **116**, 13009-13041 (2016).

6. T. Someya, Z. Bao, G. G. Malliaras, The rise of plastic bioelectronics. *Nature* **540**, 379-385 (2016).

7. K. Famm, B. Litt, K. J. Tracey, E. S. Boyden, M. Slaoui, Drug discovery: a jump-start for electroceuticals. *Nature* **496**, 159-161 (2013).

8. N. Misra *et al.*, Bioelectronic silicon nanowire devices using functional membrane proteins. *Proc Natl Acad Sci U S A* **106**, 13780-13784 (2009).

9. A. Noy, Bionanoelectronics. *Adv Mater* **23**, 807-820 (2011).

10. E. E. Josberger *et al.*, Proton conductivity in ampullae of Lorenzini jelly. *Sci Adv* **2**, e1600112 (2016).

11. D. D. Ordinario *et al.*, Bulk protonic conductivity in a cephalopod structural protein. *Nat Chem* **6**, 596-602 (2014).

12. C. Zhong *et al.*, A polysaccharide bioprotonic field-effect transistor. *Nat Commun* **2**, 476 (2011).

13. S. W. Hwang *et al.*, A physically transient form of silicon electronics. *Science* **337**, 1640-1644 (2012).

14. C. D. Bostick *et al.*, Protein bioelectronics: a review of what we do and do not know. *Rep Prog Phys* **81**, 026601 (2018).

15. M. Torculas, J. Medina, W. Xue, X. Hu, Protein-Based Bioelectronics. *ACS Biomater Sci Eng* **2**, 1211-1223 (2016).

16. P. W. Rothemund, Folding DNA to create nanoscale shapes and patterns. *Nature* **440**, 297-302 (2006).

17. J. Selberg, M. Gomez, M. Rolandi, The Potential for Convergence between Synthetic Biology and Bioelectronics. *Cell Syst* **7**, 231-244 (2018).

18. S. Z. Bisri, S. Shimizu, M. Nakano, Y. Iwasa, Endeavor of Iontronics: From Fundamentals to Applications of Ion-Controlled Electronics. *Adv Mater* **29**, (2017).

19. H. Chun, T. D. Chung, Iontronics. *Annu Rev Anal Chem (Palo Alto Calif)* **8**, 441-462 (2015).

20. Y. Chang *et al.*, First Decade of Interfacial Iontronic Sensing: From Droplet Sensors to Artificial Skins. *Adv Mater* **33**, e2003464 (2021).

21. S. Keene, Y. van de Burgt, Lowering the threshold for bioelectronics. *Nat Mater* **19**, 584-586 (2020).

22. X. Wang *et al.*, A sub-1V, microwatt power-consumption iontronic pressure sensor based on organic electrochemical transistors. *IEEE Electron Device Lett* **42**, 46-49 (2021).

23. Y. Wang, Z. Wang, Z. Su, S. Cai, Stretchable and transparent ionic diode and logic gates. *Extreme Mechanics Letters* **28**, 81-86 (2019).

24. S. M. Lim *et al.*, Ion-to-ion amplification through an open-junction ionic diode. *Proc Natl Acad Sci U S A* **116**, 13807-13815 (2019).

25. G. Sun, S. Senapati, H. C. Chang, High-flux ionic diodes, ionic transistors and ionic amplifiers based on external ion concentration polarization by an ion exchange membrane: a new scalable ionic circuit platform. *Lab Chip* **16**, 1171-1177 (2016).

26. J. J. Langer, E. Frąckowiak, S. Golczak, Electrically induced light emission from proton-conducting materials. Protonic light-emitting diodes. *Journal of Materials Chemistry C* **8**, 943-951 (2020).

27. D. Prete *et al.*, III-V semiconductor nanostructures and iontronics: InAs nanowire-based electric double layer field effect transistors. *AIP Conference Proceedings* **2145**, 1-9 (2019).

28. K. Tybrandt, K. C. Larsson, A. Richter-Dahlfors, M. Berggren, Ion bipolar junction transistors. *Proc Natl Acad Sci U S A* **107**, 9929-9932 (2010).

29. K. Tybrandt, E. O. Gabrielsson, M. Berggren, Toward complementary ionic circuits: the npn ion bipolar junction transistor. *J Am Chem Soc* **133**, 10141-10145 (2011).

30. M. Muccini, A bright future for organic field-effect transistors. *Nat Mater* **5**, 605-613 (2006).

31. S. Yuvaraja *et al.*, Organic field-effect transistor-based flexible sensors. *Chem Soc Rev* **49**, 3423-3460 (2020).

32. J. O. M. Bockris, A. K. N. Reddy. (Springer US,, Boston, MA, 2002), pp. 1 online resource (828 p.

33. X. Strakosas, M. Bongo, R. M. Owens, The organic electrochemical transistor for biological applications. *Journal of Applied Polymer Science* **132**, n/a-n/a (2015).

34. Y. Deng *et al.*, H+-type and OH- -type biological protonic semiconductors and complementary devices. *Sci Rep* **3**, 2481 (2013).

35. S. T. Martin, A. Akbari, P. Chakraborty Banerjee, A. Neild, M. Majumder, The inside-out supercapacitor: induced charge storage in reduced graphene oxide. *Phys Chem Chem Phys* **18**, 32185-32191 (2016).

36. P. Janson, E. O. Gabrielsson, K. J. Lee, M. Berggren, D. T. Simon, An Ionic Capacitor for Integrated Iontronic Circuits. *Advanced Materials Technologies* **4**, (2019).

37. C. Li, T. Xiong, P. Yu, J. Fei, L. Mao, Synaptic Iontronic Devices for Brain-Mimicking Functions: Fundamentals and Applications. *ACS Applied Bio Materials* **4**, 71-84 (2020).

38. E. J. Fuller *et al.*, Parallel programming of an ionic floating-gate memory array for scalable neuromorphic computing. *Science* **364**, 570-574 (2019).

39. S. T. Keene, P. Gkoupidenis, Y. Van de Burgt, Neuromorphic computing systems based on flexible organic electronics. *Organic Flexible Electronics*, 531-574 (2021).

40. M. Fahlman *et al.*, Interfaces in organic electronics. *Nature Reviews Materials* **4**, 627-650 (2019).

41. J. Nissa, P. Janson, M. Berggren, D. T. Simon, The Role of Relative Capacitances in Impedance Sensing with Organic Electrochemical Transistors. *Advanced Electronic Materials* **7**, (2021).

42. A.-M. Pappa *et al.*, Organic Electronics for Point-of-Care Metabolite Monitoring. *Trends in Biotechnology* **36**, 45-59 (2018).

43. C. Ward, S. Henderson, N. H. Metcalfe, A short history on pacemakers. *Int J Cardiol* **169**, 244-248 (2013).

44. P. A. Iglesias, B. P. Ingalls, *Control theory and systems biology*. (MIT Press, Cambridge, Mass., 2010), pp. ix, 345 p.

45. D. Del Vecchio, A. J. Dy, Y. Qian, Control theory meets synthetic biology. *J R Soc Interface* **13**, (2016).

46. T. Afroz, C. Beisel, Understanding and exploiting feedback in synthetic biology. *Chemical Engineering Science* **103**, 79-90 (2013).

47. S. A. Benner, A. M. Sismour, Synthetic biology. *Nat Rev Genet* **6**, 533-543 (2005).

48. A. Boo, T. Ellis, G. Stan, Host-aware synthetic biology. *Current Opinion in Systems Biology* **14**, 66-72 (2019).

49. P. E. Purnick, R. Weiss, The second wave of synthetic biology: from modules to systems. *Nat Rev Mol Cell Biol* **10**, 410-422 (2009).

50. S. K. Aoki *et al.*, A universal biomolecular integral feedback controller for robust perfect adaptation. *Nature* **570**, 533-537 (2019).

51. D. Del Vecchio, R. M. Murray, *Biomolecular feedback systems*. (Princeton University Press, Princeton, New Jersey, 2015), pp. vi, 275 pages.

52. F. Menolascina *et al.*, In-vivo real-time control of protein expression from endogenous and synthetic gene networks. *PLoS Comput Biol* **10**, e1003625 (2014).

53. J. B. Lugagne *et al.*, Balancing a genetic toggle switch by real-time feedback control and periodic forcing. *Nat Commun* **8**, 1671 (2017).

54. M. Ghorbani, P. Bogdan, Reducing risk of closed loop control of blood glucose in artificial pancreas using fractional calculus. *Annu Int Conf IEEE Eng Med Biol Soc* **2014**, 4839-4842 (2014).

55. M. O. Din, A. Martin, I. Razinkov, N. Csicsery, J. Hasty, Interfacing gene circuits with microelectronics through engineered population dynamics. *Sci Adv* **6**, eaaz8344 (2020).

56. K. Krawczyk *et al.*, Electrogenetic cellular insulin release for real-time glycemic control in type 1 diabetic mice. *Science* **368**, 993-1001 (2020).

57. J. Selberg, M. Jafari, C. Bradley, M. Gomez, M. Rolandi, Expanding biological control to bioelectronics with machine learning. *APL Materials* **8**, (2020).

58. V. S. Meka *et al.*, A comprehensive review on polyelectrolyte complexes. *Drug Discov Today* **22**, 1697-1706 (2017).

59. K. S. Schanze, A. H. Shelton, Functional polyelectrolytes. *Langmuir* **25**, 13698-13702 (2009).

60. T. A. Waigh, A. Papagiannopoulos, Biological and Biomimetic Comb Polyelectrolytes. *Polymers* **2**, 57-70 (2010).

61. D. Sumanth Kumar, B. Jai Kumar, H. M. Mahesh, Polyelectrolyte layer-by-layer spin assembly of aqueous CdTe quantum dot multilayered thin films. *Journal of Alloys and Compounds* **735**, 2558-2566 (2018).

62. X.-W. Cheng, R.-C. Tang, F. Yao, X.-H. Yang, Flame retardant coating of wool fabric with phytic acid/polyethyleneimine polyelectrolyte complex. *Progress in Organic Coatings* **132**, 336-342 (2019).

63. Z. Liao, G. Wu, D. Lee, S. Yang, Ultrastable Underwater Anti-Oil Fouling Coatings from Spray Assemblies of Polyelectrolyte Grafted Silica Nanochains. *ACS Appl Mater Interfaces* **11**, 13642-13651 (2019).

64. X. Ni, J. Luo, R. Liu, X. Liu, Facile fabrication of flexible UV-cured polyelectrolyte-based coatings for humidity sensing. *Sensors and Actuators B: Chemical* **329**, (2021).

65. C. J. Galvin, M. D. Dimitriou, S. K. Satija, J. Genzer, Swelling of polyelectrolyte and polyzwitterion brushes by humid vapors. *J Am Chem Soc* **136**, 12737-12745 (2014).

66. T. Luo, S. Abdu, M. Wessling, Selectivity of ion exchange membranes: A review. *Journal of Membrane Science* **555**, 429-454 (2018).

67. H. Gregor, Gibbs-Donnan Equilibria in Ion Exchange Resin Systems. *Journal of the American Chemical Society*, (1951).

68. H. Strathmann, in *Encyclopedia of Separation Science*. (Academic Press, London, 2000), chap. Electrodialysis, pp. 1707-1717.

69. T. E. Decoursey, Voltage-gated proton channels and other proton transfer pathways. *Physiol Rev* **83**, 475-579 (2003).

70. A. E. Senior, ATP synthesis by oxidative phosphorylation. *Physiol Rev* **68**, 177-231 (1988).

71. T. E. DeCoursey, Voltage-gated proton channels: what's next? *J Physiol* **586**, 5305-5324 (2008).

72. J. A. Wemmie, R. J. Taugher, C. J. Kreple, Acid-sensing ion channels in pain and disease. *Nat Rev Neurosci* **14**, 461-471 (2013).

73. M. Capasso, T. E. DeCoursey, M. J. Dyer, pH regulation and beyond: unanticipated functions for the voltage-gated proton channel, HVCN1. *Trends Cell Biol* **21**, 20-28 (2011).

74. R. A. Duquette, S. Wray, pH regulation and buffering power in gastric smooth muscle. *Pflugers Arch* **442**, 459-466 (2001).

75. Z. Hemmatian *et al.*, Taking electrons out of bioelectronics: bioprotonic memories, transistors, and enzyme logic. *Journal of Materials Chemistry C* **3**, 6407-6412 (2015).

76. C. Gabrielli, P. Grand, A. Lasia, H. Perrot, Investigation of Hydrogen Adsorption-Absorption into Thin Palladium Films: I. Theory. *Journal of the Electrochemical Society* **151**, (2004).

77. L. Glasser, Proton Conduction and Injection in Solids. *Chemical Reviews* **75**, 21-65 (1974).

78. T. Miyake, E. Josberger, S. Keene, Y. Deng, M. Rolandi, An enzyme logic biopreotonic transducer. *APL Materials* **3**, (2014).

79. T. Flanagan, F. Lewis, Hydrogen Absorption by Palladium in Aqueous Solution. *Trans. Faraday Soc.* **55**, 1400-1408 (1959).

80. X. Strakosas, J. Selberg, Z. Hemmatian, M. Rolandi, Taking Electrons out of Bioelectronics: From Bioprotonic Transistors to Ion Channels. *Adv Sci (Weinh)* **4**, 1600527 (2017).

81. S. Cukierman, Et tu, Grotthuss! and other unfinished stories. *Biochim Biophys Acta* **1757**, 876-885 (2006).

82. M. Kunst, J. M. Warman, Proton mobility in ice. *Nature* **288**, 465-467 (1980).

83. R. Pomès, Theoretical Studies of the Grotthuss Mechanism in Biological Proton Wires. *Israel Journal of Chemistry* **39**, 387-395 (1999).

84. R. Pomès, B. Roux, Molecular Mechanism of H+ Conduction in the Single-File Water Chain of the Gramicidin Channel. *Biophysical Journal* **82**, 2304-2316 (2002).

85. L. Liu, W. Chen, Y. Li, An overview of the proton conductivity of nafion membranes through a statistical analysis. *Journal of Membrane Science* **504**, 1-9 (2016).

86. M. K. Petersen, G. A. Voth, Characterization of the solvation and transport of the hydrated proton in the perfluorosulfonic acid membrane nafion. *J Phys Chem B* **110**, 18594-18600 (2006).

87. P. R. Solanki, A. Kaushik, V. V. Agrawal, B. D. Malhotra, Nanostructured metal oxide-based biosensors. *NPG Asia Materials* **3**, 17-24 (2011).

88. P. Si, Y. Huang, T. Wang, J. Ma, Nanomaterials for electrochemical non-enzymatic glucose biosensors. *RSC Advances* **3**, (2013).

89. X. Strakosas *et al.*, A non-enzymatic glucose sensor enabled by bioelectronic pH control. *Sci Rep* **9**, 10844 (2019).

90. C. f. D. C. a. Prevention, National Diabetes Statistics Report, 2017. *Atlanta, GA: Centers for Disease Control and Prevention, US Dept of Health and Human Services*, (2017).

91. P. Zimmet, K. G. Alberti, D. J. Magliano, P. H. Bennett, Diabetes mellitus statistics on prevalence and mortality: facts and fallacies. *Nat Rev Endocrinol* **12**, 616-622 (2016).

92. A. J. Bandodkar, J. Wang, Non-invasive wearable electrochemical sensors: a review. *Trends Biotechnol* **32**, 363-371 (2014).

93. E. Witkowska Nery, M. Kundys, P. S. Jelen, M. Jonsson-Niedziolka, Electrochemical Glucose Sensing: Is There Still Room for Improvement? *Anal Chem* **88**, 11271-11282 (2016).

94. W. Gao *et al.*, Fully integrated wearable sensor arrays for multiplexed in situ perspiration analysis. *Nature* **529**, 509-514 (2016).

95. H. Yao *et al.*, A contact lens with integrated telecommunication circuit and sensors for wireless and continuous tear glucose monitoring. *Journal of Micromechanics and Microengineering* **22**, 075007 (2012).

96. J. Kim, A. S. Campbell, J. Wang, Wearable non-invasive epidermal glucose sensors: A review. *Talanta* **177**, 163-170 (2018).

97. A. Martin *et al.*, Epidermal Microfluidic Electrochemical Detection System: Enhanced Sweat Sampling and Metabolite Detection. *ACS Sens* **2**, 1860-1868 (2017).

98. H. Lee *et al.*, Wearable/disposable sweat-based glucose monitoring device with multistage transdermal drug delivery module. *Sci Adv* **3**, e1601314 (2017).

99. Y.-T. Liao, H. Yao, A. Lingley, B. Parviz, B. P. Otis, A 3-uW CMOS Glucose Sensor for Wireless Contact-Lens Tear Glucose Monitoring. *IEEE Journal of Solid-State Circuits* **47**, 335-344 (2012).

100. B. J. van Enter, E. von Hauff, Challenges and perspectives in continuous glucose monitoring. *Chem Commun (Camb)* **54**, 5032-5045 (2018).

101. H. Lee, Y. J. Hong, S. Baik, T. Hyeon, D. H. Kim, Enzyme-Based Glucose Sensor: From Invasive to Wearable Device. *Adv Healthc Mater* **7**, e1701150 (2018).

102. C. De Block, B. Manuel-y-Keenoy, L. Van Gaal, A review of current evidence with continuous glucose monitoring in patients with diabetes. *J Diabetes Sci Technol* **2**, 718-727 (2008).

103. M. M. Rahman, A. J. Ahammad, J. H. Jin, S. J. Ahn, J. J. Lee, A comprehensive review of glucose biosensors based on nanostructured metal-oxides. *Sensors (Basel)* **10**, 4855-4886 (2010).

104. K. Tian, M. Prestgard, A. Tiwari, A review of recent advances in nonenzymatic glucose sensors. *Mater Sci Eng C Mater Biol Appl* **41**, 100-118 (2014).

105. K. E. Toghill, R. G. Compton, Electrochemical Non-enzymatic Glucose Sensors: A Perspective and an Evaluation. *International Journal of Electrochemical Science* **5**, 1246-1301 (2010).

106. X. Y. Lang *et al.*, Nanoporous gold supported cobalt oxide microelectrodes as high-performance electrochemical biosensors. *Nat Commun* **4**, 2169 (2013).

107. Y. Ding *et al.*, Electrospun Co3O4 nanofibers for sensitive and selective glucose detection. *Biosens Bioelectron* **26**, 542-548 (2010).

108. H. Zhu, L. Li, W. Zhou, Z. Shao, X. Chen, Advances in non-enzymatic glucose sensors based on metal oxides. *Journal of Materials Chemistry B* **4**, 7333-7349 (2016).

109. S. R. Corrie, J. W. Coffey, J. Islam, K. A. Markey, M. A. Kendall, Blood, sweat, and tears: developing clinically relevant protein biosensors for integrated body fluid analysis. *Analyst* **140**, 4350-4364 (2015).

110. Z. Hemmatian *et al.*, Electronic control of H+ current in a bioprotonic device with Gramicidin A and Alamethicin. *Nat Commun* **7**, 12981 (2016).

111. J. Soto-Rodriguez, Z. Hemmatian, E. E. Josberger, M. Rolandi, F. Baneyx, A Palladium-Binding Deltarhodopsin for Light-Activated Conversion of Protonic to Electronic Currents. *Adv Mater* **28**, 6581-6585 (2016).

112. T. Miyake, E. E. Josberger, S. Keene, Y. Deng, M. Rolandi, An enzyme logic bioprotonic transducer. *APL materials* **3**, 014906 (2015).

113. Y. Deng, T. Miyake, S. Keene, E. E. Josberger, M. Rolandi, Proton mediated control of biochemical reactions with bioelectronic pH modulation. *Sci Rep* **6**, 24080 (2016).

114. Z. Hemmatian *et al.*, Delivery of Cargo with a Bioelectronic Trigger. *ACS Appl Mater Interfaces*, (2018).

115. S. Park, H. Boo, T. D. Chung, Electrochemical non-enzymatic glucose sensors. *Anal Chim Acta* **556**, 46-57 (2006).

116. P. Bollella *et al.*, Beyond graphene: Electrochemical sensors and biosensors for biomarkers detection. *Biosens Bioelectron* **89**, 152-166 (2017).

117. J. Isaksson *et al.*, Electronic control of Ca2+ signalling in neuronal cells using an organic electronic ion pump. *Nat Mater* **6**, 673-679 (2007).

118. T. Arbring Sjöström *et al.*, A Decade of Iontronic Delivery Devices. *Advanced Materials Technologies* **3**, (2018).

119. I. Bernacka-Wojcik *et al.*, Implantable Organic Electronic Ion Pump Enables ABA Hormone Delivery for Control of Stomata in an Intact Tobacco Plant. *Small* **15**, e1902189 (2019).

120. X. Strakosas *et al.*, A Bioelectronic Platform Modulates pH in Biologically Relevant Conditions. *Adv Sci (Weinh)* **6**, 1800935 (2019).

121. J. Selberg *et al.*, Machine Learning-Driven Bioelectronics for Closed-Loop Control of Cells. *Advanced Intelligent Systems* **2**, (2020).

122. V. S. Stoll, J. S. Blanchard, Buffers - Principles and Practice. *Methods in Enzymology* **182**, 24-38 (1990).

123. P. D. Boyer *et al.*, Oxidative phosphorylation and photophosphorylation. *Annu Rev Biochem* **46**, 955-966 (1977).

124. M. Capasso, T. E. DeCoursey, M. J. S. Dyer, pH regulation and beyond: unanticipated functions for the voltage-gated proton channel, HVCN1. *Trends in Cell Biology* **21**, 20-28 (2011).

125. R. A. Duquette, S. Wray, pH regulation and buffering power in gastric smooth muscle. *Pflugers Archiv-European Journal of Physiology* **442**, 459-466 (2001).

126. M. A. Bumke, D. Neri, G. Elia, Modulation of gene expression by extracellular pH variations in human fibroblasts: A transcriptomic and proteomic study. *Proteomics* **3**, 675-688 (2003).

127. Y. Kato *et al.*, Acidic extracellular microenvironment and cancer. *Cancer Cell International* **13**, (2013).

128. M. Chesler, Regulation and modulation of pH in the brain. *Physiol Rev* **83**, 1183-1221 (2003).

129. A. E. Ziemann *et al.*, Seizure termination by acidosis depends on ASIC1a. *Nat Neurosci* **11**, 816-822 (2008).

130. S. Joshi-Barr, C. D. Lux, E. Mahmoud, A. Almutairi, Exploiting Oxidative Microenvironments in the Body as Triggers for Drug Delivery Systems. *Antioxidants & Redox Signaling* **21**, 730-754 (2014).

131. A. Almutairi, S. J. Guillaudeu, M. Y. Berezin, S. Achilefu, J. M. J. Frechet, Biodegradable pH-sensing dendritic nanoprobes for near-infrared fluorescence lifetime and intensity imaging. *Journal of the American Chemical Society* **130**, 444-+ (2008).

132. K. Tybrandt *et al.*, Translating Electronic Currents to Precise Acetylcholineâ€ " Induced Neuronal Signaling Using an Organic Electrophoretic Delivery Device. *Advanced Materials* **21**, 4442-4446 (2009).

133. J. Isaksson *et al.*, Electronically controlled pH gradients and proton oscillations. *Organic Electronics* **9**, 303-309 (2008).

134. E. E. Josberger, Y. Deng, W. Sun, R. Kautz, M. Rolandi, Two-terminal protonic devices with synaptic-like short-term depression and device memory. *Adv Mater* **26**, 4986-4990 (2014).

135. T. Imokawa, K. J. Williams, G. Denuault, Fabrication and characterization of nanostructured Pd hydride pH microelectrodes. *Analytical Chemistry* **78**, 265-271 (2006).

136. J. Horkans, The Hydrogen Region of the Cyclic Voltammetry of Pd - the Effect of Ph and Anion. *Journal of Electroanalytical Chemistry* **209**, 371-376 (1986).

137. M. Grden, M. Lukaszewski, G. Jerkiewicz, A. Czerwinski, Electrochemical behaviour of palladium electrode: Oxidation, electrodissolution and ionic adsorption. *Electrochimica Acta* **53**, 7583-7598 (2008).

138. T. J. Battin, Assessment of fluorescein diacetate hydrolysis as a measure of total esterase activity in natural stream sediment biofilms. *Science of the Total Environment* **198**, 51-60 (1997).

139. M. J. Doughty, S. Glavin, Efficacy of different dry eye treatments with artificial tears or ocular lubricants: a systematic review. *Ophthalmic Physiol Opt* **29**, 573-583 (2009).

140. Z. Hemmatian *et al.*, Hemmatian, Zahra; jalilian, Elmira; Lee, Sanjeun; Strakosas, Xenofon; Khademhosseini, Ali; Almutairi, Adah; Shin, SuRyon; Rolandi, Marco. *ACS Appl Mater Interfaces* **Just Accepted**, (2018).

141. A. Y. Mitrophanov, E. A. Groisman, Positive feedback in cellular control systems. *Bioessays* **30**, 542-555 (2008).

142. C. Cosentino, Bates, D. , *Feedback Control in Systems Biology*. (CRC Press, Boca Raton, 2012).

143. S. Keene, Y. van de Burgt, Lowering the threshold for bioelectronics. *Nat Mater*, (2020).

144. M. Levin, J. Selberg, M. Rolandi, Endogenous Bioelectrics in Development, Cancer, and Regeneration: Drugs and Bioelectronic Devices as Electroceuticals for Regenerative Medicine. *iScience* **22**, 519-533 (2019).

145. H. Yuk, B. Lu, X. Zhao, Hydrogel bioelectronics. *Chem Soc Rev* **48**, 1642-1667 (2019).

146. A. Zhang, C. M. Lieber, Nano-Bioelectronics. *Chem Rev* **116**, 215-257 (2016).

147. M. Jakešová *et al.*, Optoelectronic control of single cells using organic photocapacitors. *Science Advances* **5**, eaav5265 (2019).

148. T. Arbring Sjöström *et al.*, A Decade of Iontronic Delivery Devices. *Advanced Materials Technologies* **3**, 1700360 (2018).

149. R. Epsztein, E. Shaulsky, M. Qin, M. Elimelech, Activation behavior for ion permeation in ion-exchange membranes: Role of ion dehydration in selective transport. *Journal of Membrane Science* **580**, 316-326 (2019).

150. A. Williamson *et al.*, Controlling epileptiform activity with organic electronic ion pumps. *Adv Mater* **27**, 3138-3144 (2015).

151. A. Jonsson *et al.*, Therapy using implanted organic bioelectronics. *Science Advances* **1**, (2015).

152. M. Seitanidou, R. Blomgran, G. Pushpamithran, M. Berggren, D. T. Simon, Modulating Inflammation in Monocytes Using Capillary Fiber Organic Electronic Ion Pumps. *Advanced Healthcare Materials* **8**, (2019).

153. I. Bernacka-Wojcik *et al.*, Implantable Organic Electronic Ion Pump Enables ABA Hormone Delivery for Control of Stomata in an Intact Tobacco Plant. *Small* **15**, (2019).

154. Y. Deng *et al.*, H+-type and OH−-type biological protonic semiconductors and complementary devices. *Scientific reports* **3**, (2013).

155. T. Miyake, M. Rolandi, Grotthuss mechanisms: from proton transport in proton wires to bioprotonic devices. *Journal of Physics: Condensed Matter* **28**, 023001 (2015).

156. C. Zhong *et al.*, A polysaccharide bioprotonic field-effect transistor. *Nature communications* **2**, 476 (2011).

157. Z. Hemmatian *et al.*, Electronic control of H+ current in a bioprotonic device with Gramicidin A and Alamethicin. *Nature Communications* **7**, (2016).

158. J. Soto-Rodriguez, Z. Hemmatian, E. E. Josberger, M. Rolandi, F. Baneyx, A Palladium-Binding Deltarhodopsin for Light-Activated Conversion of Protonic to Electronic Currents. *Advanced Materials* **28**, 6581-+ (2016).

159. D. J. Blackiston, K. A. McLaughlin, M. Levin, Bioelectric controls of cell proliferation: ion channels, membrane voltage and the cell cycle. *Cell Cycle* **8**, 3527-3536 (2009).

160. S. H. Wright, Generation of resting membrane potential. *Adv Physiol Educ* **28**, 139-142 (2004).

161. C. M. Ajo-Franklin, A. Noy, Crossing Over: Nanostructures that Move Electrons and Ions across Cellular Membranes. *Advanced Materials*, (2015).

162. J. L. Whited, M. Levin, Bioelectrical controls of morphogenesis: from ancient mechanisms of cell coordination to biomedical opportunities. *Curr Opin Genet Dev* **57**, 61-69 (2019).

163. H. F. Lodish, *Molecular cell biology*. (W.H. Freeman, New York, ed. 4th, 2000), pp. xxxvi, 1084, G-1017, I-1036 p.

164. S. Sundelacruz, M. Levin, D. L. Kaplan, Role of membrane potential in the regulation of cell proliferation and differentiation. *Stem cell reviews and reports* **5**, 231-246 (2009).

165. M. Levin, Pezzulo, G., and Finkelstein, J. M., Endogenous Bioelectric Signaling Networks: Exploiting Voltage Gradients for Control of Growth and Form. *Annual Review of Biomedical Engineering* **19**, 353-387 (2017).

166. L. Abdul Kadir, M. Stacey, R. Barrett-Jolley, Emerging Roles of the Membrane Potential: Action Beyond the Action Potential. *Front Physiol* **9**, 1661 (2018).

167. M. Levin, G. Pezzulo, J. M. Finkelstein, Endogenous Bioelectric Signaling Networks: Exploiting Voltage Gradients for Control of Growth and Form. *Annu Rev Biomed Eng* **19**, 353-387 (2017).

168. R. Kwok, Five Hard Truths for Synthetic Biology. *Nature* **463**, 288-290 (2010).

169. M. B. Elowitz, A. J. Levine, E. D. Siggia, P. S. Swain, Stochastic gene expression in a single cell. *Science* **297**, 1183-1186 (2002).

170. S. K. Aoki *et al.*, A universal biomolecular integral feedback controller for robust perfect adaptation. *Nature* **570**, 533-+ (2019).

171. L. Bleris *et al.*, Synthetic incoherent feedforward circuits show adaptation to the amount of their genetic template. *Mol Syst Biol* **7**, 519 (2011).

172. C. Briat, A. Gupta, M. Khammash, Antithetic proportional-integral feedback for reduced variance and improved control performance of stochastic reaction networks. *J R Soc Interface* **15**, (2018).

173. C. Briat, M. Khammash, Perfect Adaptation and Optimal Equilibrium Productivity in a Simple Microbial Biofuel Metabolic Pathway Using Dynamic Integral Control. *ACS Synth Biol* **7**, 419-431 (2018).

174. C. Briat, C. Zechner, M. Khammash, Design of a Synthetic Integral Feedback Circuit: Dynamic Analysis and DNA Implementation. *ACS Synth Biol* **5**, 1108-1116 (2016).

175. J. Doyle, M. Csete, Motifs, control, and stability. *PLoS Biol* **3**, e392 (2005).

176. M. Freeman, Feedback control of intercellular signalling in development. *Nature* **408**, 313-319 (2000).

177. T. W. Grunberg, D. Del Vecchio, Modular Analysis and Design of Biological Circuits. *Curr Opin Biotechnol* **63**, 41-47 (2019).

178. M. Lawrynczuk, Modelling and nonlinear predictive control of a yeast fermentation biochemical reactor using neural networks. *Chem Eng J* **145**, 290-307 (2008).

179. D. Mishra, P. M. Rivera, A. Lin, D. Del Vecchio, R. Weiss, A load driver device for engineering modularity in biological networks. *Nat Biotechnol* **32**, 1268-1275 (2014).

180. A. Milias-Argeitis, M. Rullan, S. K. Aoki, P. Buchmann, M. Khammash, Automated optogenetic feedback control for precise and robust regulation of gene expression and cell growth. *Nat Commun* **7**, 12546 (2016).

181. K. H. Ang, G. Chong, Y. Li, PID control system analysis, design, and technology. *IEEE transactions on control systems technology* **13**, 559-576 (2005).

182. G. Fiore, G. Perrino, M. Di Bernardo, D. Di Bernardo, In vivo real-time control of gene expression: a comparative analysis of feedback control strategies in yeast. *ACS synthetic biology* **5**, 154-162 (2016).

183. J.-B. Lugagne *et al.*, Balancing a genetic toggle switch by real-time feedback control and periodic forcing. *Nature communications* **8**, 1-8 (2017).

184. V. G. Maltarollo, K. M. Honório, A. r. B. F. da Silva, Applications of artificial neural networks in chemical problems. *Artificial neural networks-architectures and applications*, 203-223 (2013).

185. C. Angermueller, T. Pärnamaa, L. Parts, O. Stegle, Deep learning for computational biology. *Molecular systems biology* **12**, 878 (2016).

186. Y. Park, M. Kellis, Deep learning for regulatory genomics. *Nature biotechnology* **33**, 825 (2015).

187. D. M. Camacho, K. M. Collins, R. K. Powers, J. C. Costello, J. J. Collins, Next-generation machine learning for biological networks. *Cell* **173**, 1581-1592 (2018).

188. S. N. Kumpati, P. Kannan, Identification and control of dynamical systems using neural networks. *IEEE Transactions on neural networks* **1**, 4-27 (1990).

189. E. Lavretsky, K. A. Wise, in *Advanced textbooks in control and signal processing,*. (Springer,, London ; New York, 2013), pp. 1 online resource.

190. M. J. a. G. M. a. J. S. a. M. J. a. H. D. a. P. P. a. M. T. a. M. R. a. M. Gomez, Feedback Control of Bioelectronic Devices Using Machine Learning. *IEEE Control Systems Letters*, (2020).

191. J. Park, I. W. Sandberg, Universal Approximation Using Radial-Basis-Function Networks. *Neural Comput* **3**, 246-257 (1991).

192. J. Park, I. W. Sandberg, Universal approximation using radial-basis-function networks. *Neural Comput* **3**, 246-257 (1991).

193. G. Marquez, B. Johnson, M. Jafari, M. Gomez, in *2019 IEEE Symposium Series on Computational Intelligence (SSCI)*. (IEEE, 2019), pp. 120-125.

194. X. Strakosas *et al.*, Bioelectronic Modulators: A Bioelectronic Platform Modulates pH in Biologically Relevant Conditions (Adv. Sci. 7/2019). *Adv Sci (Weinh)* **6**, 1970041 (2019).

195. Z. Hemmatian *et al.*, Delivery of Cargo with a Bioelectronic Trigger. *ACS Applied Materials & Interfaces* **10**, 21782-21787 (2018).

196. A. Massa *et al.*, The effect of extracellular acidosis on the behaviour of mesenchymal stem cells in vitro. *Eur Cell Mater* **33**, 252-267 (2017).

197. S. C. Chao *et al.*, Functional and molecular mechanism of intracellular pH regulation in human inducible pluripotent stem cells. *World J Stem Cells* **10**, 196-211 (2018).

198. Y. Xu, P. Zou, A. E. Cohen, Voltage imaging with genetically encoded indicators. *Curr Opin Chem Biol* **39**, 1-10 (2017).

199. R. Kateklum, B. Manuel, C. Pieralli, S. Mankhetkorn, B. Wacogne, Simplifying ratiometric C-SNARF-1 pH calibration procedures with a simple post-processing. *International Journal of Photochemistry and Photobiology* **2**, 94 - 101 (2017).

200. R. Binggeli, R. C. Weinstein, Membrane potentials and sodium channels: Hypotheses for growth regulation and cancer formation based on changes in sodium channels and gap junctions. *Journal of Theoretical Biology* **123**, 377-401 (1986).

201. J. Platisa, G. Vasan, A. Yang, V. A. Pieribone, Directed Evolution of Key Residues in Fluorescent Protein Inverses the Polarity of Voltage Sensitivity in the Genetically Encoded Indicator ArcLight. *ACS Chem Neurosci* **8**, 513-523 (2017).

202. L. Jin *et al.*, Single action potentials and subthreshold electrical events imaged in neurons with a fluorescent protein voltage probe. *Neuron* **75**, 779-785 (2012).

203. S. Almeida *et al.*, Induced pluripotent stem cell models of progranulin-deficient frontotemporal dementia uncover specific reversible neuronal defects. *Cell Rep* **2**, 789-798 (2012).

204. J. Marh *et al.*, Hyperactive self-inactivating piggyBac for transposase-enhanced pronuclear microinjection transgenesis. *Proc Natl Acad Sci U S A* **109**, 19184-19189 (2012).

205. K. Famm, B. Litt, K. J. Tracey, E. S. Boyden, M. Slaoui, A jump-start for electroceuticals. *Nature* **496**, 159-161 (2013).

206. K. Birmingham *et al.*, Bioelectronic medicines: a research roadmap. *Nat Rev Drug Discov* **13**, 399-400 (2014).

207. A. Guemes Gonzalez, R. Etienne-Cummings, P. Georgiou, Closed-loop bioelectronic medicine for diabetes management. *Bioelectron Med* **6**, 11 (2020).

208. A. D. Mickle *et al.*, A wireless closed-loop system for optogenetic peripheral neuromodulation. *Nature* **565**, 361-365 (2019).

209. P. D. Ganzer, G. Sharma, Opportunities and challenges for developing closed-loop bioelectronic medicines. *Neural Regeneration Research* **14**, 46 (2019).

210. G. Quiroz, The evolution of control algorithms in artificial pancreas: A historical perspective. *Annual Reviews in Control* **48**, 222-232 (2019).

211. B. Kovatchev, Diabetes technology: monitoring, analytics, and optimal control. *Cold Spring Harbor Perspectives in Medicine* **9**, a034389 (2019).

212. Y. Li, K. H. Ang, G. C. Chong, PID control system analysis and design. *IEEE Control Systems Magazine* **26**, 32-41 (2006).

213. A. O'Dwyer, *Handbook of PI and PID controller tuning rules*. (Imperial college press, 2009).

214. J. E. Cury, F. L. Baldissera, Systems biology, synthetic biology and control theory: a promising golden braid. *Annual Reviews in Control* **37**, 57-67 (2013).

215. P. Smolen, D. A. Baxter, J. H. Byrne, Mathematical modeling of gene networks. *Neuron* **26**, 567-580 (2000).

216. M. Giovanny, B. Johnson, M. Jafari, M. Gomez, Online Machine Learning Based Predictor for Biological Systems. *SSCI*, 120-125 (2019).

217. M. Jafari, M. Gomez, in *2019 IEEE Symposium Series on Computational Intelligence (SSCI)*. (IEEE, 2019), pp. 163-169.

218. M. Jafari *et al.*, Feedback Control of Bioelectronic Devices Using Machine Learning. *IEEE Control Systems Letters*, 1-1 (2020).

219. E. Lavretsky, K. A. Wise, in *Robust and adaptive control*. (Springer, 2013), pp. 317-353.

220. M. T. Hagan, H. B. Demuth, in *Proceedings of the 1999 American control conference (cat. No. 99CH36251)*. (IEEE, 1999), vol. 3, pp. 1642-1656.

221. J. T. Spooner, M. Maggiore, R. Ordonez, K. M. Passino, *Stable adaptive control and estimation for nonlinear systems: neural and fuzzy approximator techniques*. (John Wiley & Sons, 2004), vol. 43.

222. J. Selberg *et al.*, Machine Learning-Driven Bioelectronics for Closed-Loop Control of Cells. *Advanced Intelligent Systems,* (2020).